Politecnico di Torino

Master of science program in Architecture for Sustainability

December 2025 Graduation Season

Digital Documentation of the Nisa Archaeological Site (Turkmenistan):

Enhancing the Integration of Laser Scanning Methods for 3D Printing and Video Mapping

Supervisors:

Antonia Teresa Spano'

Giacomo Patrucco

Riccardo Roberto Covino

Student:

Biwei Kong

Index

Abstract

This project aims at establishing a comprehensive digital archive for an archaeological site, ensuring its accessibility for future applications across multiple scales and diverse research needs. The geomatics methods developed according to the site's features provide valuable insights in the field of digital surveying, while the methodology of applying 3D printing to the site reconstruction offers the public a direct form of visualization, and the involvement of projection mapping further enhances the immersive experience and richness of the exhibition, thereby enabling the widespread sharing of academic achievements across different disciplines. The archaeological site selected and examined in this thesis is the Old Nisa site, an ancient city dating back more than two thousand years, the capital of the Parthian civilization, located approximately 16 km from the present capital of Turkmenistan, Ashgabat.

Taking the Old Nisa as research subjects, the research develops a complete workflow including on-site geomatic survey, point cloud acquisition and processing, digital model reconstruction, and derivative outputs for physical and visual representation. The thesis is mainly structured covering the conceptual foundation of cultural heritage and digital archiving (Chapter 1), historical and archaeological context of Old Nisa (Chapter 2), theoretical background of geomatic survey and data collection workflow (Chapter 3), point cloud data processing and analysis (Chapter 4), 3D printing-based physical reconstruction (Chapter 5), and video mapping (projection mapping) for enhancing digital interpretation and public communication (Chapter 6).

This thesis is based on the collaboration of the Laboratorio di Geomatica per i Beni Culturali (Lab G4CH) of Politecnico di Torino, the Centro Ricerche Archeologiche e Scavi di Torino (CRAST) per il Medio Oriente e l'Asia, and the Laboratorio Multimediale (MULTIMEDIALab) of Politecnico di Torino within the framework of an exhibition project organized between the Musei Capitolini in Rome and the official institutions of Turkmenistan. The exhibition was held at piazza Campidoglio of

Rome on October 25, titled as “Antiche civiltà del Turkmenistan (Ancient civilizations of Turkmenistan)”, with the aim of presenting to the public a multidimensional and grand narrative set in the historical context of Central Asia in the 3rd century BC.

The thesis discussed the pressing challenges faced by cultural heritage sites, and further explored practical strategies for applying digital technologies to heritage conservation and dissemination. The author mainly contributed to the optimization of point clouds, further completed the construction of the three-dimensional digital model and the transformation of the physical model.

Image Resources

Fig. 1-2 Evolution of the Parthian region, by author, reference by MULTIMEDIALab

Fig. 3 Satellite view of Ashgabat suburbs - the Old Nisa and New Nisa area, by author

Fig. 4 JuTAKE and Italian Mission excavations in the late 1940s, (Lippolis et al., 2011)

Fig. 5 Landscape of the Old Nisa, by CRAST,
https://www.centroscavitorino.it/en/siti-di-scavo/nisa-2/

Fig. 6 Current situation of the Old Nisa, by Google Earth

Fig. 7-13 The excavation on site, unearthed relics and related research, by CRAST

Fig. 14 Protective intervention methods of the archaeological site, by Eurasia Travel,
https://www.google.com/imgres?q=Old%20Nisa%20&imgurl=https%3A%2F%2Feurasia.travel%2Fwp-content%2Fuploads%2F2024%2F08%2FNissa-20.jpg&imgrefurl=https%3A%2F%2Feurasia.travel%2Fturkmenistan%2Fashgabat%2Fnissa%2F&docid=7XgWftYKKxYHGM&tbnid=vsTdQ1S1W2VtVM&vet=12ahUKEwiqrP-50ZKRAxVzJkQIHf0sJCoQM3oECFEQAA..i&w=1800&h=1200&hcb=2&itg=1&ved=2ahUKEwiqrP-50ZKRAxVzJkQIHf0sJCoQM3oECFEQAA

Fig. 15 Principle and instruments for GNSS/DGNSS/RTK measurement,
By GEODELTA, https://www.geodelta.com/en/articles/how-do-gnss-and-imu-work
By Ориент СистеМС, https://orsyst.ru/page3005641.html
By SMAJAYU,
https://www.amazon.com/SMAJAYU-Surveying-Equipment-Handheld-Channels/dp/B0BQ6WB3R4?ref_=ast_sto_dp&th=1

Fig. 16 Mechanical composition and operating logic of total station
By RRP Survey,
https://www.prabas.com.np/what-is-total-station-its-use-operation-and-advantages/
By Jongchool LEE and Taeho RHO,
https://www.fig.net/resources/proceedings/fig_proceedings/korea/full-papers/session17/lee-rho.htm
By C.R.Kennedy,
https://survey.crkennedy.com.au/products/lg868829/leica-ts07-1--r1000-manual-total-station-with-egl
By Land Surveyors United - Surveying Education Community,
https://landsurveyorsunited.com/photo/polar-method-surveying

Fig. 17 Multiple surveying methods, (Spanò, 2025)

Chapter 1: Introduction

1.1 Topic Background: Cultural Heritage Documentation Trends and Public Education

The traces created by human beings over thousands of years are the evidence of each stage of the development of our civilization. As the carriers of continuity and collective memory, historical heritage not only documents the course of social evolution, but also embodies cultural values that transcend regions and eras. Unlike written records which may be easily falsified, the material presence of heritage serves as quite reliable proof. However, unlike an individual, the civilization will suffer a far longer life span. Therefore, it is the duty of both professionals and the public to guard these legacies across generations, ensuring that the origins of civilization are preserved and continue to inspire those who come after us.

1.1.1 Conceptual framework of cultural heritage conservation

1.1.1.1 Concept of “cultural heritage” and definition of “heritage protection”

Since ancient times, human societies have actively engaged in the protection and preservation of monuments and artifacts. Across both Eastern and Western civilizations, ruling classes and elites consistently maintained and restored palaces, churches, and historic structures, while many ordinary individuals also developed a keen interest in collecting antiquities. However, these early preservation efforts were largely driven by the protectors’ desire to reinforce their own authority or serve personal interests, rather than by a concern for the welfare of humanity as a whole. Such a narrow perspective undoubtedly set a high threshold for heritage preservation, limiting public awareness of the value of shared-cultural assets, while contributing indirectly to the destruction of many irreplaceable treasures.

During the 18th and 19th centuries, the rapid update of societies worldwide and the rise of progressive ideas prompted people to critically examine historical

artifacts. However, the concept of heritage preservation was not proposed systematically at the international level until the 20th century. In 1931, the First International Congress of Architects and Technicians of Historic Monuments was held in Athens, where *The Athens Charter for the Restoration of Historic Monuments* (International Council of Museums, 1931) was adopted, confirming its “seven main resolutions” aimed at emphasizing the importance of protecting historic monuments. After the disaster of World War II, the significance of heritage conservation and restoration became even more pronounced. In 1964, *the Venice Charter* (ICOMOS, 1964) expanded the concept of ancient monuments to “embraces also the urban or rural setting in which is found the evidence of a particular civilization, a significant development or a historic event” based on *the Athens Charter*, and the concept of restoring ancient monuments is discussed more detailed at the same time. The concept of “historical monuments” was no longer limited to individual buildings, but also applied to smaller ancient works that acquired cultural significance over time, in another word cultural relics.

In 1972, UNESCO adopted *the Convention Concerning the Protection of the World Cultural and Natural Heritage* (UNESCO, 1972), which for the first time defined the concept of "World Heritage", aiming to safeguard cultural and natural heritage with outstanding universal value to all mankind. The Convention clarified the responsibility of States Parties to protect their national heritage, established relevant committees and funding programs to ensure its effective implementation, and created the World Heritage List system. The Convention divided "World Heritage" into two categories: “cultural heritage” and “natural heritage”. “Cultural heritage” is defined as “monuments”, “groups of buildings” and “sites”, which is the global starting point of the term “cultural heritage”. Since then, the term has been widely used and has become a core concept in international academic research and protection practice.

It is worth noting that the concept of “mixed heritage” was added into *the Operational Guidelines for the Implementation of the World Heritage Convention* subsequently published by UNESCO (UNESCO, 2017), stated that “Properties

shall be considered as ‘mixed cultural and natural heritage’ if they satisfy a part or the whole of the definitions of both cultural and natural heritage laid out in Articles 1 and 2 of the Convention”. It was further recognized that cultural heritage is not limited to specific material forms, and the concept of “cultural heritage” was distinguished into tangible and intangible heritage (UNESCO, 2003).

As human awareness of preservation gradually grew, came a long period of debate and exploration regarding how to excavation and protection of historical sites. Some of them advocated cleaning and restoring the ruins and recover the former glory, while others emphasized maintaining the original state of the sites and avoiding human alteration. Perhaps the most famous argue in this period (19th century) was the opposing views between Viollet-le-Duc and John Ruskin. Viollet-le-Duc believed “to restore a building is not to preserve it, to repair, or rebuild it, it is to reinstate it in a condition of completeness that could never have existed at any given time” (Hearn, 1990), while Ruskin claimed that “regardless of the carefulness of the restorer, it was an “imitation still, a cold model” (Jackson, 2006). The conflict of these two parties essentially represents a binary discussion on the necessity of restoration, which laid a profound foundation for the following development of the concept of heritage preservation.

1.1.1.2 Evolution of conservation concept

During the same period, with the colonial expansion of European and American, many relics were “often mined like mineral deposits” under the name of archaeology (Sharer & Ashmore, 1988). In the first half of the 20th century, with the catastrophic destruction caused by the world wars and the development of related disciplines, the international community gradually recognized the non-renewable property of heritage sites. *the Athens Charter* (International Council of Museums, 1931) directly required that excessive cleaning and reconstruction must be avoid during excavation, while t*he Venice Charter* (ICOMOS, 1964) further emphasized that sites should preserve their historical traces and environmental characteristics as much as possible. Regardless of the limitations of the era, the foresight of

policymakers regarding the true value of historical heritage was absolutely admirable.

However, due to the immaturity of contemporary theoretical frameworks and scientific techniques, archaeological sites and excavated artifacts were sometimes damaged or even completely destroyed during excavation, resulting in the irreversible loss of a large amount of valuable information (Jia, 2025) (Anadolu Agency, 2021).

In 1990, *the Lausanne Charter* (ICOMOS, 1990) defined that “Excavation should be carried out on sites and monuments threatened by development, land-use change, looting, or natural deterioration… If the site is non-threatened, excavation must be preceded by thorough scientific evaluation of the significance of the site”, which remains the primary principle that excavation work must follow to this day.

1.1.2 Trends in establishing digital archives

In the context of the 21st century, two particularly notable changes have emerged in heritage conservation practices:

1) The Advent of the Information Age

“The past generation had only the film camera, paper and pencil, tape measures and slide rules.” (Remondino & Stylianidis, 2016) The rapid development of science and technology has undoubtedly provided great convenience for the protection of these precious heritage sites and relics. Looking back at the technological advancements, a variety of methods have been adopted across disciplines: different laser scanning technologies are used to capture high-precision three-dimensional geometric data of the site's topography, buildings, and artifacts, while aerial photography and photogrammetry following a photogrammetric approach are employed to generate three-dimensional models (Spanò, 2025). Multispectral and hyperspectral imaging further expand the visible range, allowing invisible traces to be identified and analyzed under non-destructive conditions (Santoro, Wu, Patrucco, & Spanò, 2025). In the subsequent data processing process, the application of geographic information system (GIS) provides spatial analysis tools (Katsianis et al., 2008), and the emergence of Building Information Modeling (BIM) has greatly improved the efficiency of information integration and management (Garagnani, Gaucci, & Gruska, 2016).

2) The Arise of the Concept of Sustainable Development

However, the double-edged nature of technological progress cannot be ignored. While enjoying the conveniences it brings in many areas, the environment is also facing many unprecedented pressures. Extreme weather, natural disasters, and even social unrest may all pose unpredictable threats to cultural heritage. The emergence of the concept of sustainability aligns closely with the trend of digital archiving (Roussel & De Luca, 2023). Scholars have begun integrating digital

archives with tools such as big data and artificial intelligence to conduct risk assessment and scenario simulation for cultural heritage. This approach enables managers to pre-propose appropriate protection strategies before potential risks happen, thereby extending the lifespan of cultural heritage.

At the same time, from the public's perspective, digital archives of cultural heritage provide a much more engaging and accessible channels (Carvalho & Matos, 2018). Multimedia technologies translate research findings into easily understandable language, presenting professional information in ways that are more approachable for general audiences (Kong, 2025). This practice not only helps to disperse tourism pressure and reduce the impact of frequent activities on fragile sites, but also inspires public interest in cultural heritage. Undoubtedly, it provides extensive social support for heritage preservation, allowing culture to truly live on beyond research institutes and museums.

In summary, new technologies and concepts allow for the analysis and application of multi-dimensional scaling (Stanco, Battiato, & Gallo, 2011):

At landscape scales, digital 3D modeling and data analysis allow archaeologists to integrate different archaeological features and physical context without breaks, in order to better document the area. At monument/site scale, 3D techniques can deliver accurate measurements and objective documentation as well as a new aspect from a different point of view. At artifact scale, 3D modeling enables the reproduction of accurate digital/physical replicas of every artifact that can be studied, measured and displayed, while also providing data for public access, virtual restoration and conservation (Patrucco, Bambridge, Giulio Tonolo, Markey, & Spanò, 2023).

In all of these cases, clear and accurate initial information are essential. Based on this fundamental requirement, the necessity of establishing digital archives for cultural heritage can be summarized in several aspects and directions. Due to the large number of cases, only representative examples are presented (Table. 1).

Table. 1 Application of Digital Archives of Cultural Heritage

Field	Purpose	Tools	Value
Archival / archaeological heritage	Physical information archive of the target	High-precision scanning, high-definition image acquisition, 3D modeling, etc.	By digitally recording the shape, patterns, materials and other details of the heritage, the complete information is preserved, providing a reliable digital copy for future research and inheritance.
	Archives management and classification	BIM, HBIM, etc.	Through visual management mode, it provides clear and efficient digital archives and provides a platform for archive management and cross-disciplinary research.
Landscape / Architectural heritage	Geographic Information Analysis	GIS、spectral analysis, etc.	Allows for large-scale information extraction and exploration, broadens perspectives while improving work efficiency and reducing damage to property itself
Methods Innovation	Risk assessment and prediction	Big data analysis, artificial intelligence simulation, etc.	Provide early warning for property protection, pay timely attention to target status, and achieve preventive protection against extreme climate and disaster risks
	Cultural heritage Restoration	Virtual cultural relics restoration, etc.	Use digital technology to simulate restoration work, provide accurate data, reduce physical operation risks, and view preview effects in real time
Dissemination	Serving public education	Virtual museums, online interactive platforms, offline multimedia exhibitions, etc.	Translate professional knowledge into popular language, expand the audience, enhance public awareness and protection, and promote cultural heritage

1.2 Thesis Objectives and Structure Organization

According to the background outlined, this thesis focuses on the widespread challenges currently confronting cultural heritage sites, and aims to examine strategies for employing digital technologies in heritage conservation and dissemination through practical application.

Archeological site the Old Nisa, the former capital of the Parthian Dynasty has been chosen as the research object. The research establishes a complete workflow that covers on-site geomatic survey, advanced processing of raw point cloud data, analysis of refined point clouds and generation of derivative products, as well as the subsequent refinement and secondary creation based on these derivative outputs.

The organization of this thesis follows the progression of the project and is divided into six chapters, which are briefly summarized below:

1) Chapter 1

The chapter provides the overall research background by reviewing the origins and key concepts of cultural heritage and heritage protection, clarifies the necessity and contemporary trend of establishing digital archives, thereby defining the research objectives and workflow of the thesis.

2) Chapter 2

This chapter introduces the historical, cultural, and geographical context of Old Nisa. Architectural features, excavation history, and current conservation challenges of the site are outlined according to archaeological discoveries, offering crucial references for the subsequent workflow.

3) Chapter 3

This chapter presents the geomatic survey strategy assigned by the characteristics of Old Nisa, explains the measurement principles, special focuses on the theoretical background of Light Detection and Ranging (LiDAR), including the involvement of Terrestrial Laser Scanning (TLS) and Simultaneous Localization

and Mapping (SLAM), further introduced the establishment of the geospatial control network and data acquisition procedures (practical operation of TLS and SLAM).

4) Chapter 4

This chapter based on acquired point cloud data, introduced the elaborates on the processing procedure, including point cloud denoising, calibration, integration and verification, 3D mesh (digital model) reconstruction, and preliminary GIS analysis based on the Digital Elevation Model (DEM).

5) Chapter 5

This chapter describes the workflow for physically reconstructing the site through 3D printing, including model structure planning, theoretical foundations of the adopted 3D printing technologies, mesh pre-processing, printing tests, and the final assembly of the model.

6) Chapter 6

This chapter outlines the theoretical background of video mapping (projection mapping), the development of exhibition strategies and storyboards arrangement, the production of visual effects, and the evaluation of the final outcomes of its integration with the 3D-printed model.

Chapter 2: Background of the Old Nisa

2.1 History of Old Nisa

The Parthian Empire which stretching across the Eurasian continent, served as the intersection of Eastern and Western civilizations, is often called the as a "crossroads of history" (UNESCO World Heritage Centre, 2007a).

In the 5th and 4th centuries BC, the Parni/Parthians, a tribe of the Scythian confederation of the Dahi from the regions around the Aral Sea, settle in Parthava/Parthyene (present-day south-central Turkmenistan). By the middle of 3rd century BC, they gradually gained control of the region under the leadership of King Arsaces, and from which the name Arsacid dynasty was derived (The Editors of Encyclopaedia Britannica, n.d.a). In the first half of the 2nd extending from Margiana to the Euphrates River, and the city of Mithradatkert was founded, also known as the Old Nisa (Bruno, 2019)(Fig. 1, a).

In the second half of the 2nd century BC, they engaged in conflicts with Central Asian nomadic groups (Yuezhi). At the same time, China for the first time sent envoys to the Arsacid Empire (known in Chinese as Anxi) (Wang, 2022), and began trade along the routes that later became known as the Silk Road (Fig. 1, b).

Entering the 1st century BC, Parthia made its first contact with Rome in the late years of Mithridates II, after which relations between the two powers grew increasingly tense. In 54 BC, M. Licinius Crassus was defeated by the Parthians at Carrhae (The Editors of Encyclopaedia Britannica, n.d.b), which deepened the confrontation between the two sides. In 20 BC, Rome and Parthia reached a

Fig. 1 Evolution of the Parthian region in early stage

settlement during the reign of Augustus, and the Romans recovered the military standards lost by Crassus. During the 1st and 2nd centuries CE, the Roman Empire continued to expand in the Near East, conflicts with Parthia were frequent, and the frontier shifted from time to time because of warfare but generally followed the Euphrates River ((Fig. 2, c).

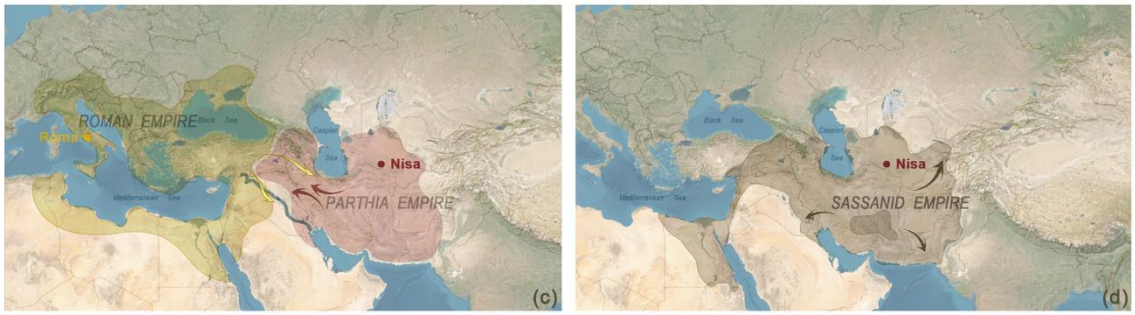

Fig. 2 Evolution of the Parthian region in later stage

In this period, under growing pressure from the west, the power center of Parthian royal family gradually moved westward to the later capital, Ctesiphon (The Editors of Encyclopaedia Britannica, n.d.c). The Parthian dynasty was finally replaced by the Sasanian Persian Empire in 223/224 CE, and its ancient capital Nisa gradually faded from historical memory (Keshavarz Rahbar, 2024) (Fig. 2, d).

In the early 19th century, based on the preservation of the toponym “Nisa”, British traveler D. Kinneir suggested linking the grand ruins located about 16 kilometers

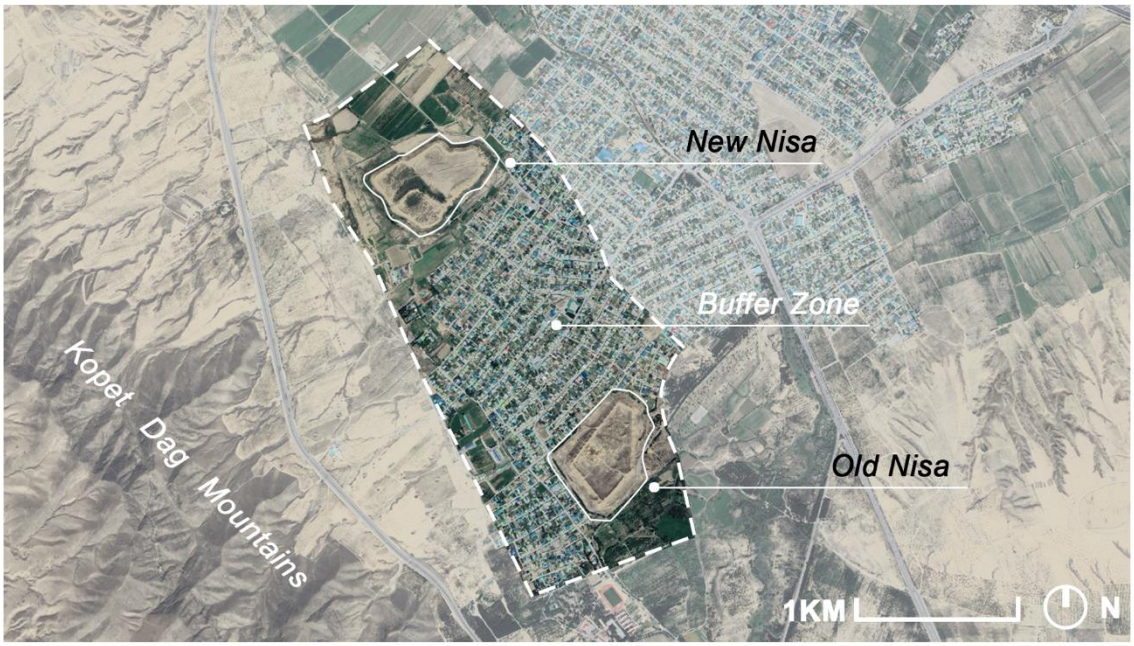

Fig. 3 Satellite view of Ashgabat suburbs – the Old Nisa and New Nisa area

west of modern-day Ashgabat (the capital of Turkmenistan), with the name “Parthaunisa” mentioned in classical sources (Lippolis, 2025). From these ruins, the once- splendid civilization of the Parthian Empire came into view once again.

The Old Nisa lies at the northern foothills of the Kopet Dagh and consists of two closely connected centers, known as New Nisa and Old Nisa, both surrounded by massive defensive walls (Fig. 3).

In 1925, the Ashgabat Regional Museum of History conducted the first surface survey at the site of Old Nisa (Lippolis et al., 2011), for identifying the royal tombs mentioned in the travel record of Isidoro di Carace (1st century BC - 1st century AD). In the 1930s, under the direction of A.A. Maruščenko, the Turkmen Institute of History initiated the first stratigraphic excavations at the site. Between 1946 and 1967, the Soviet Union conducted large-scale archaeological investigations as part of the JuTAKE mission. This period marked a breaking era of discovery, whose sensational results (Masson & Pugačenkova, 1982) rekindled scientific interest in Parthian culture. Over the past three decades, excavation work has been carried out alternately by the Russian Academy of Sciences in Moscow, the Archaeological Institute of Leningrad, and the Turin Archaeological Mission (the latter active since 1990) (Fig. 4).

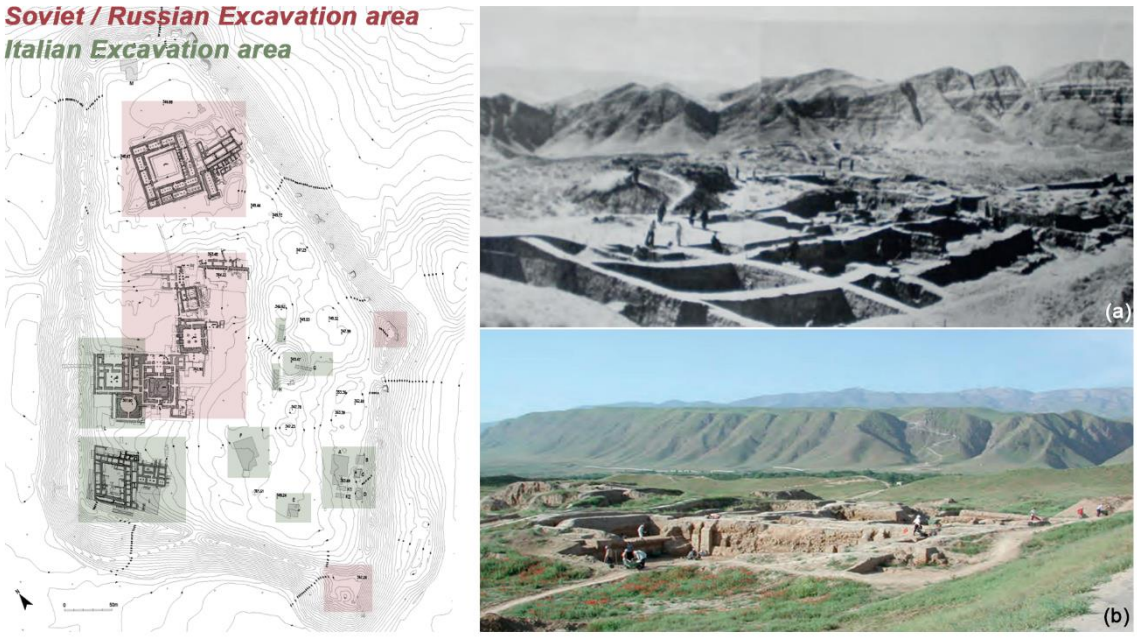

Fig. 4 (a) Nisa Parthica, JuTAKE excavations in the late 1940s
(b) Nisa Parthica, Italian Mission excavations in the Red Building

For the study of Central Asia and Parthian culture, the Old Nisa stands out as a crucial starting point for understanding the artistic, architectural directions and characteristics of the early Arsacid period. Entering the 21th century, archaeological mission primarily led by the Turin team shifted toward broader research objectives, focusing on patterns and dynamics of the diffusion of Hellenistic culture across Asia and interactions with Iranian traditions. In 2007, the New Nisa and the Old Nisa were added to the UNESCO World Heritage List (UNESCO World Heritage Centre, 2007b) together, acknowledging their outstanding value and ensuring their proper protection.

zBased on the preserved material remains and architectural forms, the New Nisa is considered as the actual urban settlement of ordinary inhabitants, consisting of a fortress and an underground town. Approximately 1 kilometer to its east lies the Old Nisa, now widely regarded to be a monumental complex dedicated to the rulers of the Parthian Empire and named after its founder, Arsaces (Lippolis et al., 2011). Archaeological excavations at Old Nisa have uncovered grand architectural structures, numerous inscribed documents, a plenty of treasury as well as a wealth of Hellenistic artworks and a large number of ivory rhytons whose rims are decorated with scenes drawn from Iranian themes or classical mythology. In fact, nearly all of the artistic and architectural remains discovered at the site reveal a fusion of Western and Iranian styles (Britannica Editors, 2025). The discoveries at Old Nisa have filled significant gaps in the understanding of Parthian civilization, and have powerfully confirmed its historical role as a key joint of cultural exchange between East and West (Fig. 5).

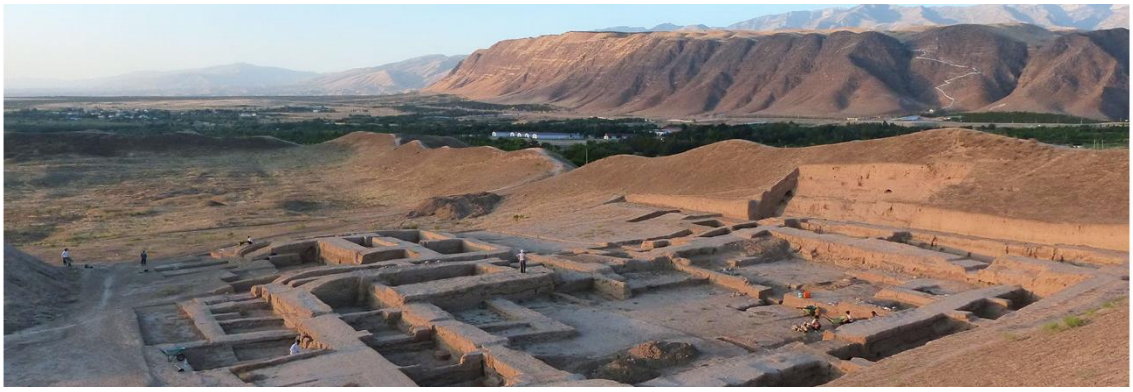

Fig. 5 Landscape of the Old Nisa

2.2 Archaeological Discoveries in Old Nisa

2.2.1 Geographical features of the site

The fortress of Old Nisa was constructed on the top of a natural hillside, the summit of the hill had been leveled and reinforced with multiple layers of compacted earth (UNESCO World Heritage Centre, 2007b). Its highest point lies at the southwest corner of the defensive tower, rising approximately 40 meters above the surrounding plain, with the base of the walls merging into the flatlands through slow slopes. The entire outline of the fortress forms an irregular pentagon, with a total area about 14 hectares.

The towering earthen walls around the city strongly emphasize its defensive character, echoing the historical conflicts between the northern Parthian world and the Iranian polities to the south. The exact number and positions of gates remain uncertain, though the main entrance was most likely located at the center of the western wall. Today, the remains of 40 defensive towers can still be traced along the walls, most concentrated on the eastern side, with the best-preserved foundations situated at the southeast corner. By contrast, the western side displays significant damage, likely caused by human activity or natural erosion. At the foot of the hill, visible accumulations of soil mark the boundaries of the site. To the northeast of the site lies a smaller hill, now separated from the main complex by a modern road. The terrain of the site is characterized by the region’s typical sandy soil, with shrubs scattered across in the field (Fig. 6).

Fig. 6 Current situation of the Old Nisa

2.2.2 Architectural traces and unearthed cultural relics in the site

The traces of human activity within Old Nisa are concentrated mainly in the northern and central architectural complexes, where variations in building forms reveal a clear functional zoning of the fortress. Other unexcavated areas remain buried beneath the modern soil layer.

On the northern side stands a massive square structure excavated during the Soviet period, which is referred to as the "*Square House*" (UNESCO World Heritage Centre, 2007b), in dimension 60m x 60m (Fig. 7).

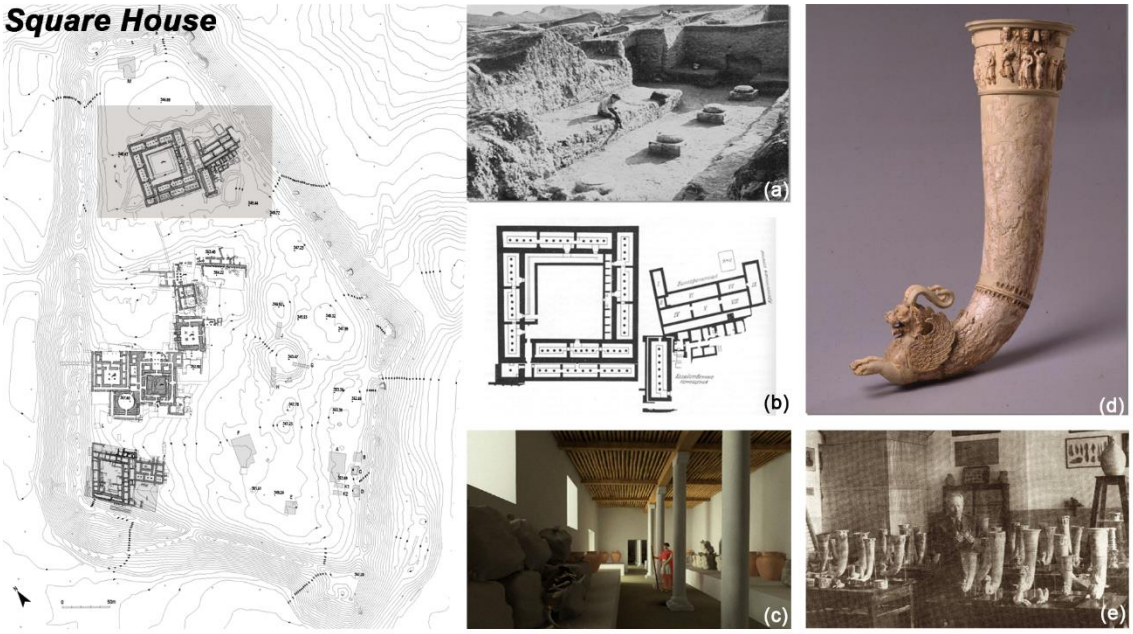

Fig. 7 The excavation site of the Square House, speculative reconstruction, and unearthed treasures the rhytons

The house is made of unfired bricks (the main building material), with smooth exterior walls and an entrance on its southern side. Three connected rectangular rooms are arranged around a courtyard with porticoes on both sides. The rooms are equipped with flat roofs supported by central wooden supports, whose stone foundations are still preserved today. A quite number of famous art works were found inside the modular rooms, include weapons, coins, metal statues, marble sculptures, and the most importantly 55 exquisite rhytons (Lippolis, 2025). Initially, this discovery was thought to confirm that the site had served as a royal treasury, however recently it has been suggested that it may originally have been used as a

ceremonial venue. Adjacent to the eastern side of the *Square House* lies a large warehouse, where approximately 2,800 inscribed pottery fragments were unearthed, providing valuable insights into the management of commodities at the time, particularly the handling of food and beverages.

The core of the site is the "*Central Complex*" (Lippolis, 2025), which consists of a group of monumental structures, including the *Red Building*, the *Palace* (northeast building N-E), the *Square Hall*, the *Tower Building*, and the *Round Hall* (Fig. 8). Except for the *Red Building* which dates back to the original city-building period under Mithridates I, all other structures belong to the same program:

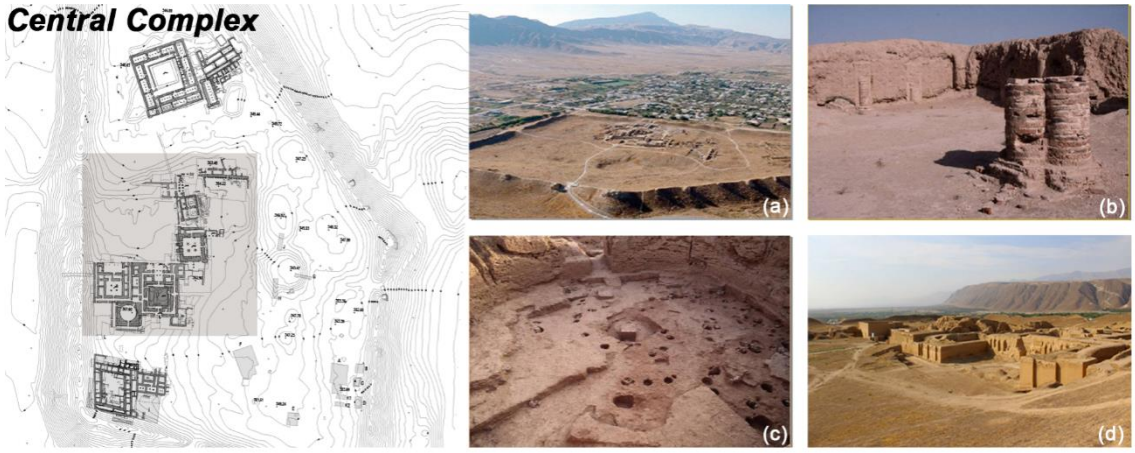

Fig. 8 Situation of the Central Complex

1) *Red Building*

Due to its strong symbolic significance, its original layout has been preserved and remains in use to this day (Fig. 9).

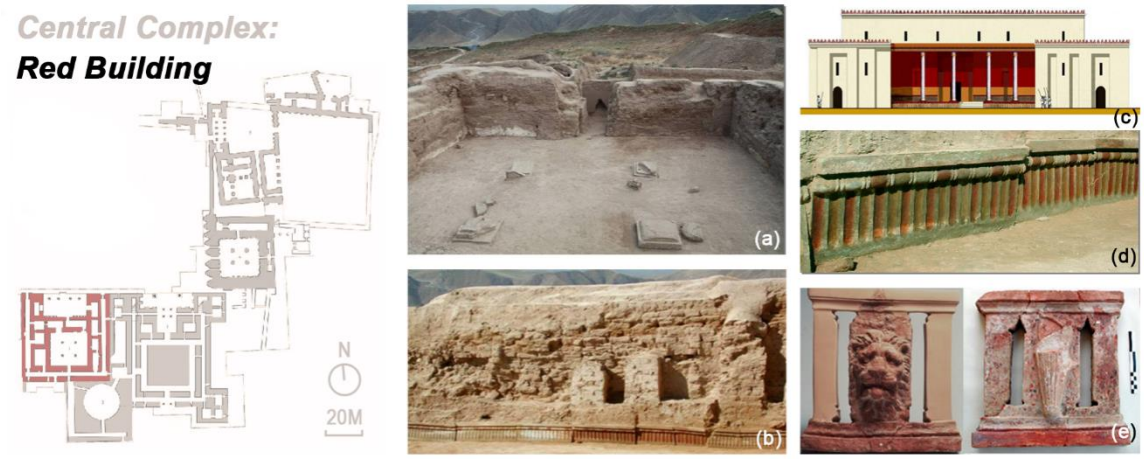

Fig. 9 The remaining column bases of the Red Building, speculative reconstruction, and unearthed red architectural decorative pieces

2) *Square Hall*

The feature of the building is the central hall supported by four columns and a triple entrance. The second floor housed large, finely crafted unbaked clay statues, indicating that it served as a display gallery for heroes or deified ancestors (Staraja Nisa, 1996) (Fig. 10).

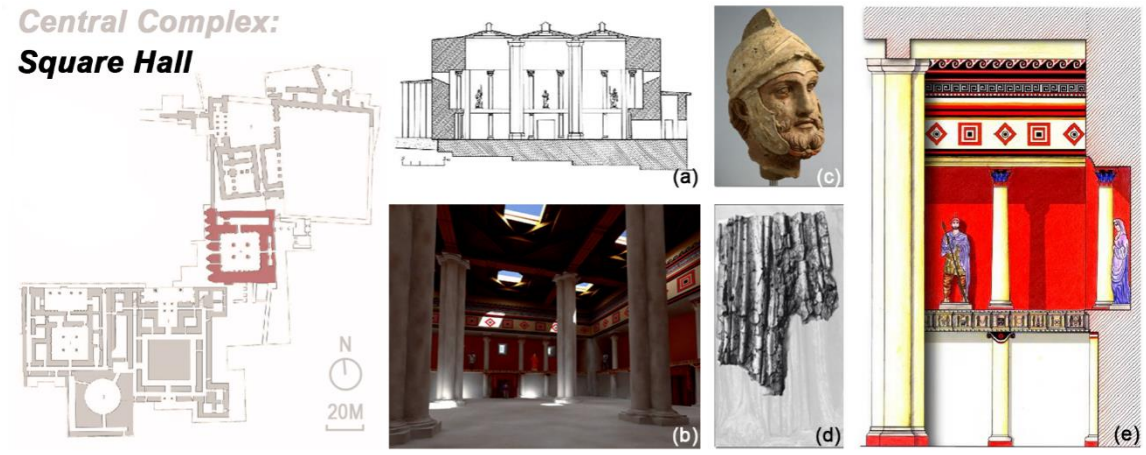

Fig. 10 The terracotta sculpture fragments unearthed from the Square Hall (fig. c presumably Mithridates) and the architectural reconstruction

3) *Tower Building*

The layout of the towers reflects strong influences from Iranian and Central Asian traditions and carries sacred symbolic significance, with interior decorations including a highly valuable painting depicting cavalry in nomadic attire engaged in combat (Pilipko, 2015) (Fig. 11).

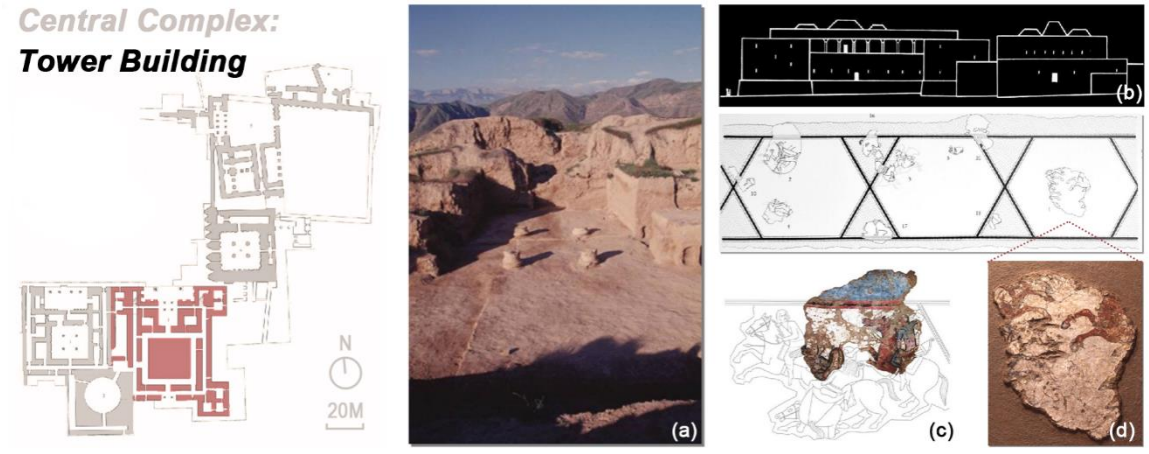

Fig. 11 The situation of the Tower Building and unearthed Colorful decorative pieces

4) *Round Hall*

The circular shape and scale of the hall further emphasize its sacred significance. The hall was initially believed to be a temple of heroes, while later identified as a monument of the Parthian royal family. Italian researchers have made significant contributions to the architectural study of the *Round Hall*, proposing a reconstruction scheme differing from earlier excavators (Fig. 12). This reconstruction displayed a reasonable semi-elliptical raw brick dome, which is the first such structure discovered in Parthia and beyond. These buildings feature mud-brick walls coated with white plaster, sometimes painted in red, ochre, black, or green, and decorated with geometric, floral, and figural patterns. The architectural features along with the discovered sculpture fragments and murals indicate their ceremonial functions, intended to commemorate and glorify the rulers and the history of the Parthian Empire. Furthermore, fragments of terracotta statues in purely Greek-style were unearthed in this area, together with those in typical Iranian clothing (Lippolis, 2025).

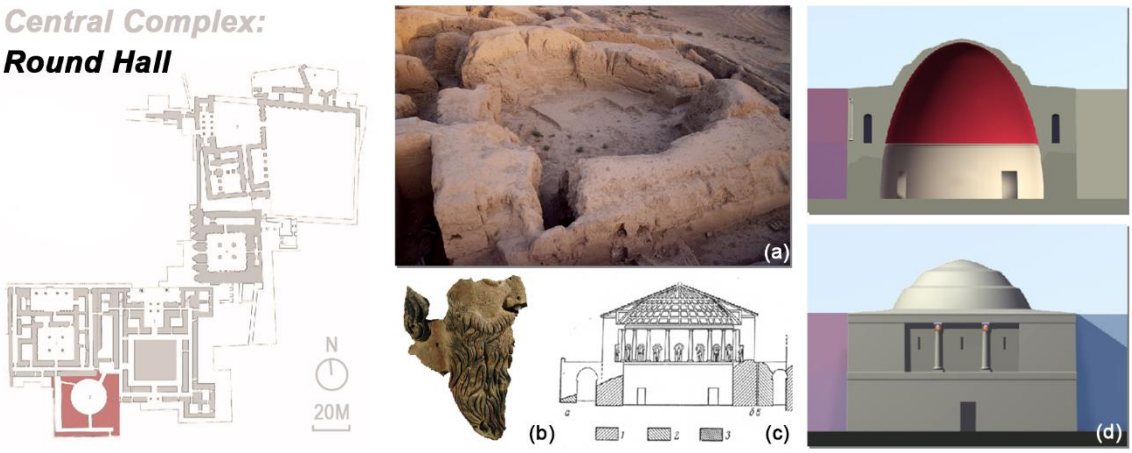

Fig. 12 Early architectural reconstruction speculations (c)
Recent new speculations by Italian archaeologists (d)

5) *N-E Building / Palace*

The layout of the palace is only partially known, a spacious open area, likely used for banquets and collective ceremonies (Staraja Nisa, 2001).

Between the northern and central building groups lies a paved cannel and several ancillary structures (UNESCO World Heritage Centre, 2007b). In the central urban area, a clearly sunken zone is observed between the waterways, which is presumed to have functioned as a reservoir (*water basin*). Water was likely drawn from an external source, passed through the channel and stored in the internal reservoir, then discharged from the opposite side.

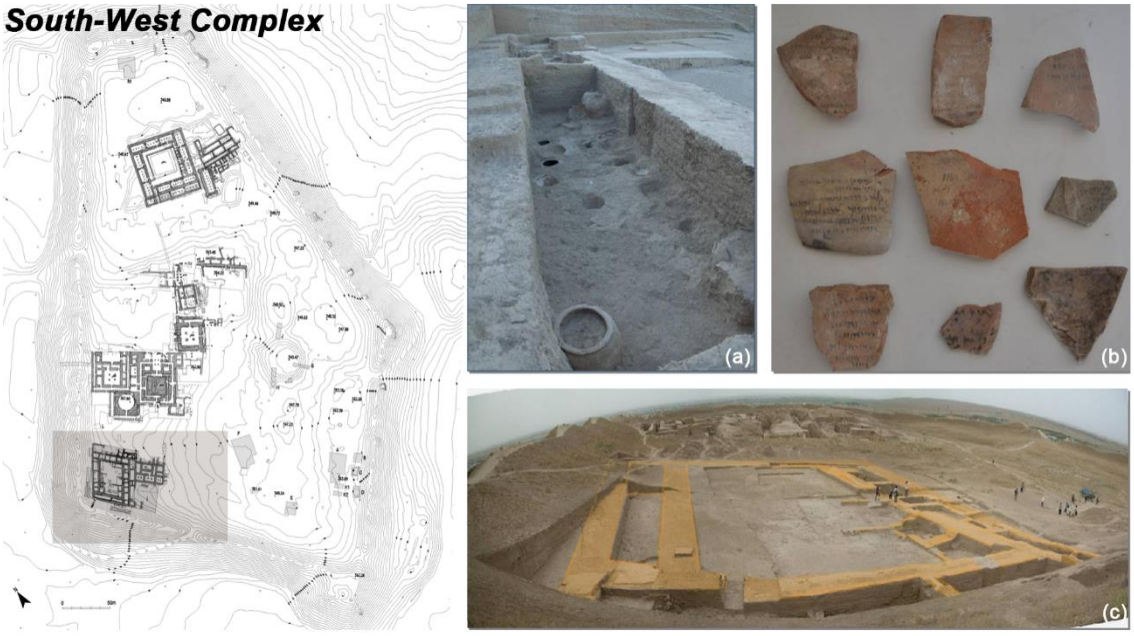

Fig. 13 Recent excavations in the Southwest and the discovery of inscribed pottery shards

In recent years, the Turin Archaeological Research Center has opened new investigation areas on the southwestern and southeastern sides (Fig. 13). Excavations on the southwestern side have revealed a large storage and production area, with rooms arranged around a spacious courtyard, including a dedicated zone for plaster and stucco work. A nearby building contains a row of cylindrical rooms, which may have served residential or ceremonial purposes (Lippolis, 2025). Further information is expected as excavations progresses.

2.2.3 Current status of the site and protection measures

At Old Nisa, it's estimated that approximately half of the site remains untouched and thus remains stable. However, in the decades following the start of archaeological activities, the exposed structures remained unprotected and suffered erosion from natural and human activities. Some protective measures have been implemented (UNESCO World Heritage Centre, 2007b): the addition of fired bricks to the ancient brick columns was intended only to reinforce the remaining original column bases, protecting them from seasonal rain and frost and preventing climbing (Fig. 14).

On the other hand, even after the site was opened to visitors, no large-scale restoration work was carried out. Concrete paving was installed to provide clear pathways for tourists, protecting the archaeological site and it remains from frequent human activity. Although these measures have been effective, their discordant colors and styles have occasionally been criticized (Fig. 14).

In spite of the growing awareness of preservation is encouraging, certain challenges remain, such as drainage in complex terrain. In addition, there are still some unknown factors, such as local seismic activity and increasing pressure from tourism. For these reasons, it is crucial for researchers to maintain a constant watch over the site and conduct timely digitization and documentation. The site contains a wealth of information and numerous points of interest, of which will serve as a reference for the completion of the projected story board in Chapter 6.

Fig. 14 Protective intervention methods: ground paving and brick addition

Chapter 3: Data collection of point cloud

3.1 Tools Involved and Related in the Survey

To achieve the digitalization of heritage sites, it is necessary to have a systematic understanding of its technical means, and a variety of surveying and mapping methods have been developed by today. Selecting appropriate techniques according to specific scenarios and integrating interdisciplinary skills will also contribute to improve work efficiency and ensure data accuracy.

This section will introduce the technologies used in this survey, analyze their advantages and disadvantages, and briefly discuss technologies that were not adopted but may hold potential value.

3.1.1 Working background：Establishment of geospatial control framework

Regardless of the data acquisition technique employed, ensuring that all datasets can cooperate within a unified environment is the basement.

Therefore, the first step involves establishing a reference system integrated with global geospatial information and setting up a network of control points. This process typically combines the use of the Global Navigation Satellite System (GNSS) and a Total Station to construct a georeferenced framework (Spanò, 2025). The GNSS provides an absolute reference system corresponding to real-world geographic coordinates, while the total station establishes a relative local reference system that simplifies measurements without incorporating absolute geolocation information (Ogundare, 2015) (Chapter 3.2.1 will detail the construction of absolute and relative coordinate systems in surveys).

Through the collaboration between these two systems, the uniformity and precision of the reference framework can be ensured. The feasibility of this workflow has been validated through practical applications in multiple fields involved in geomatics.

3.1.1.1 GNSS system

The principle of GNSS surveying is to determine the absolute coordinate position of a ground point by measuring the distances between satellites and ground-based receivers and applying spatial geometric relationships (Langley, Teunissen, & Montenbruck, 2017). Essentially, this process relies on satellite signal-based trilateration. The receiver captures signals from at least four satellites at the same time, and calculate the distances from each satellite to the receiver based on the signal propagation time and the speed of light. Subsequently, the receiver's longitude, latitude, elevation, and clock bias are derived. The coordinate system established in this manner typically follows a global geodetic reference framework, most commonly the World Geodetic System 1984 (WGS 84) (Capra et al., 2015), enabling the standardized recording of observation point coordinates (Fig. 15).

Depending on the required precision and field conditions, GNSS coordinate determination can be performed in static mode, which achieves millimeter-level accuracy through long-duration cumulative observations (Zhang, Niu, &

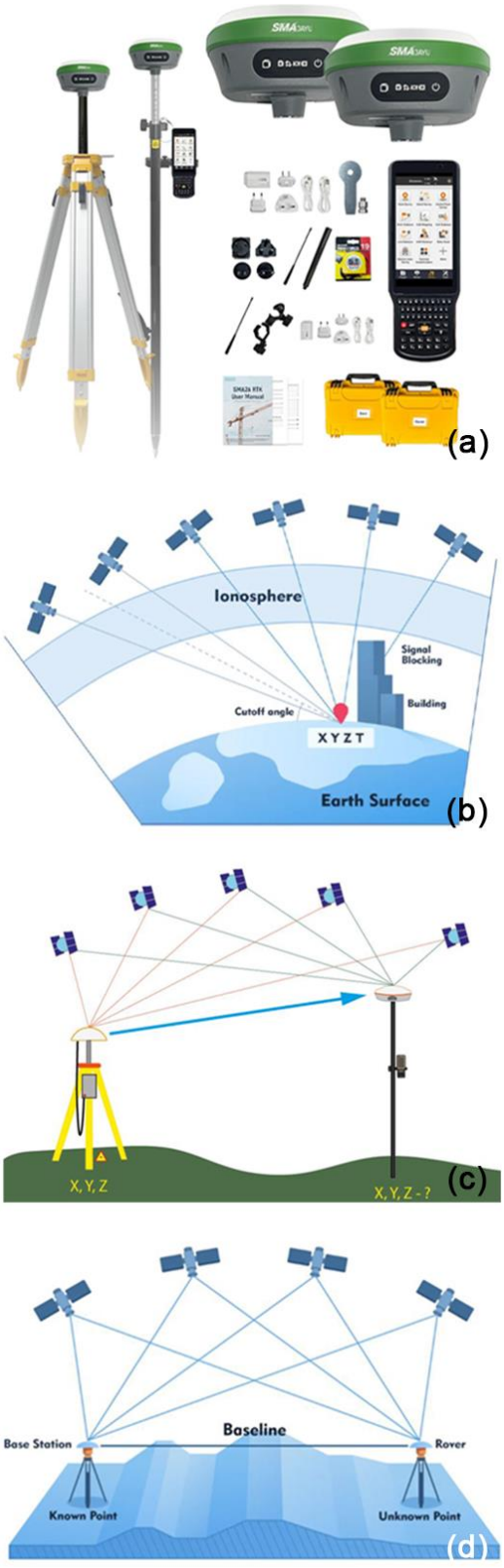

Fig. 15 (a) Common instruments for GNSS measurement
(b) GNSS measurement principle
(c) RTK measurement principle
(d) DGNSS calibration method

Shi, 2019); or in real-time kinematic (RTK) mode (Garrido-Carretero et al., 2019), which sacrifices a certain degree of precision in exchange for greater flexibility and rapid measurements (Fig. 15).

The accuracy of GNSS measurements is influenced by multiple factors, including satellite orbital errors, signal propagation delays, and observational noise. To control these errors, the Differential GNSS (DGNSS) technique is commonly used (Gebre-Egziabher & Gleason, 2009). The fundamental principle involves using a reference station with known coordinates, which later receives signals from the same satellites as the point to be test. By comparing the two sets of observations, the positional errors at the rover can be reduced, thereby improving the overall measurement accuracy (Fig. 15).

However, since GNSS surveying relies on satellite signals, its operational environment will be limited. Moreover, GNSS measurements often cannot fully meet the requirements in terms of precision and point locations (e.g. on facades). Therefore, GNSS data are commonly supplemented and refined using more precise Total Station observation system, which provide a higher resolution and supplement (Capra et al., 2015).

3.1.1.2 Total Station

Unlike GNSS surveying, a total station refines the local geometric relationships within the control network by measuring the horizontal angles, vertical angles, and slope distances between control points. It requires a reference point with known coordinates (which could be from GNSS), and by measuring the horizontal and vertical angles and the slope distance from this reference point to the target point, the coordinates of other target points can be computed through trigonometric calculation (Scherer & Lerma, 2009) (Fig. 16).

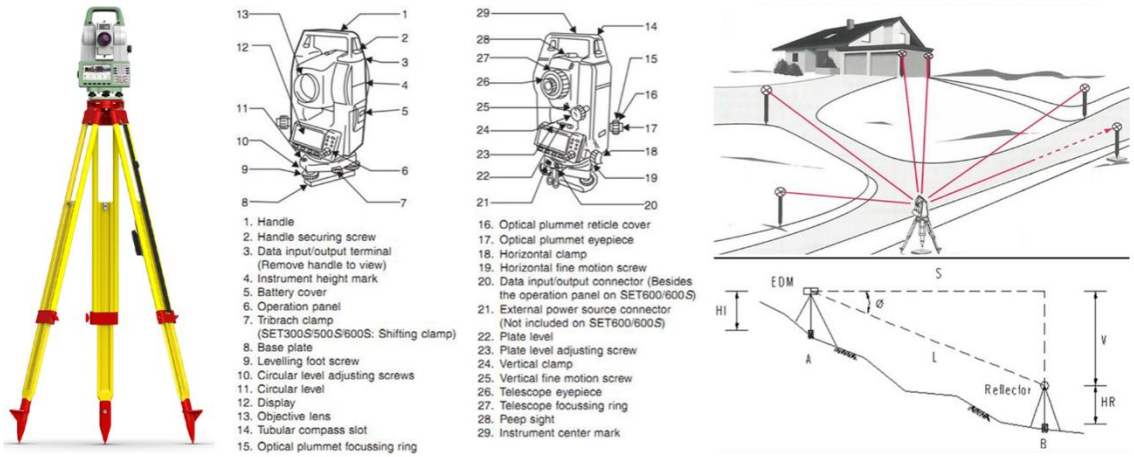

Fig. 16 Mechanical composition and operating logic of total station

Since this process directly determines relative positions based on optical angle measurement and electronic distance measurement, it can serve as a reliable surveying method in environments where GNSS signals are unavailable, such as indoor spaces or tunnels. Furthermore, because total stations offer higher precision in local measurements, they are also commonly used in the heritage domain to refine and densify GNSS-based control frameworks.

The measurement errors of a total station primarily arise from instrument calibration deviations, observational mistakes, or environmental changes that cause beam radiation (Mohammed, 2021). Instrument errors are often caused by factors such as misalignment of parts, calibration errors, and improper placement, while observational errors usually related with aiming problems or reading mistakes. Environmental disturbances, on the other hand, are often influenced by observation distance, changes in atmospheric pressure affecting the refractive index of air, and the curvature of the Earth.

The first two types of errors can be minimized through proper calibration and repeated measurements. Errors induced by environmental variations are typically corrected by using either offline or real-time adjustment computation software based on the Least Squares Adjustment principle (Karsznia, Osada, & Muszyński, 2023). Whatever, perfect measurement (beyond the capability of human skill or electronic instruments) does not exist, and an acceptable level of error tolerance must always be adopted when evaluating measurement results (Spanò, 2025).

3.1.1.3 Surveying tools and local systems

Similar to the total station, laser scanning instruments typically define a relative coordinate system when acquiring point cloud data, in order to describe the spatial structure in a local reference frame (Ogundare, 2015). As long as the positions of several feature control points are properly recorded, the relative and absolute coordinate systems can be easily transformed and aligned through specialized software (this process will be detailed in a later section). Such an approach not only reduces the computational load of the electronic instruments during data acquisition and post-processing, but also ensures the reliability in the local geometric structure once the control network is correctly aligned. However, since the accuracy of this control framework directly determines the reliability, operability, and quality of subsequent 3D reconstruction, the accuracy of this step is particularly important.

Table. 2 Comparison of GNSS & Total Station

Method	GNSS	Total Station
Time Consumption	Static mode in several hours or RTK in real-time	Relatively short, depends on number of control points
Reference system	Global	Local
Advantages	Efficient for large-scale control networks	High local accuracy and no-signal environments
Disadvantages	Signal easily blocked by obstacles, relatively low accuracy	Requires preliminary work
Applications	Establishment of overall geodetic framework	Dense local control network

3.1.2 The use of geomatic technology

Since the use of unmanned aerial vehicles (UAV) for photogrammetry was forbidden on site, oblique aerial imaging techniques which are typically suitable for large-scale area mapping were restricted. Considering that the site simultaneously features open ground and dense building complexes, a customized Light Detection and Ranging (LiDAR) approach was required, and the team adopted a combined surveying strategy using Terrestrial Laser Scanning (TLS) and Simultaneous Localization and Mapping (SLAM) techniques (Spanò, Patrucco, & Bonfanti, 2024). Consequently, this survey primarily relied on these two Light Detection and Ranging (LiDAR) methods for data acquisition.

3.1.2.1 LiDAR technology

Generally, Light Detection and Ranging (LiDAR) refers to a category of techniques for acquiring spatial information based on optical principles (Lemmens, 2011). Its core theory lies in calculating distance by precisely measuring the light path, and reconstructing three-dimensional spatial coordinates through the integration of angular information. LiDAR has been widely applied in various fields, including Terrestrial Laser Scanning (TLS), Mobile Mapping Systems (MMS), UAV-based LiDAR scanning, and eventually Spaceborne or space-based laser measurement systems for space exploration (Wang et al., 2020) (Fig. 17).

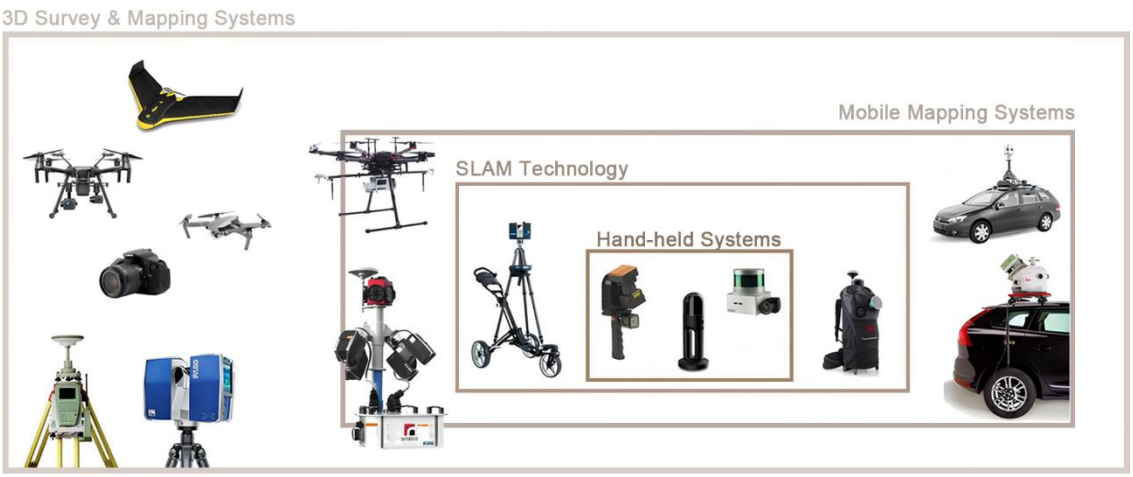

Fig. 17 Multiple surveying methods

Compared with traditional surveying methods, LiDAR offers advantages such as high speed, accuracy, and non-contact measurement. Laser scanning systems are capable of capturing the positions of a large number of points within a very short time. They operate based on measurement principles similar with total station, detecting each point by measuring two angles and one distance. The measurement of a point's three-dimensional position is first performed in spherical coordinates and then converted into Cartesian coordinates, calculated within the reference system integrated with the acquisition instrument (Spanò, 2025). The final collection of the three-dimensional coordinates of all measured points under local coordinate system is defined as "point cloud" (Autodesk, n.d.). At the same time, the scanner can acquire image data through an integrated camera, and assign color information to the point cloud after positional registration, enabling multi-perspective reconstruction of the scanned space (Lemmens, 2011).

The ranging principles of LiDAR mainly include two types: the Time of Flight (TOF) method and the Phase-based Scanning method (Spanò, 2025) (Fig. 18).

The former calculates distance by measuring the time interval between the emission and return of a laser pulse. Such systems generally have lower accuracy but a longer measurement range (up to several kilometers), making them suitable for large-scale outdoor site surveying. The latter determines distance by emitting a modulated laser beam and comparing the phase difference between the emitted and received signals. This method offers higher accuracy but a shorter range (on the order of hundreds of meters), making it more appropriate for higher scale measurements.

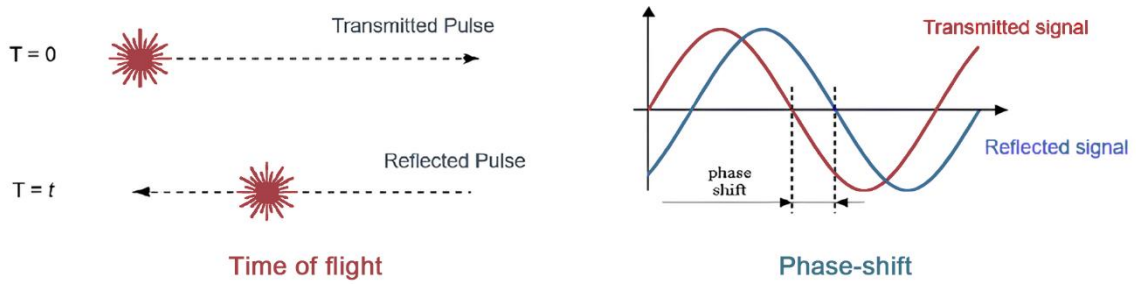

Fig. 18 Measure principle of TOF and Phase-based scanning method

The registration of different scanning datasets requires the identification of a sufficient number of common features. Since natural features are often insufficient to serve as the sole reliable reference, artificial reference targets are typically pre-arranged within the scanning site (FARO Technologies, n.d.a). At the architectural surveying scale, Spherical Targets or Checkerboard Targets (planar stickers composed of black and white grids) (Fig. 19) are usually adopted on site, in order to manually or automatically identify feature points. These points are then used to compute the relative poses (translation and rotation) between scanning stations, thereby achieving precise alignment of multi-station point clouds.

Fig. 19 Checkerboard targets used for on-site measurement point positioning

In addition, feature-based matching methods that rely on natural features (Rusu, Blodow, & Beetz, 2009) and the Iterative Closest Point (ICP) algorithm (which automatically detects the overlap ratio between point clouds through iterative optimization) (Rusinkiewicz & Levoy, 2001) can also assist in point cloud registration. These two approaches will be further introduced in the practical section later in this study.

3.1.2.2 TLS LiDAR system

The core objective of Terrestrial Laser Scanning (TLS) is to achieve stable, high-quality documentation of surveying targets, and it is currently one of the most essential and highly accurate three-dimensional recording technologies in the fields of archaeology, architecture, and cultural heritage conservation (Grussenmeyer et al., 2008). By systematically rotating in both horizontal and vertical directions, the scanner performs a comprehensive three-dimensional scan of the environment, acquiring millions to billions of spatial points within a short period of time to generate high-density, millimeter-level point cloud data (Lemmens, 2011) (Fig. 20).

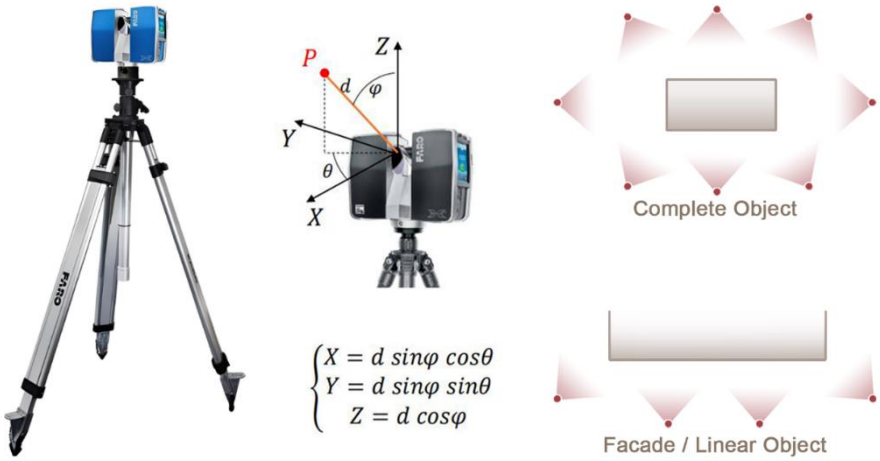

Fig. 20 FARO's TLS scanner as example. Scanning principle and measurement method

Since a single scan can only capture the visible surfaces within the instrument's line of sight, multiple scan positions are typically required to achieve a full-cover of the object. The datasets obtained from different scanning stations must then be manually or automatically registered using Iterative Closest Point (ICP) registration in the corresponding software, and subsequently integrated within a unified coordinate system (Fig. 20).

TLS devices are often equipped with high-resolution imaging units that simultaneously capture color photographs, enabling the generation of colored point clouds with realistic RGB attributes, thereby enhancing the overall informational richness of the resulting 3D model (Lemmens, 2011). The output data of Terrestrial Laser Scanning (TLS) are in the form of point clouds, in which each point contains

not only spatial coordinates but also intensity and color information (FARO Technologies, n.d.b). In which, the intensity value represents the strength of the returned laser signal, which is influenced by factors such as material reflectivity, incidence angle, and surface roughness. This parameter can assist in identifying different material or texture characteristics.

The sources of error in Terrestrial Laser Scanning (TLS) are similar to the total station. However, since TLS involves the acquisition of dense point clouds, its data quality is additionally influenced by several other factors. Above all, the beam divergence angle affects the projected area of a single laser pulse on the surface, which means the accuracy tends to decrease as the scanning distance increases. Environmental variations, such as dust, lighting, and temperature, can also cause refraction, strong reflection, or diffuse reflection, leading to signal attenuation or abnormal returns that result in noise or data voids. Insufficient overlap between scan stations or inaccurate target recognition may also leads to registration errors (Ogundare, 2015).

Furthermore, site constraints can limit the performance of TLS. Take buildings as an example of the target, in environments with dense occlusions (e.g., vegetation or debris) or complex spatial layouts, fine details are often difficult to capture completely. Overall, it is essential to carefully observe the scanning environment during the survey process and develop appropriate strategies to mitigate potential issues.

As a mature surveying technique, Terrestrial Laser Scanning (TLS) is beyond the traditional scope of two-dimensional documentation in heritage recording. Its high precision enables the complete capture of architectural and archaeological geometries as well as detailed surface textures, providing a highly reliable basis for various applications such as digital reconstruction, archaeological excavation (Lippolis, Spanò, Patrucco, & Messina, 2024), structural deformation analysis (Mukupa et al., 2017), and environmental risk assessment (Patrucco, Setragno, & Spanò, 2025).

Moreover, this kind of non-contact measurement approach minimizes potential

damage to the scanned objects. The comprehensive datasets acquired through TLS can be reused in later stages, reducing the need for repeated field visits and thereby aligning with sustainable principles in preservation, presentation, and research. High-quality TLS data can also be integrated with Building Information Modeling (BIM) (Mill, Alt, & Liias, 2013), Virtual Reality (VR), and video mapping platforms (Stanco, Battiato, & Gallo, 2011), providing a solid technological foundation for heritage visualization, education, and public engagement.

3.1.2.3 MMS & SLAM LiDAR system

Unlike traditional static or fixed-point surveying methods, the Mobile Mapping System (MMS) (Leica Geosystems, n.d.) enables continuous scanning of large-scale environments while in motion, allowing the surveyed objects/areas to be captured as complete three-dimensional digital models within a shorter period of time. It provides a flexible and mobile alternative to conventional static laser scanning, representing a significant breakthrough in the field of spatial data acquisition.

A typical MMS platform uses light detection and ranging (LiDAR) and/or high-resolution cameras as its primary sensors to acquire data for objects/areas of interest, and integrated with sensor suites for positioning and georeferencing, such as the global navigation satellite system (GNSS) and inertial measurement unit (IMU) (Elhashash, Albanwan, & Qin, 2022) (Fig. 21).

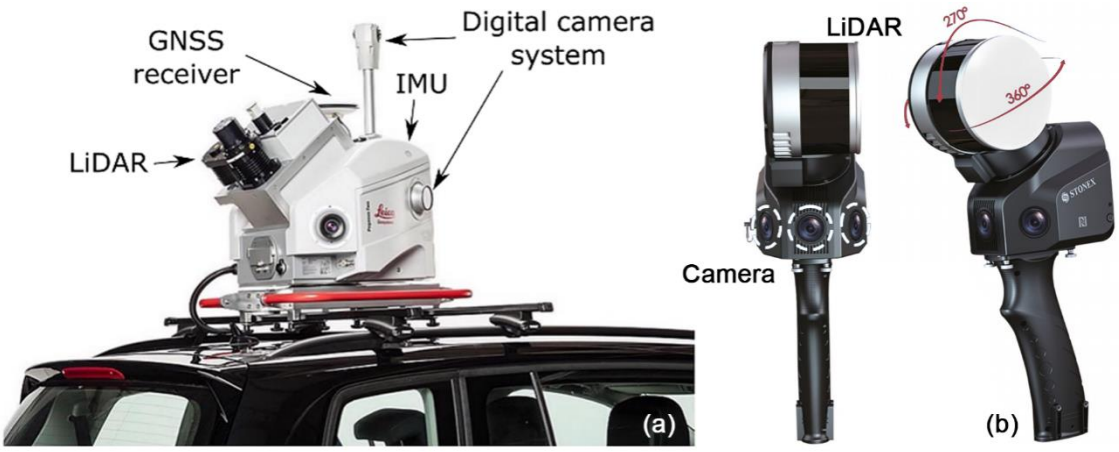

Fig. 21 Taking the vehicle-mounted MMS measurement system and the handheld scanner from Stonex as examples

In traditional Mobile Mapping Systems (MMS), the GNSS module provides positional references during movement, while the LiDAR sensor continuously scans the environment at high frequency, and the Inertial Measurement Unit (IMU) records angular velocity and acceleration to make up the limitations of GNSS during brief signal loss or high-frequency motion. However, in environments where GNSS signals are restricted such as indoor spaces, underground areas, or archaeological excavation sites, positioning methods that rely solely on external signals cannot ensure stability and continuity (Bosse & Zlot, 2009) (Fig. 21).

To address this issue, a SLAM-based (Simultaneous Localization and Mapping) approach has been introduced (Bosse, Zlot, & Flick, 2012). In these last years, this type of handheld 3D mapping technology has increasingly developed the framework of portable solutions for close-range mapping systems that have mainly been devoted to mapping the indoor building spaces of enclosed or underground environments, such as forestry applications and tunnels or mines (Sammartano & Spanò, 2018).

In SLAM-based MMS scanners, the system continuously captures point clouds of the environment while in motion and employs feature-matching algorithms to identify spatial correspondences between consecutive scans, thereby estimating the device's trajectory. As scanning progresses, the system incrementally accumulates data and expands the map. Through a Loop Closure mechanism (Labbé & Michaud, 2014), previously visited areas are detected, and then allowing the correction of errors and the construction of a point cloud map within a relative

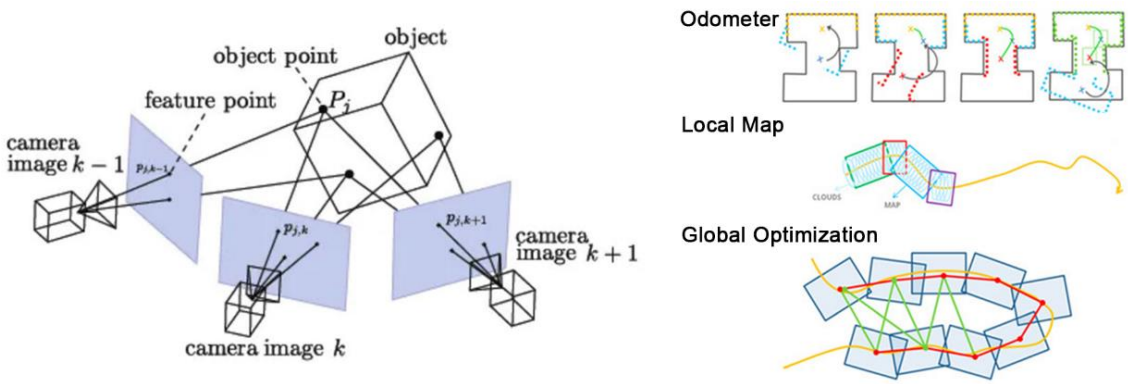

Fig. 22 Principles and processes of SLAM-based scanner component point cloud environment

reference frame, enabling self-referenced digital recording while navigating unknown spaces (Fig. 22).

Data from different sensors are unified using the timestamp, and fused through a Kalman filter algorithm (Qi & Moore, 2002) to jointly estimate the scanner's motion trajectory for reducing noise and cumulative errors. Furthermore, during traversal, the SLAM system should occasionally pause at pre-set checkpoints (Checkerboard locations) to ensure the accuracy and consistency of point cloud modeling.

Today, MMS scanners can be paired with various mobile applications for real-time monitoring (e.g., SLAM GO, Cavas, Scaniverse), enabling users to conveniently assess the preliminary scanning status and view the real-time generated scanning trajectory. Without relying on fixed survey stations or external references, operators can perform continuous surveying of complex spaces, significantly improving the efficiency and coverage of three-dimensional documentation.

In addition to the commonly mentioned sources of laser scanning errors, it should be noted that when conducting verification at very high scales and fine detail, some handheld laser scanners (e.g., ZEB series) produce derived models whose scale can be considered roughly equivalent to conventional architectural scales (e.g., 1:100 or 1:200). However, a 1:50 scale or higher is typically required to fully capture and process architectural details, necessitating the use of TLS-derived point clouds for higher precision (Spanò, Patrucco, & Bonfanti, 2024).

Moreover, during large-scale scanning of open areas, SLAM-based systems tend to exhibit more noise and drift compared to TLS. SLAM scans are also more sensitive to operator handling, and some complex scanning routes are also more likely lead to the misalignment of point cloud. Therefore, post-processing registration corrections and reference data from TLS remain critically important.

In summary, MMS and SLAM-based systems enable surveying tasks across a wide range of environments from indoor spaces to urban streets, allowing efficient three-dimensional modeling. Beyond mobile scenarios, they are also well-suited for operation in closed or narrow spaces. Although point cloud accuracy by SLAM

scanner is generally slightly lower than that of TLS (Szrek et al., 2024), they can still maintain a reasonably reliable error range in specific working conditions, which is sufficient to support structural analysis and morphological studies (Yiğit et al., 2024). With algorithmic iteration and hardware upgrades, this technology holds quite potential for further development.

3.1.2.4 Other potential survey technologies

Although the TLS + SLAM workflow can perform exceptionally well, some minor issues still persist. In this survey case, for example, due to limitations in working time and scanning trajectories, both methods (TLS/SLAM) exhibited partial information loss on the western ramp, which will be discussed in detail later. Therefore, it is worthwhile to explore potential optimization strategies to enable the rapid and comprehensive acquisition of site information.

1) UAV technology

It is reasonable to believe that, if conditions permit, the use of Unmanned Aerial Vehicle (UAV) surveying technology (also a type of MMS) (Spanò, 2025) (Nex & Remondino, 2014) can also contribute to the mutual validation of TLS and SLAM models. Furthermore, since it is estimated that roughly half of the Old Nisa site remains buried and untouched, and historical records regarding Old Nisa and the Parthian Empire are extremely limited (see in Chapter 2), identifying the locations of unexcavated areas is quiet challenging. In future research, using UAVs equipped with multispectral sensors to document and analyze the site may enable precise detection and excavation. This approach has the potential to significantly save the cost and resources required for fieldwork (Fig. 23).

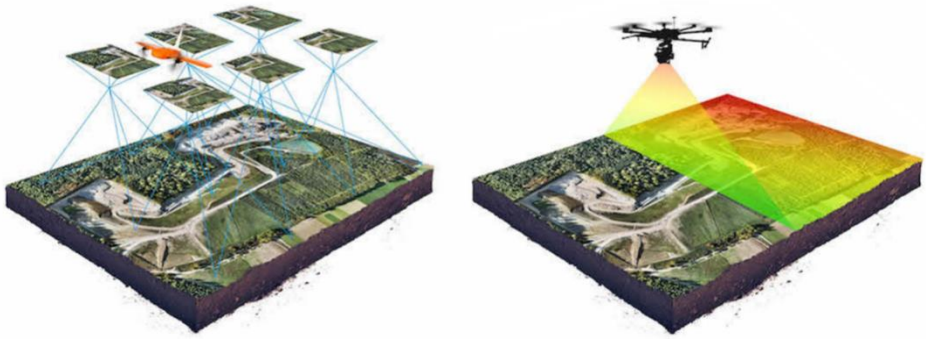

Fig. 23 Measurement methods of UAV oblique photography and multispectral detection

2) Photogrammetry technology

If rapid surveying of individual areas is required, photogrammetry based on digital cameras can also meet this need (Spanò, 2025) (Grussenmeyer et al., 2008). Compared with laser scanning which requires more time and complex operation, photogrammetry can acquire image data at lower economic and temporal costs, assisting in the rapid three-dimensional reconstruction of target objects (Fig. 24).

Fig. 24 Photogrammetry based on photo modeling provides high-overlap-rate photos from multiple angles, and uses algorithms to capture key point matching to generate models.

Table. 3 Comparison of the Mapping Tools

Method	Time Consumption	Advantages	Disadvantages	Applications
TLS	Medium/Long	Very high accuracy, high-density point clouds, reliable details	On-site operations are complex, time-consuming, easily affected by obstructions	High-precision architectural, geographic recording
MMS	Short	High efficiency, Suitable for complex environments	Accuracy relatively low	Indoor spaces, tunnels, underground ruins, large-area rapid recording
UAV	Short	Suitable for large-scale mapping, captures roofs and terrain, covers inaccessible areas	High equipment costs, regulatory and weather restrictions	Terrain modeling, geographic planning
Photo-grammetry	Short/Medium	Low cost, flexible operation	Accuracy relatively low	Rapid recording in building levels

3.2 Strategy and methodology: Point Cloud Data Collection

The 3D surveying work was carried out by the geomatics team of Politecnico di Torino and CRAST members, with two survey conducted at the Old Nisa archaeological site in May 2024 and April 2025, resulting in a complete, full-coverage point cloud of the site. Since the author did not participate in the field survey, the data in this chapter is mainly from the 2024 NISA Mapping Technology Report (Spanò, Patrucco, & Bonfanti, 2024).

This experiment aims to obtain two/three-dimensional measurement data with high-precision, develop a 3D printed model based on DSM (Digital Surface Model), perform geographic analysis on the site based on the 2D/3D data obtained from the survey, and finally project the analysis results onto the 3D printed model in a visual manner. In addition, the results of the survey of the Old Nisa will support archaeological research and other related needs.

As mentioned earlier, drone-based photogrammetry was prohibited on site, making oblique aerial photography for large-area coverage infeasible. Considering that the archaeological site comprises both open spaces and dense buildings existing, the team decided a targeted TLS + SLAM workflow (Spanò, Patrucco, & Bonfanti, 2024) to conduct a comprehensive three-dimensional survey of the entire city, involving buildings, excavated and unexcavated areas, external and internal sides of the city walls, and the surroundings.

The terrestrial laser scanning (TLS) work was carried out using two Faro systems: the Focus3D X330 with a ranging capability of 330 m, and the Focus S70 with a ranging capability of 70 m, which ensured the measurement accuracy and point cloud density.

The mobile laser scanning (SLAM) survey was performed using the Stonex X120GO handheld scanner with a ranging capability of approximately 80-100 m, which was employed to supplement areas of buildings or excavations that were difficult to reach with TLS and to provide reference points for global point cloud registration. The following section briefly introduces the methods adopted to

achieve the objectives described above.

Fig. 25 (a)(b) TLS scanning operation (c) SLAM and TLS scanning operation (d) SLAM at checkpoints

3.2.1 Establishment of geospatial control network

The first phase of the survey began with the establishment of an accurate three-dimensional control network, which served as the foundation for all subsequent detailed 3D measurements. Since the survey area included both the interior and exterior of the city walls, using traditional GNSS techniques to establish the control network was considered as the optimal approach. The Old Nisa archaeological site measures approximately 535 × 657 meters (east-west/north-south walls), and survey vertices were primarily selected on the tops of towers surrounding the city, providing reference points for each excavated area as well as for future zones of interest.

Since permanent GNSS station data were unavailable to refine the global coordinates, a local reference frame (relative reference system) was used.

The first measurements were conducted on three GNSS reference points (S1, S25, S200) (Fig. 26), which served as the fixed vertices forming the triangular baseline. Their measurements employed static GNSS techniques with occupations of 2-3 hours, and a differential method was applied to

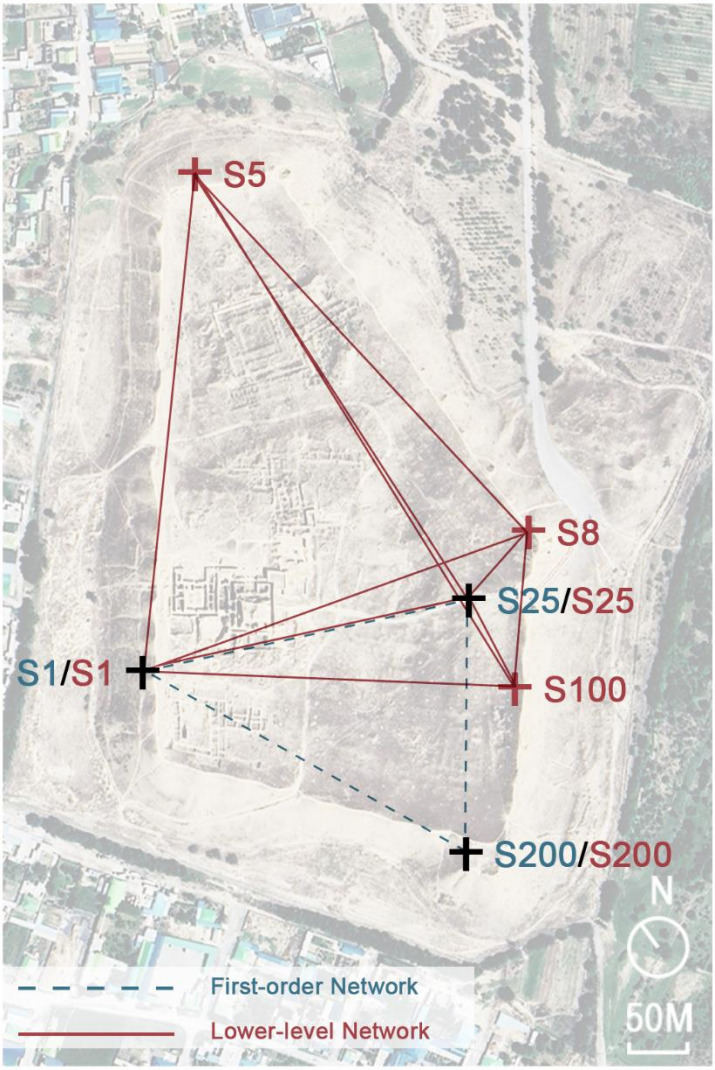

Fig. 26 GNSS primary and secondary network setup

eliminate errors. Vertex coordinates were measured and adjusted using a least-squares adjustment procedure, which estimated the coordinate accuracy and corrected for ephemeris residuals. The establishment of GNSS control network is according to the international UTM N40 WGS 84 reference system, ensuring a practical and necessary universal reference framework for archaeological and environmental investigations.

Subsequently, five vertices (S1, S5, S8, S25, S100) (Fig. 26) placed on pre-existing stable site stakes were measured for the establish of the control frame. Additionally, measurements were taken from two other vertices at the top of the southeastern tower, where exist a stable cemented picket served as secondary control network reference. Besides, wall columns at Russian survey period vertices and metal markers visible from a distance were also measured from each of the other vertices. Since the traditional control network has been measured by using the directions and distances from each vertex to other vertices, as well as the zenith angle, high redundancy are existing (resulting in repeated calculations of 4 directions and 4 distances for each vertex). Subsequently, the data were adjusted using MicroSurvey Starnet v7 software, producing a refined and complete topographic control network. The diagram below illustrates the overall network organization and its extremely high metric quality, with an accuracy that can reach the millimeter level. The local reference frame has now been aligned with the UTM N40 WGS 84 reference system provided by GNSS baseline measurements, allowing conversion between the two systems as required for the survey (Table. 4-6).

Table. 4 Final adjusted coordinates of the complete topographical control network

	X	Y	Z
S100	500.000	500.000	500.000
S1	812.010	500.000	508.750
S8	493.802	366.939	500.669
S25	542.706	426.271	491.592
S5	792.320	78.691	495.347
S200	535.514	641.934	499.712

Table. 5 Error Propagation: Station Coordinate standard Deviations (Meters)

	X	Y	Z
S100	0.000000	0.000000	0.000000
S1	0.002309	0.000002	0.005851
S8	0.002745	0.002037	0.002900
S25	0.002241	0.001950	0.002516
S5	0.005047	0.002851	0.007708

Table. 6 Error Propagation: Station Coordinate standard Deviations (Meters)
NOTE -Adjustment Failed the chi-square Test
Standard Deviations are Scaled by Total Error Factor

	X	Y	Z
S100	0.000000	0.000000	0.000000
S1	0.000000	0.000000	0.000000
S8	0.007912	0.006240	0.013428

The planimetric coordinates (X, Y) will be used for general georeferencing (fixing also the main elevation), while the differences in level (Z) and distances of the vertexes will remain the ones calculated using the traditional survey method (total station) to provide more accurate points heights and orientations for the future detailed topographical operation within the site. The final process will provide the geodic heights using the old Russian cartographic heights (Fig. 27).

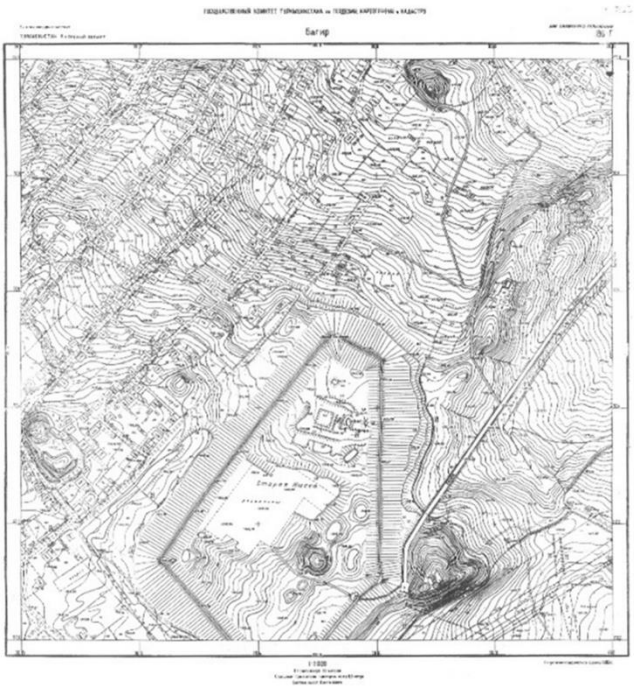

Fig. 27 Survey maps of Russian archaeological period

3.2.2 TLS LiDAR workflow

In this phase, terrestrial laser scanning (TLS) was conducted using two scanners equipped with coaxial cameras (Focus3D X330 and Focus S70 by FARO). They primarily served to construct high-resolution 3D microtopography surfaces and support geospatial analysis, as well as to extract multi-scale representation models suitable for different research objectives and applications.

The main scanning strategy is placing multiple adjacent scan positions along the tops of the city towers, enabling the collection of a series of highly detailed scans. Additionally, a transverse scanning strip was acquired in the east-west direction, corresponding to the main tower entrance path (Fig. 28). This primary scanning chain was executed using the 330-meter range scanner at a 1/4 resolution (with adjacent points spaced 6 mm apart at a 10-meter distance), generating a very extensive point cloud. Scan registration was performed using a set of highly detailed and widely distributed control points, marked with checkerboard targets, whose coordinates were calculated from the new control network. Over 90 control points were measured using polar coordinate methods, and portions of these scanning positions can be observed in the Scene software view of the real-world dataset (Fig. 29).

In addition to surveying the entire site, TLS was also employed to establish complete scanning chains around the main city buildings, capturing the primary facades and providing ground truth matrix reference for other mobile scans. Furthermore, TLS was used to conduct targeted recording of several key structures within the “central building complex” (including the interior of the Round Hall, the forecourt of the Red Building, the interior of the Red Building, the interior of the Round Hall, and the forecourt of the Tower Building), ensuring the acquisition of high-quality point clouds in these complex areas (Fig. 28). In total, 341 scan positions were employed to achieve full coverage of the entire site.

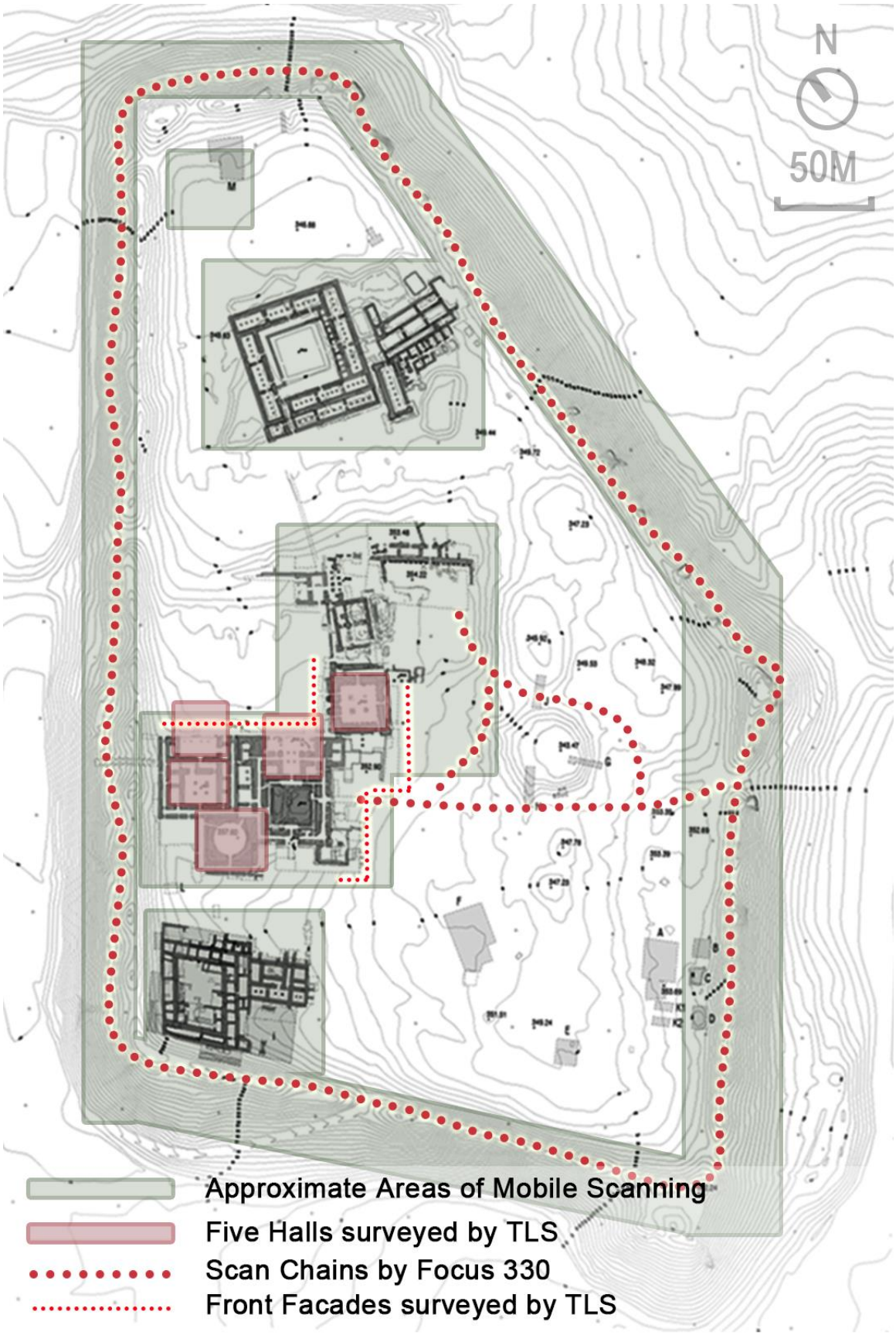

Fig. 28 TLS scan routes/areas, SLAM scan areas

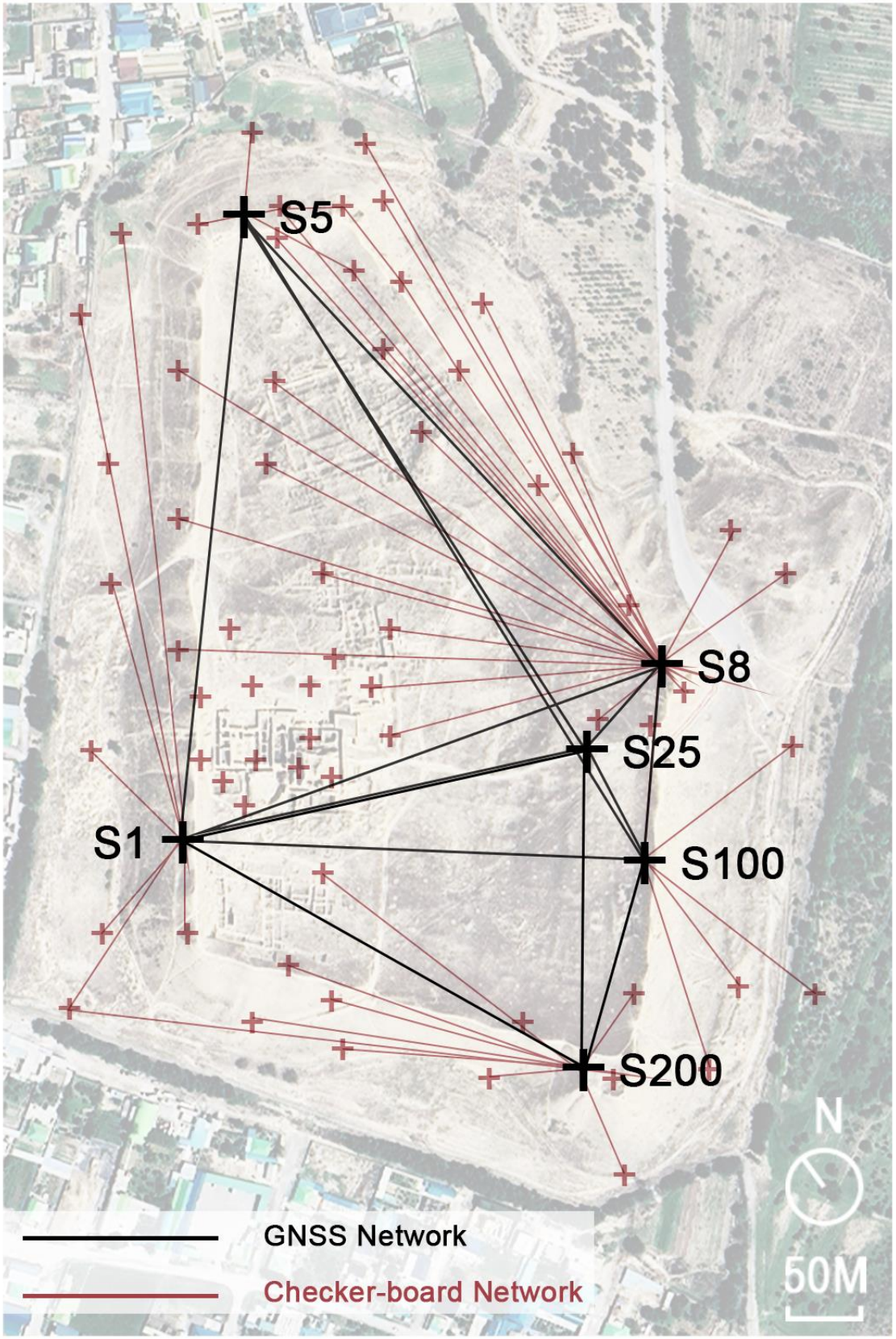

Fig. 29 Control points network

3.2.3 SLAM LiDAR workflow

The mobile scanning using the handheld Stonex X120GO was conducted synchronously with TLS along the main scanning chain, primarily surveying the exterior of the city walls. Two mobile acquisitions were carried out on the western side of the walls, one on the southern side, two on the eastern side, and the final one on the northern side (Fig. 28). These datasets were subsequently integrated in software, in order to form a complete point cloud surrounding the entire site. The scanning trajectory can be seen clearly via timestamps: the mobile route started at the eastern gateway (currently near the parking platform), proceeded in sequence through the south, west, and north sides, and finally returned to the entry platform to complete the trip (Fig. 28). During the mobile survey, the SLAM system was occasionally paused at designated points to perform self-validation.

The greatest value of the SLAM mobile scanner was its ability to perform a new set of mobile scans inside buildings, traversing the main hall, secondary rooms, and corridors, and moving over walls and room coverings, thereby filling many TLS blind spots (Fig. 30). In addition, even though the main scanning chain already provided a very dense point cloud, SLAM was still used to survey areas of archaeological interest within the site: one scan was conducted for the excavation pit in Area I, and two scans were carried out for the northern square hall area and the excavation pit in Area M.

The following table summarizes the responsibilities of TLS and SLAM:

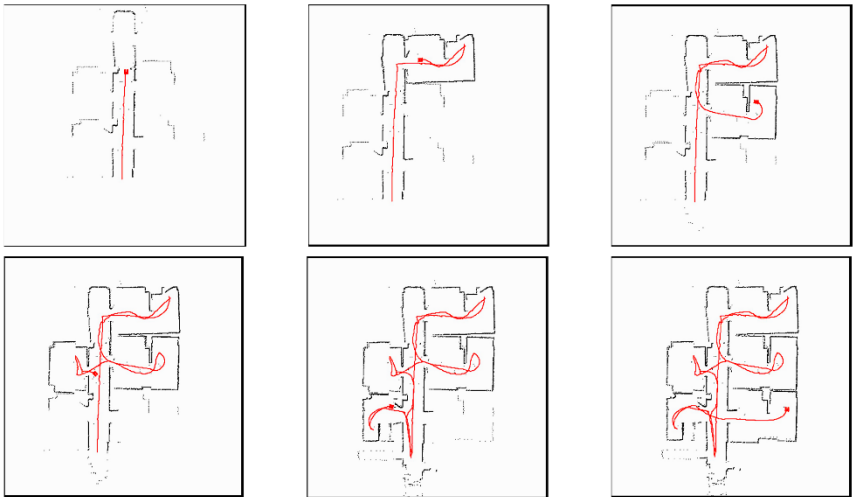

Fig. 30 SLAM scan path, room construction

Table. 7 Classification and functions of primary geomatic tools used in the point cloud acquisition workflow

	Main Tasks	Output
GNSS system	Establish global geospatial reference framework (under UTM N40, WGS84)	Global coordinates of control network of the sites
Total Station	Refine local reference system, improve relative accuracy	High-precision local coordinates
TLS LiDAR	Provide high-accuracy and high-density point cloud	High-resolution point clouds with intensity and RGB, reliable point cloud reference of the archaeological site
SLAM LiDAR	Supplement TLS blind spots	High-quality point clouds in densely built-up areas

Chapter 4: Data Processing & Analysis of Point Cloud

4.1 Data Processing：Integration and Review

4.1.1 TLS data

TLS data processing was performed using a commercial software Scene developed by FARO. The purpose was to initially integrate and register source files from different TLS scan stations, unifying them within a complete, real-world georeferenced coordinate system (UTM N40 WGS 84). The color information captured by the depth cameras was applied to the TLS point clouds for colorization, and the final datasets were exported in the universal point cloud format (.e57) in segments, enabling fitting with a wider range of software environments (Fig. 31).

Fig. 31 Mura 27 slice as example, the scanned point cloud and image are integrated into the scene, and the scanned points within a sub-file are visible

The geometric registration principle in Scene is based on feature recognition, automatically or semi-automatically picking similar natural features (such as corners, edges, and planes) and artificial targets (checkerboard or spherical targets, checkerboard targets were used in this survey) between scan stations, aligning them within the same coordinate system to achieve geometric-constrained

registration and spatial reconstruction of laser point clouds (Rusu, Blodow, & Beetz, 2009) (Rusinkiewicz & Levoy, 2001). Scene provides three kinds of registration modes: automatic registration, manual registration, and interactive registration in the latest version (Fig. 32).

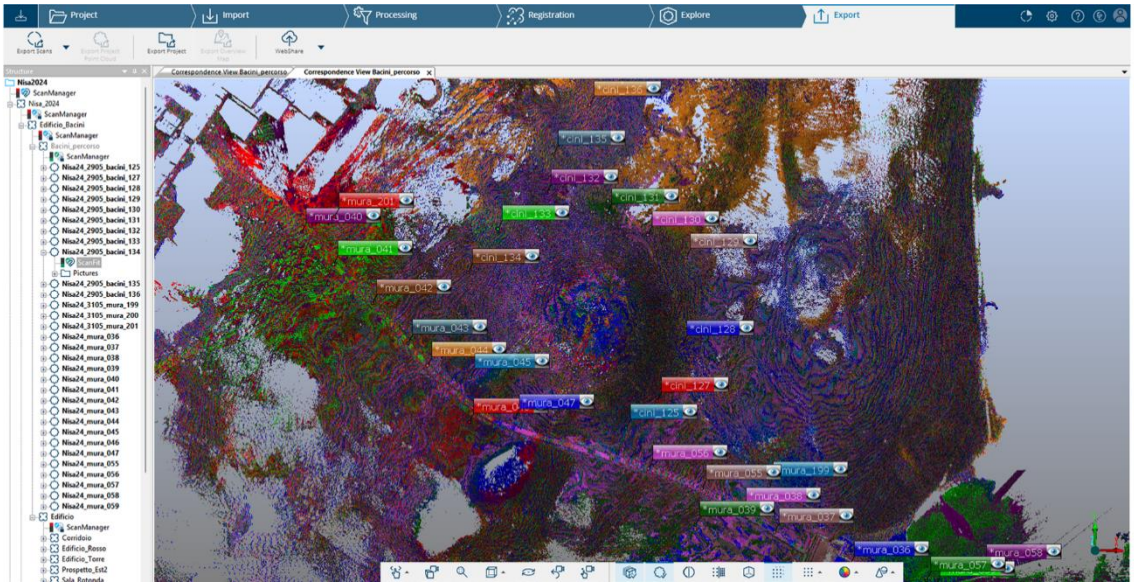

Fig. 32 Aligned point clouds, each label representing a scan fragment

For this project, processing was conducted primarily in automatic registration mode, assisted by manually checked and calibrated. At the end of this step, the result is an aligned geometric model without georeferencing. Since GNSS control points were used on site, Scene subsequently transformed the model into the global georeferenced coordinate system. To reduce workload, large integers in the global coordinates of the points were cut, though the displacement can always be corrected using a transformation matrix (see 4.2.3). Finally, the Mean Scan Point Distance Error can be viewed in Scene's Scan Manager, which at the target scale

Fit	Scan/Cluster	Mean Scan Point Dist. Error [mm]	Mean Target Dist. Error [mm]	Mean Target Ang. Error [°]	Incl. mism. [°]
	Nisa24_2905_bacini_134	6.85	---	---	0.008
	Nisa24_mura_047	6.60	---	---	0.016
	Nisa24_mura_058	6.40	---	---	0.006
	Nisa24_2905_bacini_127	6.31	---	---	0.011
	Nisa24_2905_bacini_125	6.17	---	---	0.014
	Nisa24_mura_039	6.07	---	---	0.007
	Nisa24_mura_044	5.99	---	---	0.008
	Nisa24_mura_036	5.98	---	---	0.006
	Nisa24_2905_bacini_135	5.74	---	---	0.007
	Nisa24_mura_043	5.50	---	---	0.006
	Nisa24_3105_mura_200	5.50	---	---	0.007
	Nisa24_3105_mura_199	5.50	---	---	0.005
	Nisa24_2905_bacini_131	5.49	---	---	0.008

Fig. 33 Point cloud errors after region registration by Edificio Bacini Percorso, listed in descending order, with the largest being 6.85 mm

indicates that the registration quality is acceptable (Fig. 33).

341 TLS scans were performed in total, organized into 24 clusters and 3 blocks, with each cluster containing 10-15 million points, and 42.6255 billion points in total. The shape accuracy ranged from 4-6 mm, with a target accuracy of 5 mm, and the total file size amounted to 322 GB, including 70 GB of camera image files (CRI) (Spanò, 2024). Due to the extremely huge quantity of data, even with professional-grade computer hardware, it remained very difficult to process the entire dataset as a whole. Therefore, a segmented processing strategy was adopted: Point clouds will first be optimized while maintaining its unmerged size, and the subsets will be merged only when necessary, allowing for manageable computation while maintaining processing efficiency.

Fig. 34 Final TLS Point Cloud

4.1.2 SLAM data

Unlike TLS, SLAM scanners integrate the algorithmic system, so no additional registration step is required. During real-time mapping, the point clouds are automatically unified within a local coordinate system, and color information is simultaneously applied via the camera sensor. In short, SLAM effectively integrates the functions of TLS and Scene (excluding georeferencing) during the scanning process. A total of 20 SLAM scans were conducted, and 716 million points with an average accuracy of 6 cm and a total file size of 15 GB (Spanò, 2024). Unfortunately, the SLAM-exported point clouds lost all color information, and significant misalignments occurred at the overlapping sections.

Fig. 35 Final SLAM Point Cloud

4.2 Data Processing: Calibration and Optimization

The following summarizes the main issues identified during data processing:

1) Loss of color information in SLAM point clouds
2) Noise from vegetation and buildings
3) Alignment discrepancies between TLS and SLAM
4) Parameters for 3D mesh reconstruction

To ensure that the point clouds meet the 1:500 scale model accuracy requirement and allow for accurate GIS analysis, the issues identified above must be addressed through pre-processing. The author's work begins primarily from this stage, focusing on point cloud optimization (including organization, denoising, merging, alignment, and validation) as well as subsequent processing tasks (including mesh generation from the point cloud, 3D printing tests, and model planning). In this chapter, open-source software CloudCompare is introduced for optimization work.

4.2.1 Loss of color information in SLAM point clouds

The colorize function in CloudCompare allows a target point cloud to be colored using a reference point cloud with known color information. In this study, TLS-derived color data were applied to black-and-white SLAM point clouds. It is noteworthy that, in practice, due to non-overlapping areas between the two datasets (e.g., regions where TLS did not fully capture points) (Fig. 36, a, b), the colorize algorithm works by capturing the color from nearby points in the source cloud and applying it to corresponding points in the target cloud (CloudCompare, n.d.). Consequently, in areas where no direct correspondence exists, the SLAM point cloud may display mosaic-like color artifacts after processing (Fig. 36, c).

Summary of the solution:

Considering that the final goal of obtaining a fully colored point cloud in this study is to provide high-resolution overhead views for subsequent projection, this issue was addressed by post-processing the mosaic areas in image format (Fig. 36, d).

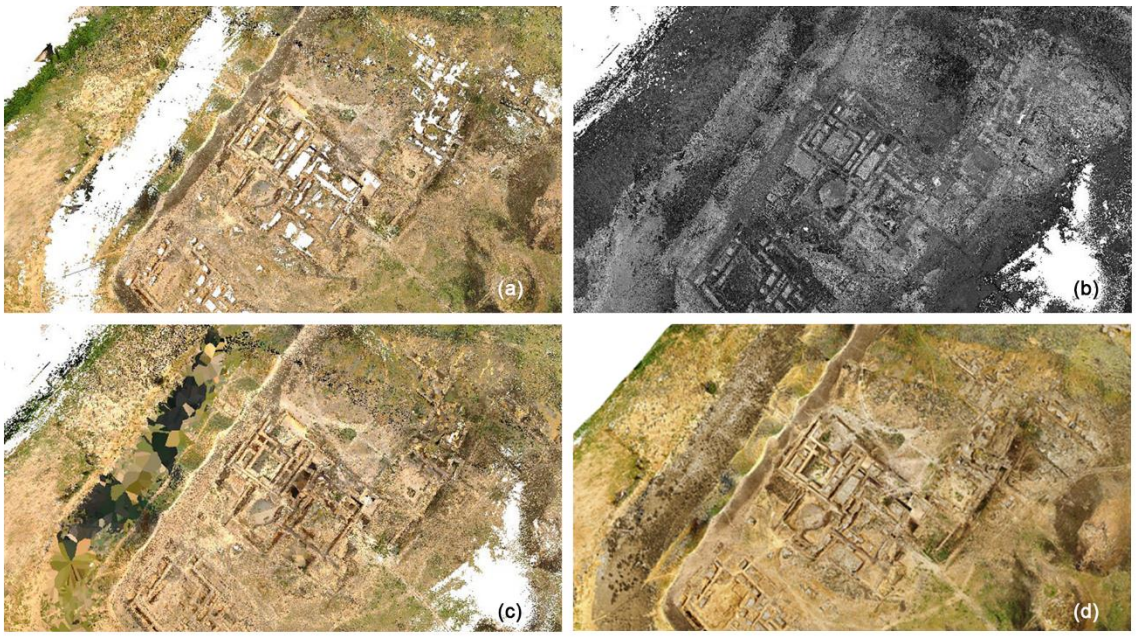

Fig. 36 (a) (b) No-corresponding regions of TLS and SLAM point clouds (c) Stitched region (d) High-resolution RGB point cloud fully restored after image restoration processing

4.2.2 Tests on denoising strategies

The main types of noise present in this survey can be categorized as: isolated floating points, man-made structures such as high-voltage towers and buildings, tall trees, and low shrubs on the ground. The presence of such noise can significantly affect the quality of automatic registration, making it necessary to denoise both TLS and SLAM point clouds separately. Various denoising strategies were attempted in order to better preserve the valid areas of the point clouds.

Before the availability of new TLS data in April 2025, SLAM data cleaning was conducted first. Due to the loss of color information in the SLAM point clouds, it was not possible to use CloudCompare's RGB-based automatic extraction tools. Therefore, alternative methods had to be employed to remove noise caused by vegetation and ground clutter.

The first attempt employed CloudCompare's built-in *Noise Filter* and *SOR (Statistical Outlier Removal) Filter* functions. However, preliminary trials indicated that neither method performed satisfactorily. The Noise Filter algorithm works by fitting a local plane around each point in the point cloud and then removing points that are too far from the fitted plane (CloudCompare Wiki, 2015a). To estimate the underlying (planar) surface, the algorithm searches for neighboring points within a given radius *r* or a fixed number of nearest neighbors *n*, and then calculates the mean distance or standard deviation between the point and its neighbors. If the mean distance is significantly higher than the overall average or the number of neighboring points is too small, the point is considered an outlier and either removed.

However, the *SOR Filter* determines outliers based on the average density between each point and its neighboring points (CloudCompare Wiki, 2015b) For each point, the average distance *d* to its nearest neighbor is calculated, along with the global mean *d'* and standard deviation σ of all points. If the point's neighbor distance significantly exceeds the global mean (beyond the assigned standard deviation threshold by the operator), the point is classified as an outlier and

removed.

While inside the Old Nisa, low shrubs and grass grow densely across almost the entire site, covering some excavation pits and architectural remains (Fig. 37). Their chaotic vector orientations severely interfere with 3D mesh reconstruction.

Thus from the perspective of the point cloud processor, these vegetation points should be considered “noise”, however both the *Noise Filter* and *SOR Filter* algorithms often fail to classify these points as noise because they are too close to valid points, and sometimes even filter out distant terrain points by mistake.

Fig. 37 Vegetation disturbance within the site in scanning environment

Although these algorithms are not very effective at removing vegetation noise, they still successfully remove many isolated outliers, which is means they still need to be applied in the early workflow. Additionally, manual splitting is necessary for cleaning some invalid points, as these groups cannot be removed automatically due to the algorithms’ logic limitations. Consequently, we further explored two denoising strategies as below.

4.2.2.1 Denoising in 3D Reshaper: DTM involved

The first method is based on Leica's 3D Reshaper software, which extracts a Digital Terrain Model (DTM) from the point cloud (Hirt, 2014) and then calculates offsets to retain only points closest to the DTM (Fig. 38).

Fig. 38 Concept of DTM & DSM

The first stage involves in selecting appropriate parameters to optimize DTM extraction. Through testing, setting the maximum terrain slope to its upper limit proved beneficial for extracting steeper surfaces, as the presence of vegetation often causes a sudden increase in local slope relative to the ground (Fig. 39, a). The DTM grid size was set to 50 cm, balancing detail level and processing time. The resulting DTM mesh consisted of 221,250 points and 442,408 triangles (Fig. 39, b, c). However numerous unnatural sharp protrusions were still observed, requiring slight smoothing of the grid to more regularly extract points close to the ground layer and remove noise points far from the scanning center (Lenti, 2025). With the help of this mesh, points can be filtered according to a tolerance, defined as the distance from the DTM surface. To extract a cleaner subset of points, the

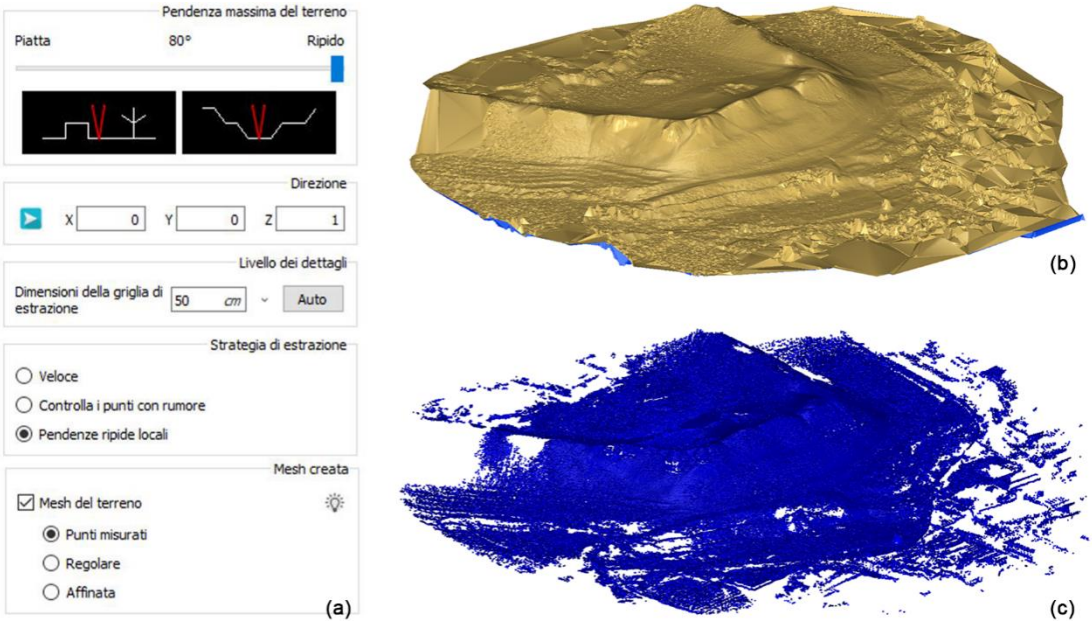

Fig. 39 (a)Terrain slope parameters (b)DTM extracted (c)Cloud extracted according to DSM

maximum distance tolerance was set to 5 cm. This method is highly effective for point clouds collected in areas without buildings or structures, as it can generate a very smooth DTM, thereby isolating the noisiest points in the dataset. However, in areas with buildings, it is not possible to extract vertical surfaces, making this method less suitable for separating points in densely built zones.

In such cases, an alternative approach is to extract a Digital Surface Model (DSM) from the point cloud (Hirt, 2014), using a procedure similar to DTM extraction. The DSM helps to separate points in areas with buildings, as it represents a mesh of the entire point cloud, including elevated points. However, because the mesh is generated from the upper points of the point cloud, which may include vegetation-covered areas, the DSM generally contains more noise (Fig. 40, a).

In summary, a balanced solution is to manually divide the point cloud into two smaller subsets: one containing points inside buildings, and the other containing points outside buildings. The two subsets are then processed separately, using a DSM-based approach for the building interiors and a DTM-based approach for

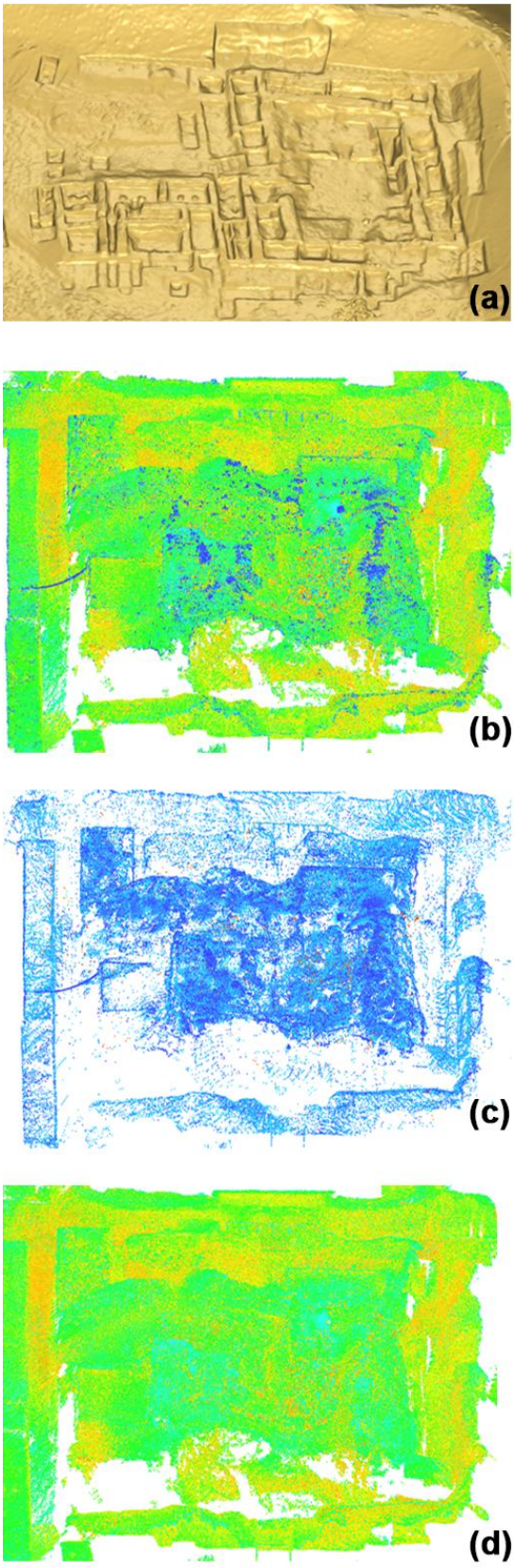

Fig. 40 (a) example of a DSM used for separating the point cloud (b) Point cloud before filtering (c) filtered and eliminated (d) Point cloud after filtering

the exterior points, before merging them back together.

Another primary point cloud denoising method is based on intensity filtering. Since the intensity value represents the strength of the returned laser pulse (which varies depending on the surface material properties of the target, and is typically expressed as an integer between 1 and 256), it can also be used as a filtering criterion for point clouds (Fig. 40, b, c, d). However, the returned intensity is also affected by scan angle, distance, surface composition, and moisture content, which means that filtering based on intensity does not always produce consistent results. For Nisa, intensity-based filtering is effective at removing most vegetation, particularly when they are near buildings. To avoid removing points that are far from the scanning center and have low intensity, the point cloud must be manually segmented prior to filtering. Additionally, some removed points are not actually noise, but were excluded solely due to their low intensity. Therefore, this filtering method is only suitable under specific conditions.

Finally, manual segmentation and cleaning were required for some points that are difficult to remove automatically, such as the stairs and towers at the eastern entrance and nearby modern structures surrounding the site. After denoising, filtering, and merging all point clouds, a refined SLAM point cloud was obtained, which is more suitable for 3D printing and contains approximately half the number of points of the original dataset (Fig. 41).

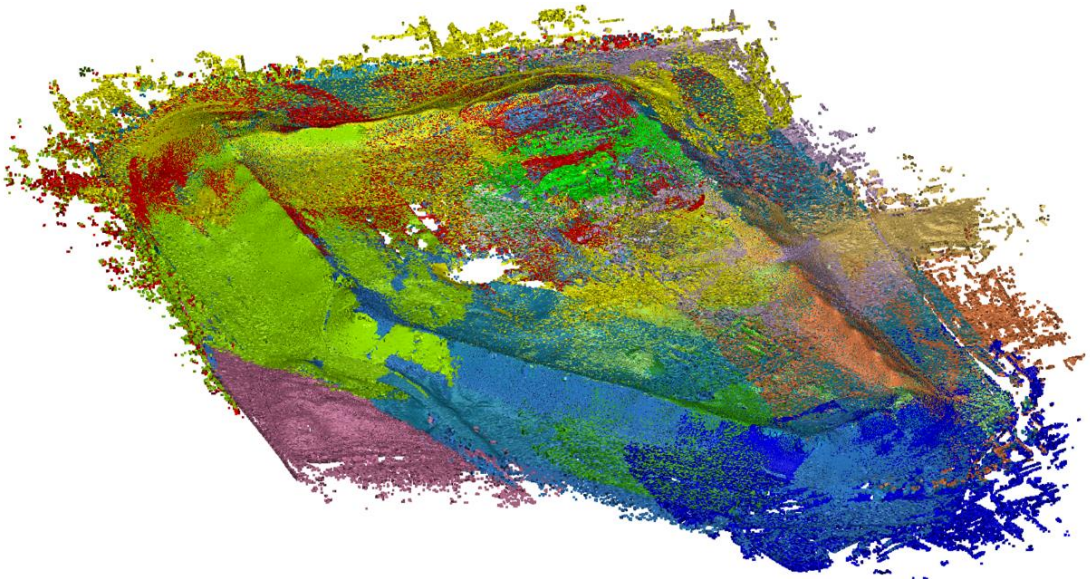

Fig. 41 Final Point cloud filtered

4.2.2.2 Denoising in CloudCompare: CSF involved

The second strategy is based on CloudCompare's *Cloth Simulation Filter (CSF)* plugin, which can automatically separate terrain from non-terrain objects. This plugin was developed by Zhang et al. (Zhang et al., 2016). Its operational logic is similar to the DTM-based approach in 3D Reshaper in some way, also following a workflow of point cloud - simulated terrain extraction - proximity-based point classification. The basic principle of the algorithm is to invert the original point cloud and simulate a virtual cloth falling under gravity above it. During the falling process, the cloth interacts with the inverted point cloud surface, ultimately forming a fitted "ground surface" that approximates the real terrain. By calculating the distance between the original point cloud and the cloth model, the algorithm can automatically distinguish ground points from non-ground points, enabling efficient ground extraction (Fig. 42).

According to this computational logic, the *CSF* method is particularly suitable for the present case, as the generated DTM is not affected by surface noise, ensuring that the DTM remains clean and well-fitted. Points that do not belong to the ground layer are assigned to a separate group, making it easy to check and further segmentation if necessary (Fig. 43).

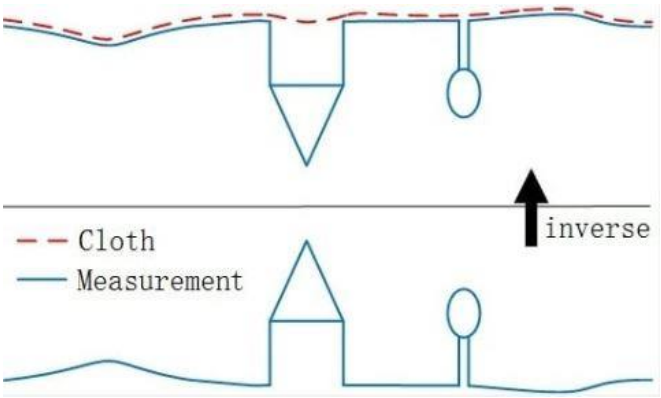

Fig. 42 CSF logic: Inverted point cloud, simulating an inverted cloth under gravity, extracting DTM, obtaining neighboring points to generate a clean DTM point cloud

In general, prior to running the algorithm, it is sufficient to set the terrain parameters, cloth resolution, and the number of iterations to obtain two clearly separated point cloud groups. The workflow is therefore very straightforward and user-friendly.

Some mis-classifications are inevitable, for example, parts of the ground connected to building structures may be classified as non-ground points. However, these areas are generally easily to be distinguished, and can be quickly split and merged using the *segment* or *cross-section* tools.

Even in relatively complex areas, practical tests have shown that repeating the CSF command about three times can ensure an almost perfect extraction of valid ground points (Fig. 43). Although some manual identification is required, its efficiency and accuracy are still much higher than those of the other three processing methods. The denoising of TLS point clouds was entirely carried out using this approach.

Summary of the solution:

For SLAM point clouds, DSM extraction and filtering strategy were performed in 3D Reshaper, while for TLS point clouds the *CSF* in CloudCompare was applied. Manual inspection and cutting were necessary, as automated processes alone could not ensure reasonable noise removal.

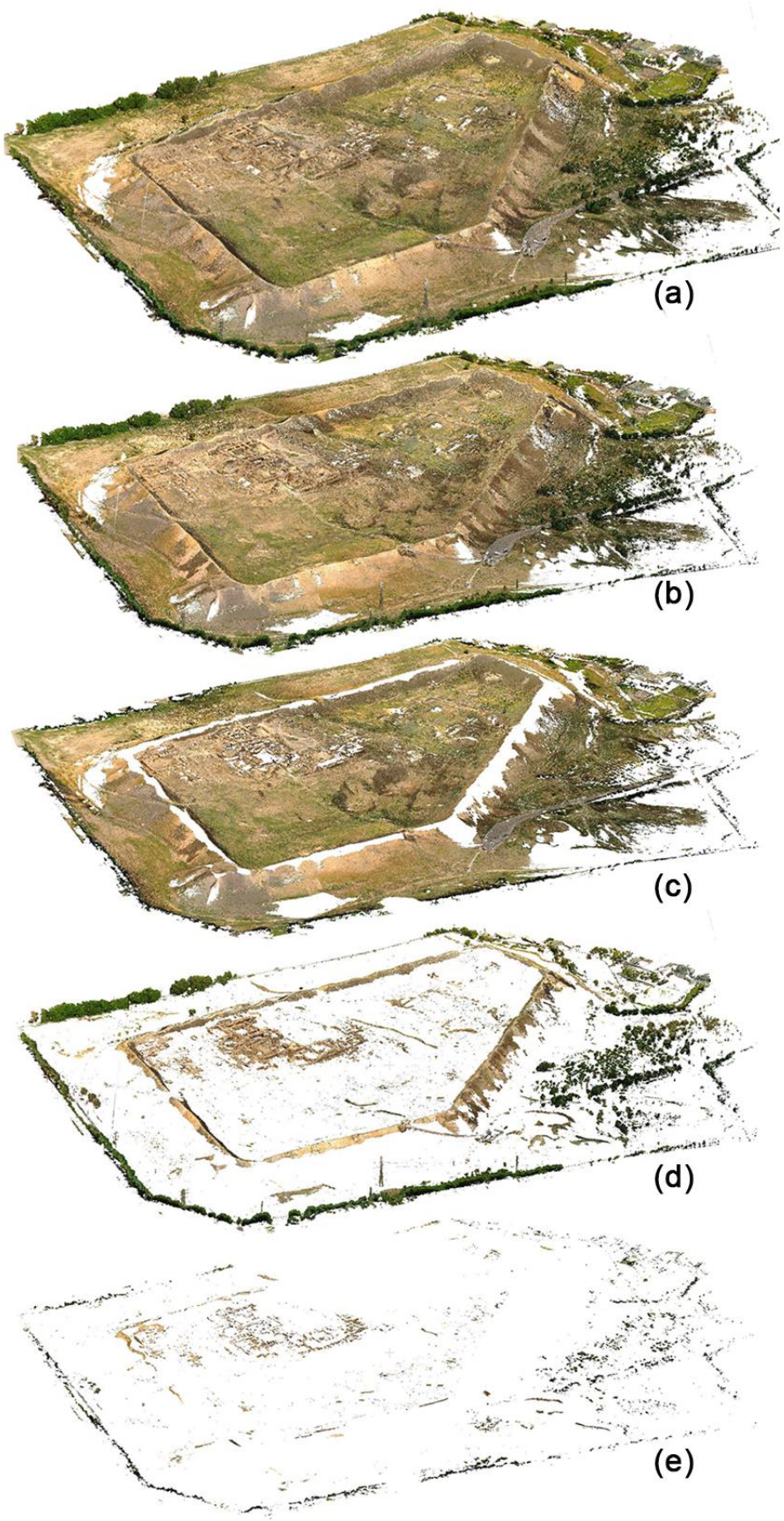

Fig. 43 (a) Original point cloud (b) After SOR noise filtering (c) DTM extracted by single CSF (d) No-ground points extracted by single CSF (e) No-ground points after further filtering

4.2.3 Alignment of TLS and SLAM data

Up to this stage, the denoised and self-integrated TLS point clouds still use a simplified global coordinate system, while the SLAM point clouds remain in their own local coordinate framework. The primary task is to align the two datasets before proceeding with merging and comparison. In this study, the TLS data were taken as the reference, and the SLAM point clouds were rotated to align with the TLS point clouds. A global transformation was applied only when required for geospatial analysis.

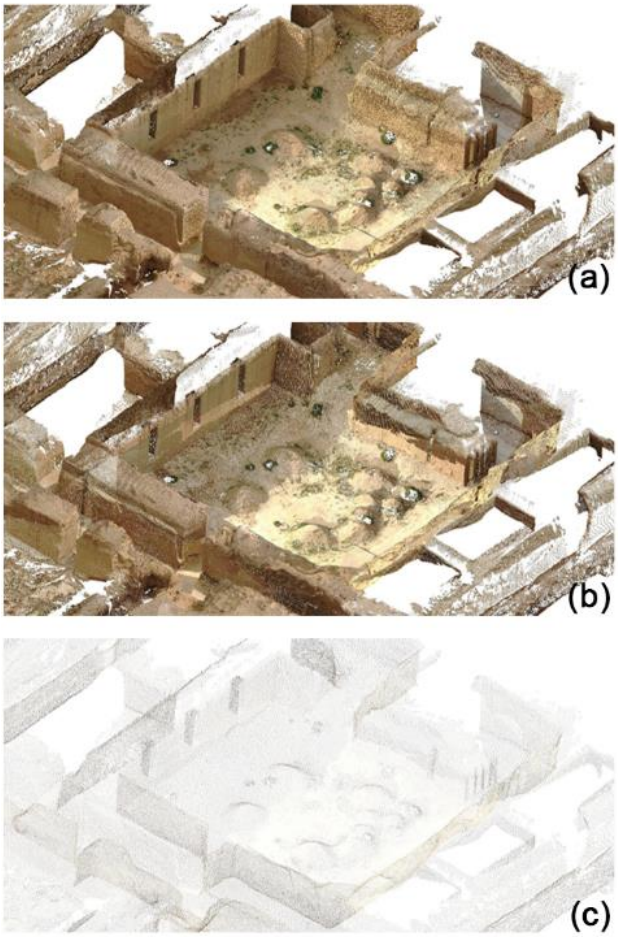

Fig. 44 Point Cloud under density of 1cm(a), 2cm(b), 10cm(c)

To reduce the computing stress, both TLS and SLAM point clouds were re-subsampled after denoising in minimum spacing thresholds of 1 cm, 2 cm, and 10 cm (min space between points) for different using (Fig. 44). The alignment process presented here uses the point clouds sampled at the 2 cm level as an example. The detailed procedure is as follows:

1) The local coordinates and geographic coordinate files of the reference points (S1, S5, S8, S25, S100) were imported into CloudCompare in CSV format, both datasets appeared as point markers in the virtual space. Using the *Registration (Align: Points pairs picking)*, corresponding points between the two datasets were manually paired (e.g., S1_Local matched with S1_Georeference). As a result, the local coordinates were corrected to the georeferenced positions. At this stage, a 16-value matrix could be obtained, representing the transforming parameters between the two coordinate systems (Fig. 45).

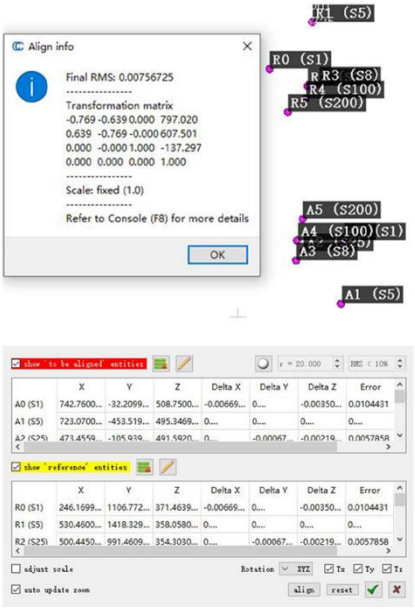

Fig. 45 Corresponding reference point and transformation matrix

2) The *Apply Transformation* was then applied to the SLAM point cloud, using the previously obtained matrix as the operation parameter. As a result, the SLAM point cloud was roughly aligned with the TLS point cloud, after which *Iterative Closest Point (ICP)* automatic registration was performed. The logic of *ICP* lies in iteratively identifying the closest point correspondences between two clouds and computing the rigid transformation (rotation and translation matrices) that minimizes the distance between the matched points. The source point cloud is continuously updated during the iterations, gradually approaching the target point cloud. The iterative process terminates once the error converges or the predefined iteration limit is reached, thereby achieving precise spatial alignment between the two clouds. In fact, the Scene automatic registration mode mentioned earlier, as well as the real-time generation of SLAM point clouds, both follow this algorithm.

3) At this stage, the two clouds appeared to be nearly perfectly aligned at a visual inspection level. To evaluate the alignment accuracy, the *Cloud-to-Cloud (C2C)*

distance function was used to calculate the point-to-point distances between the TLS (target point cloud) and the SLAM point cloud. The color bar tool was then applied to filter and visualize the *C2C* parameters. In the *Global Display* mode, areas with larger alignment errors appeared in red, while regions in green indicated optimal alignment performance (Fig. 46).

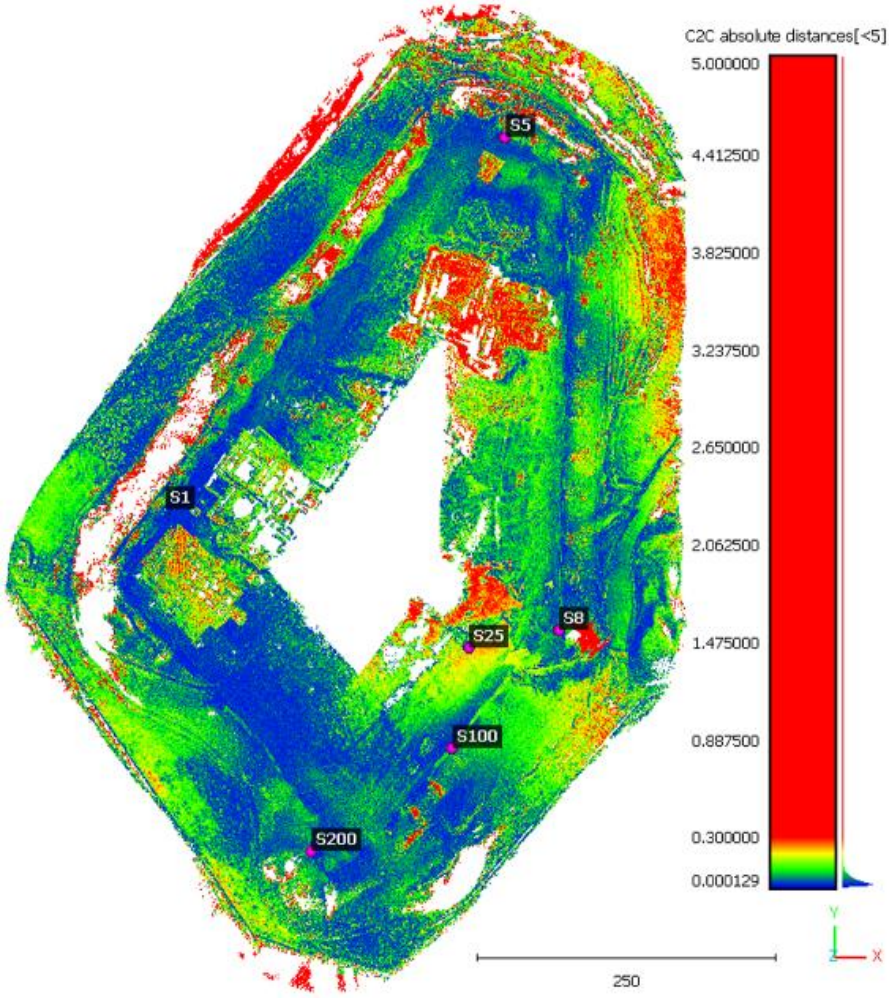

Fig. 46 C2C computation, 229_Giro Completo as example

Areas shown in deep red indicate that a large number of points from either the target or the source cloud are missing corresponding matches in that region. This does not represent an alignment error, but rather reflects missing data caused by instrument characteristics and scanning limitations. Therefore, before performing Gaussian distribution analysis, it is necessary to set a preliminary threshold and use the *Filter by value* function to remove extreme maximum and minimum values, only then can the resulting data be considered meaningful (Fig. 47).

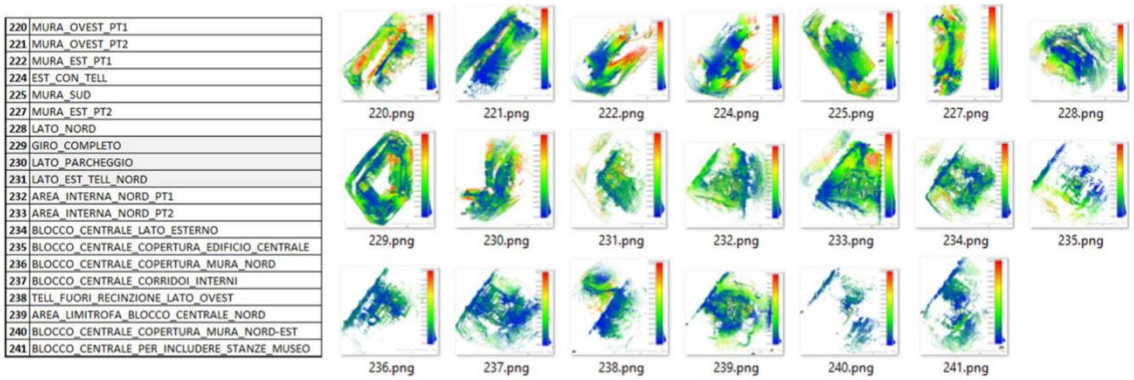

Fig. 47 C2C computation on 20 subsets, in order to exclude outliers, detail see in appendix

Based on the requirements of 3D printing, a criterion of Mean = 0.1 m / Standard Deviation = 0.1 m was adopted. Under the scale of 1:500, this corresponds to an error of approximately 0.2 mm, which is equal to the preset minimum 3D printing layer thickness (0.2 mm) in this experiment. Therefore, point cloud errors below this threshold can be considered satisfied. From this step, histogram of *C2C absolute distances* (in meters) along with the *Gaussian mean* and *standard deviation* are available, allowing verification of whether the results fall within an acceptable error range under the 1:500 scale condition.

A total of 20 SLAM scan groups were compared with the integrated TLS point cloud within the same spatial reference (Fig. 47) (Appendix). The experiment shows that the correspondence between the two datasets varied across different areas of the site. More than 2/3 of the scan groups exhibited both *Mean* and *Standard Deviation* values below the 0.1 m threshold, which can be considered satisfactory in this scale. However, six scan groups showed values close to or exceeding the 0.1 m level (Cloud 220, 224, 227, 230, 233, 235).

After excluding cases where data existed unequal between scanning areas (for example, in group 220, where the TLS dataset contained blank zones on the western side), the most serious alignment issue was found in group 230, corresponding to the registration of the eastern parking entrance. Cross-sectional views shows that the maximum drift distance between the two datasets reached nearly 17 m, while the smaller deviations still exceeded one meter (Fig. 48). It is

speculated that this problem was caused by significant misalignment resulting from repeated SLAM scans in this area. The scanning path for this dataset started from the eastern entrance at the hilltop, proceeded downhill, followed a circular route of up and down around the isolated hill to the east, and then returned uphill to the same eastern entrance. The extended scanning duration, large range of motion, and unstable walking all likely affected the real-time computation of spatial positioning, resulting in the most severe drift observed throughout the entire scanning process.

After three iterations of ICP registration, the drift error in the area was ultimately reduced to approximately 0.7 m, which falls within the acceptable range for this experiment (Fig. 48). The parameters used for the three ICP runs were as follows: overlap ratios of 16%, 20%, and 24%, with random sampling limits (RSL) of 500,000, 700,000, and 1,000,000 points. The *root mean square* (*RMS*) errors for the three registrations were 0.303561 m (based on 500,000 points), 0.176536 m (based on 700,000 points), and 0.168068 m (based on 1,000,000 points).

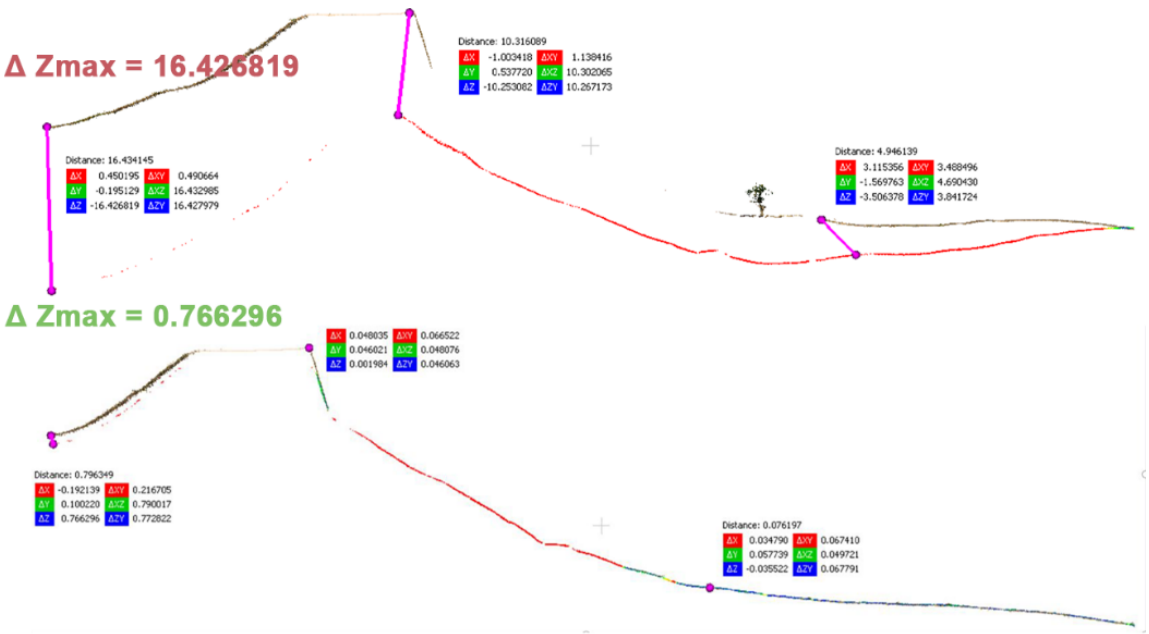

Fig. 48 Comparison of registration differences before and after ICP registration, measured from cross-section

Summary of the solution:

Areas requiring higher precision such as densely built zones, were subjected to registration and merging. For point clouds exceeding the acceptable error threshold, additional ICP registration was performed, followed by another round of error verification. Depending on the results, multiple ICP iterations could be applied, or the process could return to the Noise Filter stage for repetition. In other cases, the dataset with better performance between the two-point clouds was selected for slicing, in order to reduce computing stress. All subsets exceeding the error standard were performed the operation, to ensure that the error was kept within an acceptable range (0.1M). Subsequently, all processed TLS-clouds were merged with the SLAM-clouds, to obtain the Final TLS-clouds and the Final SLAM-clouds. The C2C command was then used on both Final-clouds, to verify the adjusted error distance (Fig. 49).

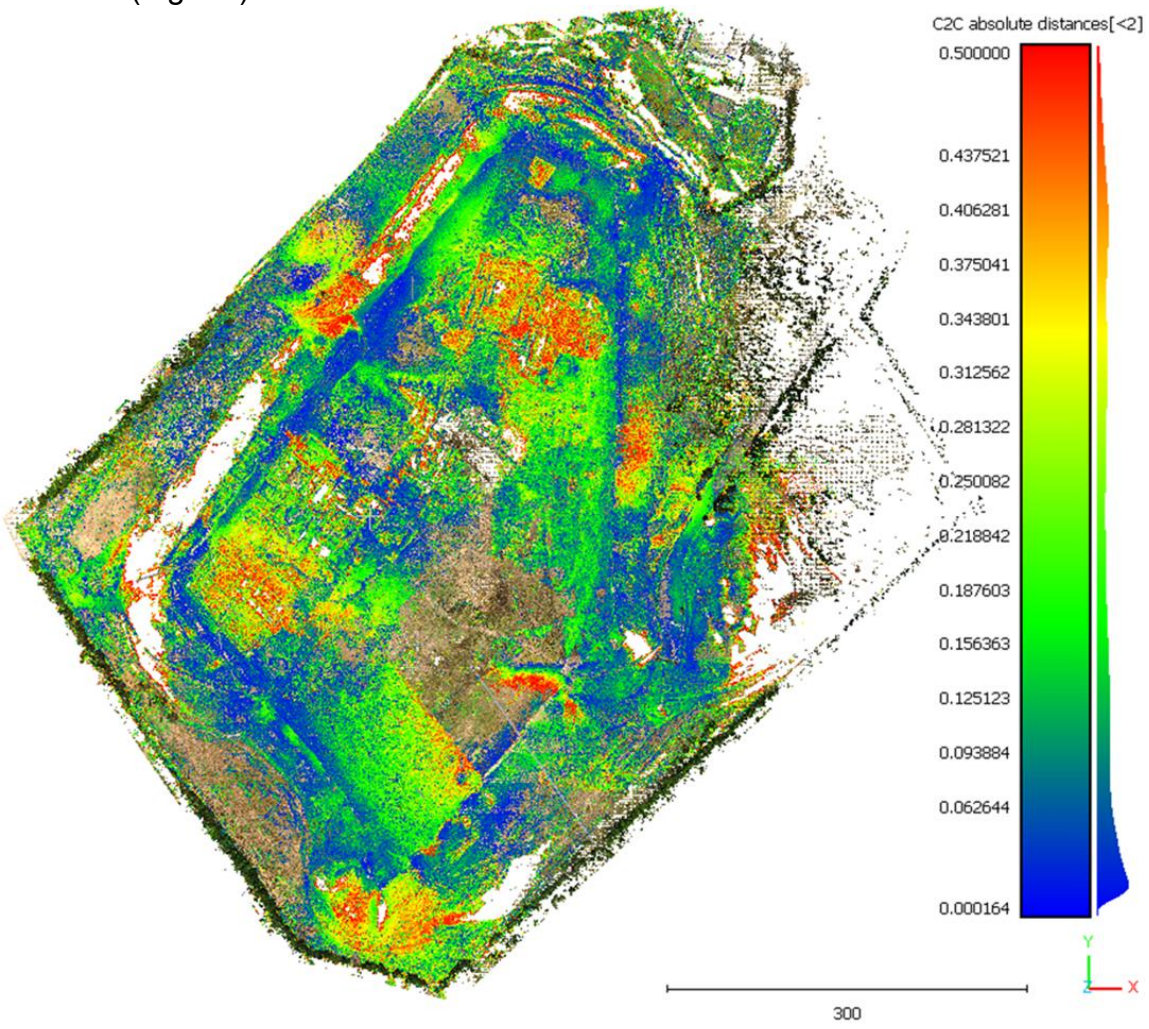

Fig. 49 Comparison of two overlaid point clouds with C2C verification

4.2.4 Parameters for 3D mesh reconstruction

The conversion from point clouds to mesh slices is a key step in preparing data for 3D printing. Due to the large size of the point clouds, it is necessary to perform re-subsample on the cleaned and integrated dataset (TLS + SLAM) before mesh reconstruction. In this case, a 10 cm point spacing level was used as the standard, which corresponds to a printing precision of 0.2 mm at a 1:500 scale. This exactly matches the minimum layer thickness chosen for 3D printing in this experiment, making it sufficient for the task. Even so, during mesh reconstruction, setting an octree depth higher than 13 levels or a resolution value too low (typically below 0.1) can still easily cause the software to freeze.

In this study, the mesh reconstruction task was performed by the mesh reconstruction plugin in CloudCompare, which is based on the Poisson reconstruction algorithm proposed by Kazhdan et al. (Kazhdan, Bolitho, & Hoppe, 2006), with principle treats a point cloud with normals as a sampling of the gradient of an implicit function (therefore it is necessary to execute the *Compute Normals* function before running *Poisson Surface Reconstruction* command), then applied to the point cloud. The algorithm then solves the corresponding Poisson equation to recover the overall surface and generates a continuous, closed triangular mesh by extracting surface (Fig. 50). Based on this conversion logic, the method is advantageous for producing globally consistent and smooth meshes; however, it is sensitive to the orientation of normals and noise. Consequently, in this case, it is essential to ensure proper solving of noise and normals before performing Poisson reconstruction.

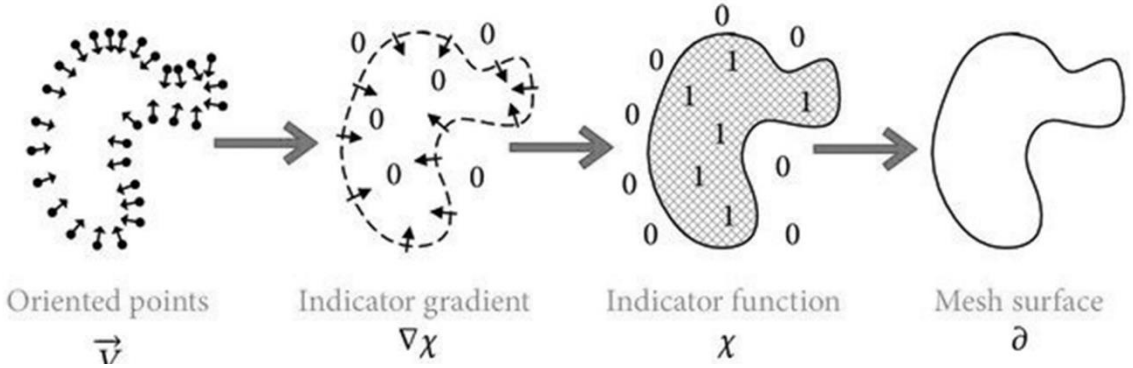

Fig. 50 Poisson surface reconstruction principle

Another relevant concept is the Octree (Elseberg, Borrmann, & Nüchter, 2013) (Fig. 51), which essentially subdivides a 3D space cube into eight sub-cubes, enabling hierarchical management of point cloud data. The node structure records the spatial extent and the distribution of points, which can be used for fast neighborhood searches and spatial indexing, thereby greatly improving computational efficiency. In this study, the *Octree level* settings were critical for both the *Compute Normals* and *Poisson Surface Reconstruction* steps, ensuring that the processing matched the workstation's performance while producing high-quality mesh models.

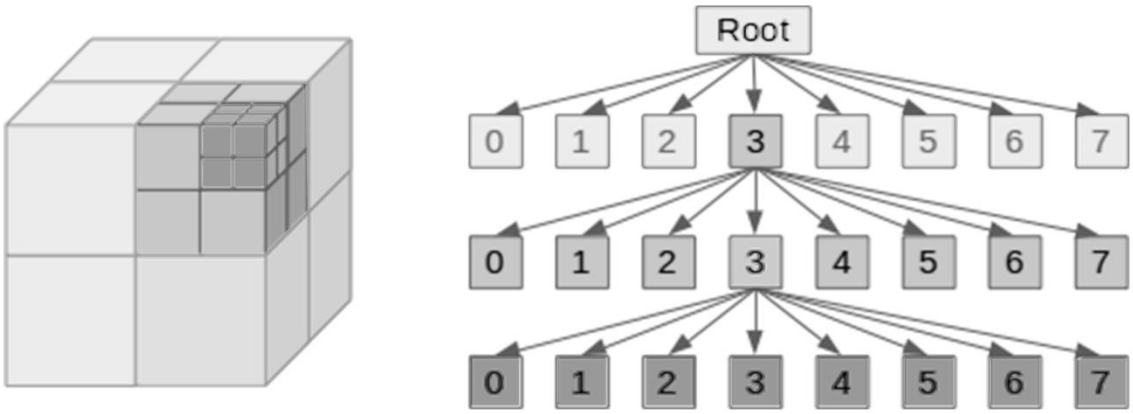

Fig. 51 Octree level concept

In practice, the quality of mesh reconstruction is primarily influenced by three factors:

1) The effectiveness of the *Noise Filter*, which determines whether the computation of normals produces inconsistent orientations.
2) The *Octree level* used in *Compute Normals*, which dictates the spatial scale and smoothing of normal estimation, thereby affecting the stability of the mesh.
3) The *Octree level* or *Resolution* value used in *Poisson Surface Reconstruction*, which ultimately determines the spatial resolution and detail density of the reconstructed mesh.

To maximize the preservation of details, a series of parameter adjustments and trials were conducted. It was ultimately found that, regardless of the control parameter settings, *Poisson Surface Reconstruction* in CloudCompare could not effectively convert the point cloud into a high-quality mesh. Too low parameter

values resulted in loss of detail, while excessively high values produced distorted meshes due to inconsistent normals, typically manifesting as swelling, adhesion to mesh surfaces, or isolated mesh fragments (Fig. 52). However, since this study requires assembling the final model from smaller tiles of a certain size (in size 100m x 100m, to be detailed in Chapter 5), it was decided to break the point cloud into modules slightly larger than the printing size (approximately 150 m × 150 m at full scale) before performing *Poisson Surface Reconstruction*.

In practice, reducing the area processed in a single operation contributes a lot for identifying suitable parameters (Fig. 52). In this case, the normal computation step generally employed *Local Surface Model* as *Plane*, with the *Octree level* typically set to 1.5 or 2. During the *Poisson Surface Reconstruction* step, mesh quality can be controlled either by *Octree level* or by *Resolution*. When using *Octree* as the controlling parameter, its level is usually set between 10 and 12. When the processing area is smaller, a higher *Octree level* can be applied. However, if the area becomes too small, swelling artifacts may occur. On the other hand, when using *Resolution* as the controlling parameter, the level is generally set between 0.15 and 0.2. Smaller *Resolution* values can indeed produce finer details, but they often result in an excessive number of mesh faces, which imposes a significant burden on subsequent mesh processing. It should also be noted that when generating the model, a rich offset along the edges must be retained to cover the overlapping regions with adjacent tiles, preventing misalignment during module assembly. It can be observed that the *Octree level* directly controls the mesh fineness, while the computational precision of normal tends to affect the correctness of detail generation. Higher density point clouds can provide more detail, but for point clouds with insufficient density, there is an upper limit to the parameter increases of Normal and octree, exceeding this limit can easily lead to incorrect generation. Therefore, appropriate reconstruction parameters should be adopted for clouds of corresponding densities. In the last, also other software options for converting point clouds to meshes, such as 3D Reshaper and Meshlab, and it would be interesting to evaluate their performance under these conditions.

Summary of the solution:

The point cloud is divided into regions, multiple reconstructions are performed to obtain complete meshes, which are then used for subsequent correction, merging, and design in 3D modeling software.

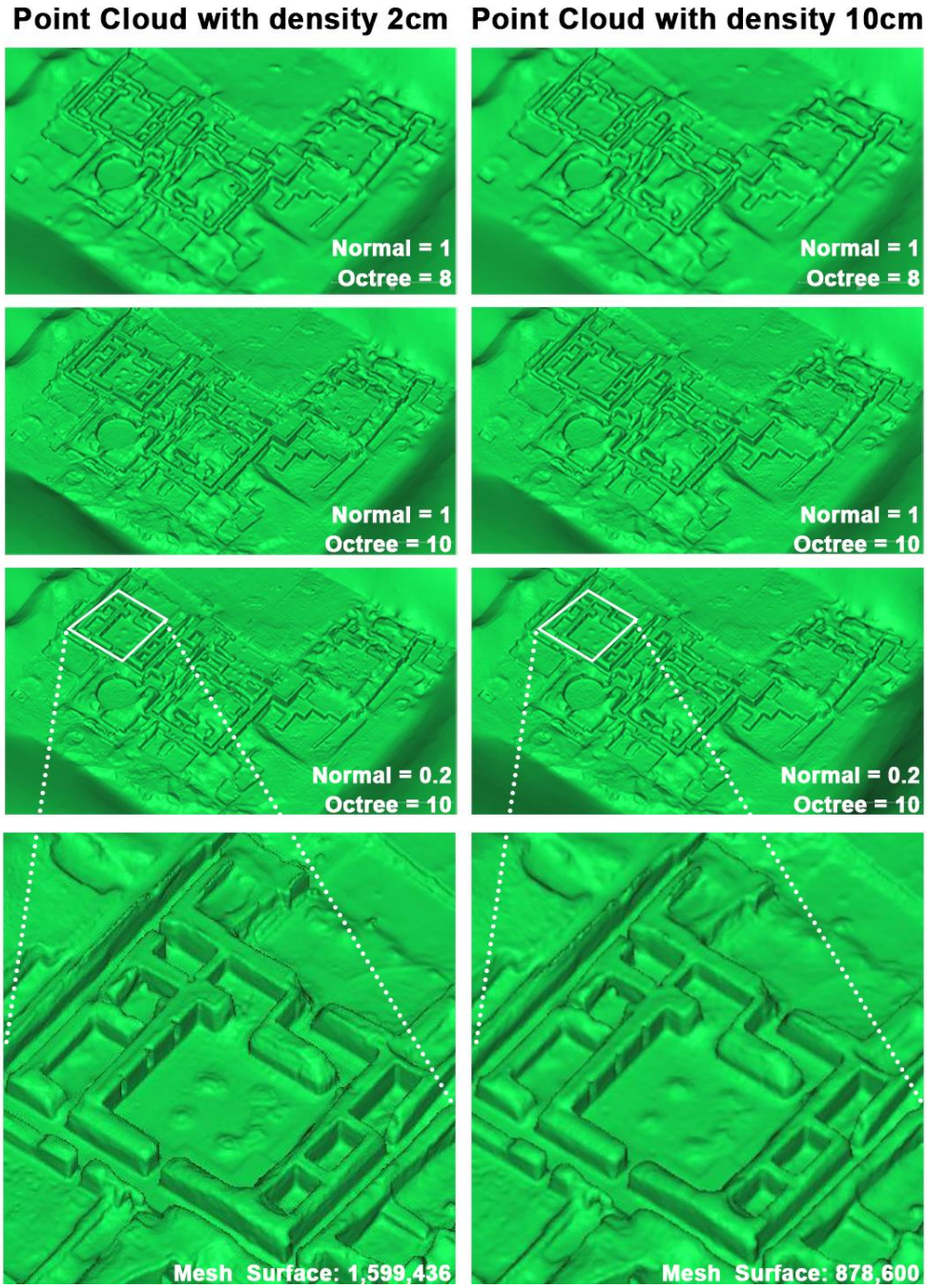

Fig. 52 Mesh reconstruction effect tested by controlling variables: Clouds at a density of 2cm (left) and 10cm (right) were used, with a Normal level of 1 or 2 and an Octree level of 8 or 10

4.3 Further Exploration of the Clouds

4.3.1 Model under different Level of Detail (LOD)

In addition to the existing workflow, further tests were conducted on the mesh reconstruction process, in order to evaluate the influence of point density and reconstruction parameters on the final level of detail of the mesh.

The results indicate that, under the same reconstruction parameters, increasing the point cloud density leads to an obvious improvement in mesh detail performance (Fig. 53). Although this difference is imperceptible at the 1:500 printing scale, using point cloud with higher density combined with higher mesh reconstruction parameters could theoretically support the fabrication of more precision models, such as architectural detail models under 1:100 or 1:50 scale.

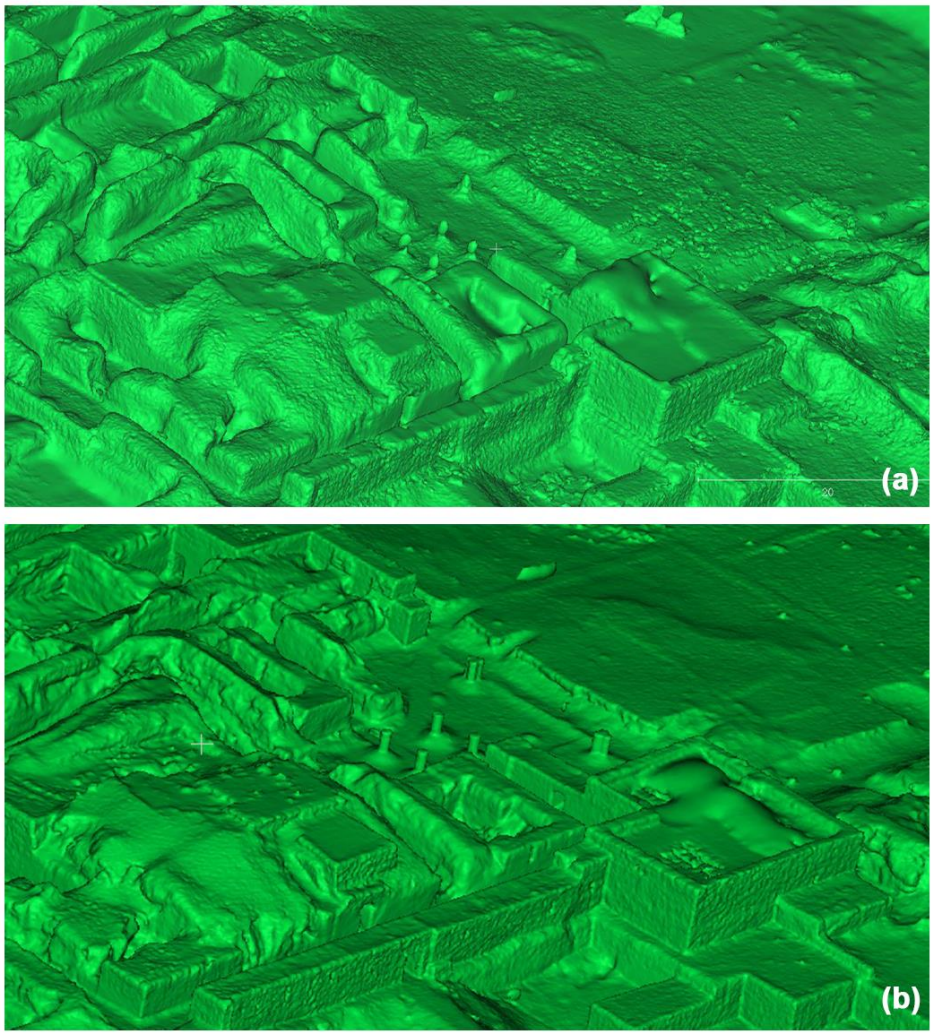

Fig. 53 Normal level = 0.2, (a) 10 cm density point cloud octree level = 11 (b) 2 cm density point cloud octree level = 11

4.3.2 Geographic feature analysis

Beyond serving for digital modeling purposes, the point clouds are also crucial for terrain and spatial analysis. Since video mapping requires an accurate correspondence between the projected imagery and the physical surfaces, precise georeferencing becomes essential in this survey, and the analysis results are further served as projected material for subsequent multimedia work. The analysis step is mainly carried out using the open-source software Quantum Geographic Information System (now renamed QGIS).

QGIS is widely used for geospatial data editing, spatial visualization, cartographic production, and a wide range of spatial analysis tasks (QGIS Association, 2025). Its rich plugin system is maintained and continuously updated by developers around the world, covers functional modules such as terrain analysis, remote-sensing image processing, network analysis, 3D visualization, spatiotemporal simulation and so on, and it also supports adherence to real-world coordinate reference systems (global reference systems). In addition, QGIS offers strong compatibility with data formats, allowing direct reading of many common vector formats (e.g., Shapefile, GeoJSON, DXF), raster formats (e.g., GeoTIFF, ASC), numerical formats (CSV), and point-cloud-derived products (e.g., DEM or DSM). According to the needs of this case, QGIS provides a simple and efficient workflow. The main objectives of this stage are to obtain hill-shade renderings of the target area, extract contour lines, conduct elevation analysis, calculate slope and aspect, acquire satellite image, and generate sunlight analysis. The processed point cloud is rendered into a georeferenced Digital Elevation Model (DEM) (NASA, n.d.) in CloudCompare and then exported in a rendered raster format to QGIS. It is important to note that the integer values in the original point-cloud coordinates were removed during earlier processing, therefore a global shift must be applied to restore the coordinates when exporting the DEM. Additionally, the spatial reference system in QGIS must be set in advance to the local Turkmenistan time-zone coordinate system (UTM Zone 40N, WGS 84), otherwise the DEM will appear

spatially displaced in QGIS. The main analytical tasks are as follows:

1) A black-and-white hill-shade map in 3D effect can be produced by adjusting the angle and azimuth of the light source. The purpose of this step is to use the hill-shade map for projection, enhancing the sense of depth, and it can also serve as a basemap of other analyses, enriching the visual perception and enhancing the effectiveness of the projection (Fig. 54).

Fig. 54 Mountain Shadow

2) The DEM is rendered in QGIS by elevation-based color classification, and contour lines are extracted by defining different values of interval parameters. This step aims to visualize elevation data so that readers can easily and quickly identify topographic variations. The resulting images may be further artistically processed as needed (e.g., changing colors or cropping) to align with the overall visual style of the projection narrative (Fig. 55-56).

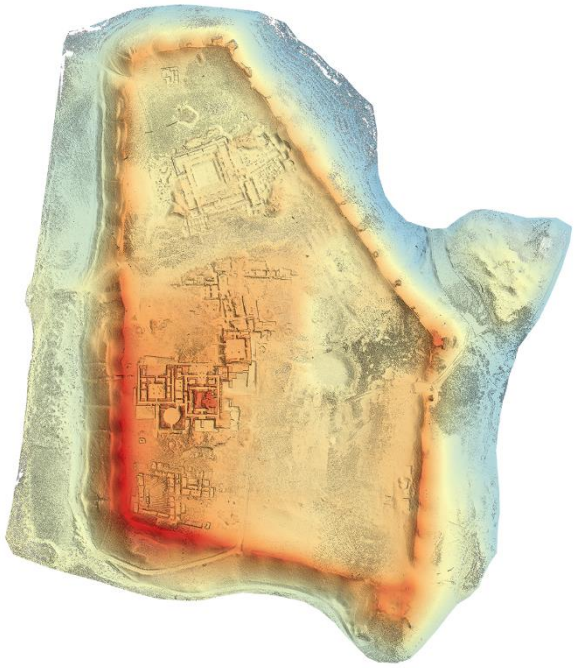

Fig. 55 Altitude: 332m (Blue) - 372m (Red)

3) The slope analysis reveals variations in terrain steepness, which rapidly defined the functional zones within the archaeological site, and enhanced the readability of ancient urban layout and spatial organization. In addition, since slope conditions are closely related to ancient settlement-site selection strategies (e.g. built-up areas and main roads were typically located on relatively flat terrain, while the traces of reservoirs and the direction of drainage ditches can be reflected by the changes happened in topography.), slope analysis has archaeological value as well (Fig. 57).

Fig. 56 Contour Lines distribution

4) Aspect analysis also helps to explain the layout logic of buildings and streets in the ruins, and even to infer the ancient vegetation patterns, thereby the audience's understanding of the environmental choices and living conditions of the ancient city can be enhanced (Fig. 58).

Fig. 57 Slope: 0 (Grey) - 60° (Orange)

5) For the satellite imagery, Google satellite image is loaded through the QGIS basemap plugin and exported by the same viewport as the DEM, rather than obtaining maps directly from Google Earth. This ensures precise alignment between the satellite imagery, the model, and other analytical outputs at the same scale (Fig. 59).

6) In addition, a sunlight simulation was conducted in SketchUp, and the realistic dynamic lighting animation was produced under the local UTM time and the equinox period. Due to hardware and software limitations, high quality video suitable for video mapping could not be exported from SketchUp. Therefore, the final decision was to perform sunlight simulation directly on the model in the animation software Blender, enabling higher-quality dynamic lighting effect (Fig. 61).

Fig. 58 Aspect: North (Red) – East (Orange) – South (Green)- West (Blue)

Fig. 59 Satellite imagery of the site

Fig. 60 Point Cloud (TLS+SLAM)

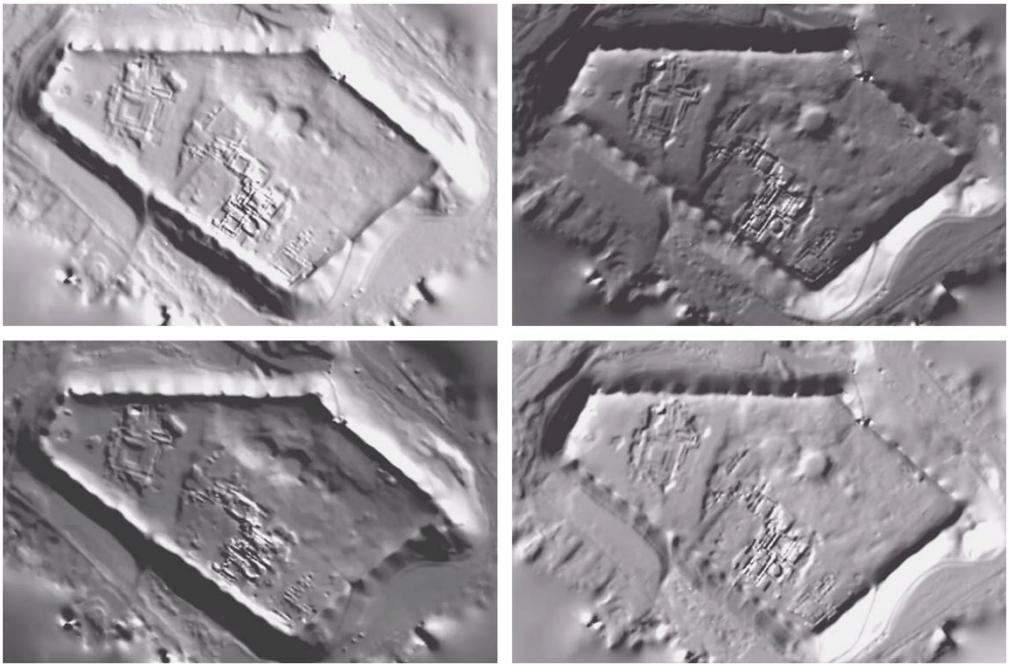

Fig. 61 Simulation of time changes within a day

Chapter 5: 3D Printing Production Process

5.1 Theoretical Background of 3D Printing

Three-dimensional printing (3D Printing), also known as Additive Manufacturing (AM), is a manufacturing technology based on geometric models that creates physical objects by stacking material layer by layer, generating a solid start from cross-sections (Shahrubudin, Lee, & Ramlan, 2019).

Unlike traditional subtractive methods such as cutting or milling, 3D printing does not require molds or shaping tools. Instead, it relies on computer-aided design (CAD) to prebuild the three-dimensional parameters of the target object (in other words, the creation of a digital model), and then controls the printer to determine the material deposition process, achieving direct construction from virtual to physical (Fig. 62).

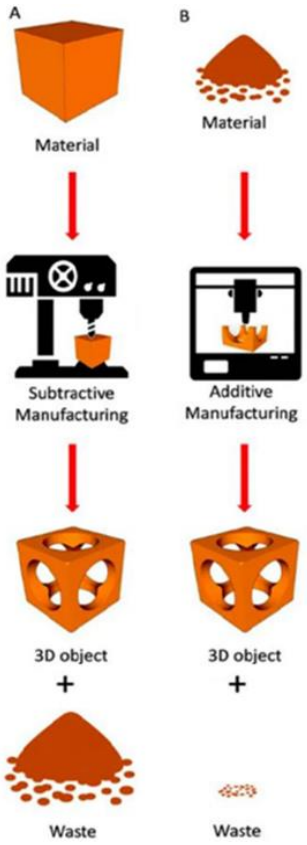

Fig. 62 Additive Manufacturing Logic

With the development of digital manufacturing technologies, 3D printing has been widely applied in various fields such as mechanical manufacturing, medical devices, educational tools, and artistic creation (Raise3D, 2024). With its increasing popularity in recent years, it is moving toward a broader market. In the field of heritage preservation, its ability to rapidly convert digitally captured artifacts or scenes into realistic models is widely valued, providing new media for research, exhibition and education, enabling the transformation from digital heritage to physical reproduction.

According to ISO/ASTM 52900:2021 Standard (ISO & ASTM International, 2021), additive manufacturing (AM) technologies are classified into seven main process categories: Binder Jetting (BJT), Directed Energy Deposition (DED), Material Extrusion (MEX), Material Jetting (MJT), Powder Bed Fusion (PBF), Sheet Lamination (SHL), and Vat Photopolymerization (VPP). Each of these processes

represents a unique forming mechanism and material system, designed to meet specific application requirements. Therefore, the choice of a suitable printing method should depend on the actual needs of the project. Considering the actual situation and budget of the project, Fused Deposition Modeling (FDM, belonging to the MEX category) and Vat Photopolymerization (VPP) were selected in this survey for comparative testing, thus these two printing methods are the focus of discussion.

5.1.1 Fused deposition modeling (FDM)

Fused Deposition Modeling (FDM) is one of the most widely used 3D printing technologies today. The principle of this process is to heat a thermoplastic material to a molten state and extrude it layer by layer through a controlled nozzle along a predetermined path. Each deposited layer rapidly cools and solidifies, and bonding firmly with the layer below. After multiple layers are stacked, a complete three-dimensional model is constructed (Kristiawan & et al., 2021).

An FDM printer typically consists of a material feed system, printing nozzle (hot end), print bed, a control/display system, and a power supply system (Fig. 63). The printing material is usually stored in the form of filament spools, which are fed through the delivery system into a heated nozzle and then melted and extruded.

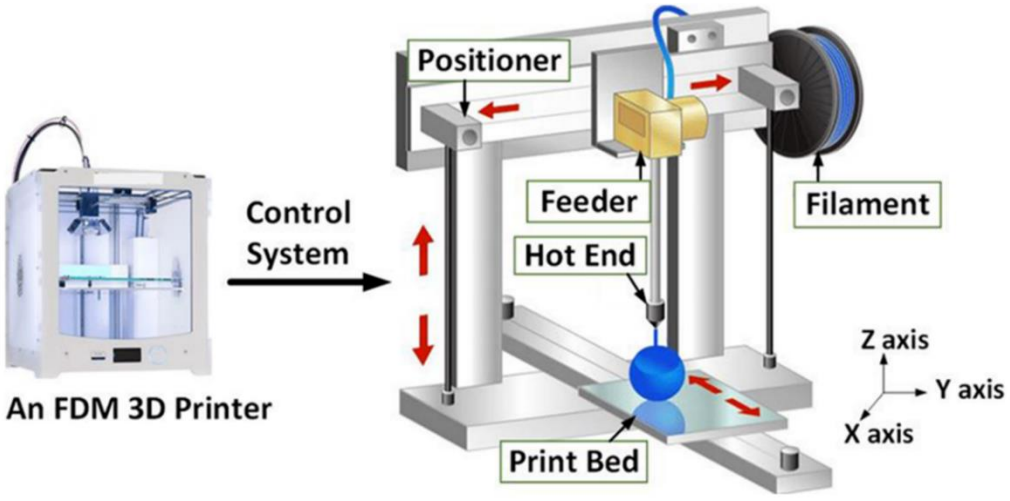

Fig. 63 FDM printer system

The movement of the printing nozzle is controlled by a numerical program and follows the precise path instructions generated by slicing software. The print bed is

heated to ensure that the first layer adheres quickly, providing strong adhesion and stability for the printed object after cooling. As each layer is completed, the printing nozzle is raised vertically by a settled distance, allowing the next layer to be deposited.

FDM printers support a wide variety of consumable materials, the most common being high-performance polylactic acid (PLA) and acrylonitrile butadiene styrene (ABS). Other thermoplastics such as nylon, ULTEM, polyetheretherketone (PEEK), polypropylene (PP), polyphenylsulfone (PPSF), thermoplastic polyurethanes (TPU), polyvinyl alcohol (PVA), high-impact polystyrene (HIPS), and composite filaments can also be used (Rajan & et al., 2022). These materials are generally economical, widely available, and many are biodegradable with good mechanical properties, thus significantly reducing the cost of FDM printing.

However, the layer-by-layer stacking method of FDM causes noticeable layer lines textures on the model's surface, resulting in relatively high surface roughness, so post-processing such as sanding or coating may be needed to achieve the requirements. Moreover, due to limitations in nozzle diameter and extrusion precision, FDM printing is limited in representing fine textures and complex structures, making it not suitable for microscale detail replication (e.g. in small-scale statue replication, fully presenting intricate carvings or surface cracks may not be achievable with FDM) (Fig. 64).

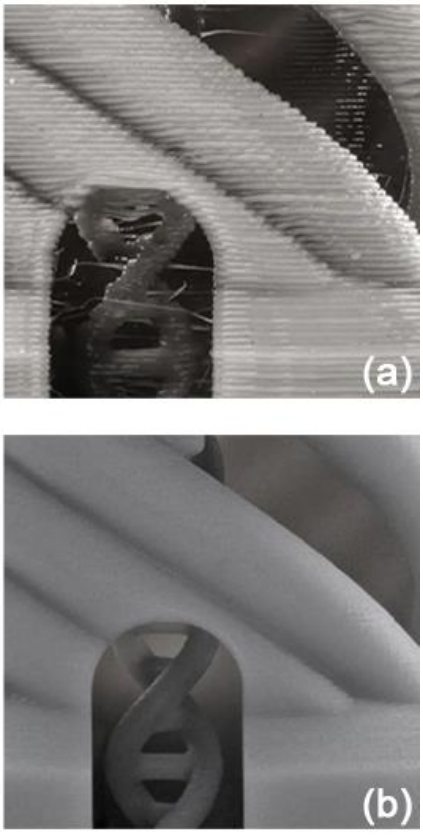

Fig. 64 Detailed comparison of FDM and VPP printed parts

Nevertheless, the visible layer lines can sometimes become advantages, for example for the terrain models, they can naturally provide an aesthetic similar to contour lines. Overall, although FDM has an inherent defect in precision, its relatively low cost, wide selection of material options, ease of operation, and good

performance make it one of the most widely used and practical 3D printing technologies today.

5.1.2 Vat photopolymerization (VPP)

Vat photopolymerization (VPP) is one of the most precise and detailed molding method in additive manufacturing, with representative technologies including Stereolithography (SLA) and Digital Light Processing (DLP) (Subedi & et al., 2024). The principle of these technologies is to selectively expose liquid photosensitive resin to light, and then causing rapid curing in specific regions and building up the object layer by layer (Fig. 65).

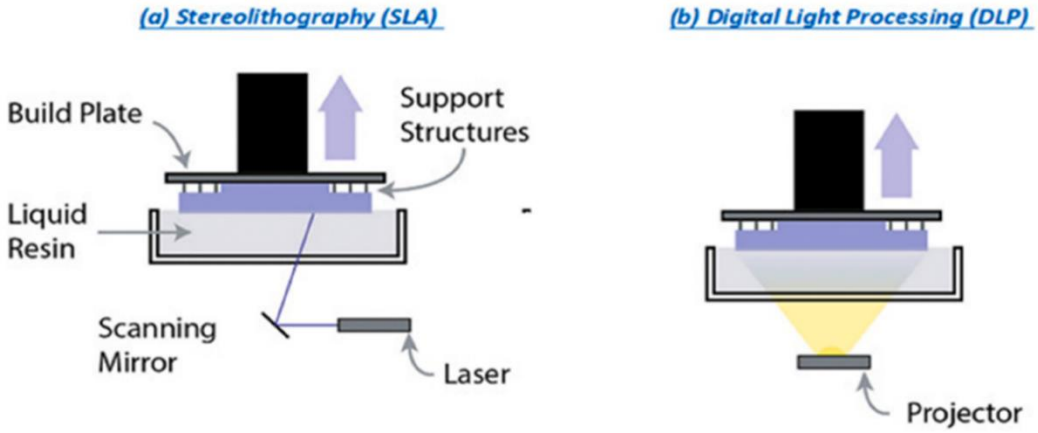

Fig. 65 Composition and Logic of SLA and DLP Printed Parts

Because the curing process is directly controlled by the light source, the molding quality is highly controllable, making VPP the preferred choice for producing models with fine details, complex structures, or high surface finish requirements. However in terms of forming mechanisms, SLA and DLP are with different curing methods. SLA employs a ultraviolet (UV) laser beam to trace the cross-sectional shape point by point along the laser 's path, while DLP uses a projection system to project UV laser on the build platform and curing the entire section layer at once (Quan & et al., 2020). In general, SLA can produce larger parts with smoother and more uniform surfaces, while DLP offers faster printing speed (McClements, 2022) (Fig. 66). Additionally, due to the uniformity of material supply, VPP cannot achieve the same level of material switching during printing respect to FDM. However, the

ability of VPP to provide smooth surfaces and extremely low visible layer lines remains unmatched by material extrusion technologies like FDM.

Fig. 66 Composition FDM, SLA and DLP Printed Parts

5.1.3 Technology choices in the case

By comparing the characteristics of the two technologies, it is reasonable to conclude that FDM is more suitable for larger-scale and rapid printing tasks (e.g., site-scale restorations), and photopolymerization is better for small-scale and high-precision models (e.g., reproducing architectural details at 1:50 or 1:20 scale). For this case, the required model is relatively large, and the focus is on the overall terrain and the spatial relationships of key features rather than microscopic textures. Based on a comprehensive evaluation as well as taking into account the project budget, FDM was ultimately chosen as the printing method (Fig. 67).

Fig. 67 Comparison of preliminary test FDM and VPP printed models

5.2 Model Structure Planning

To achieve the goal of integrating the digital reconstruction with narrative representation, the team decided to produce a physical model, on which the video mapping would be projected. Considering the complexity, production schedule, budget and final exhibition effect, the model scale was determined to be 1:500 according to the calculation based on the point cloud density.

The choice of this scale aims to preserve details under a suitable scale, while at the same time balance the printing time within a reasonable range, and to ensure that the final effect is appropriate for display while still allowing viewers to clearly observe its structural details and meet the need of video mapping. The terrain components of the model are produced using 3D printing, while the non-visible height differences are substituted with medium-density fibreboard (MDF) cut to match the dimensions of the printed modules (as detailed in the following section). To ensure the stability of the model, the assembled model (3D printing tiles + wood tiles) is placed on an MDF base (wood base) and aligned using a thin cardboard sheet engraved with a laser-cut positioning grid (Fig. 68).

The model finally used a total of 36 3D-printed modules, 181 MDF panels measuring 20 cm × 20 cm, 4 thin cardboard sheets (0.6 m × 0.9 m) laser-engraved, and 1 MDF panel with hinges that can be opened in half (1.2 m × 1.8 m when unfolded). To reduce light reflection in the projection, the entire model was eventually painted in dark grey.

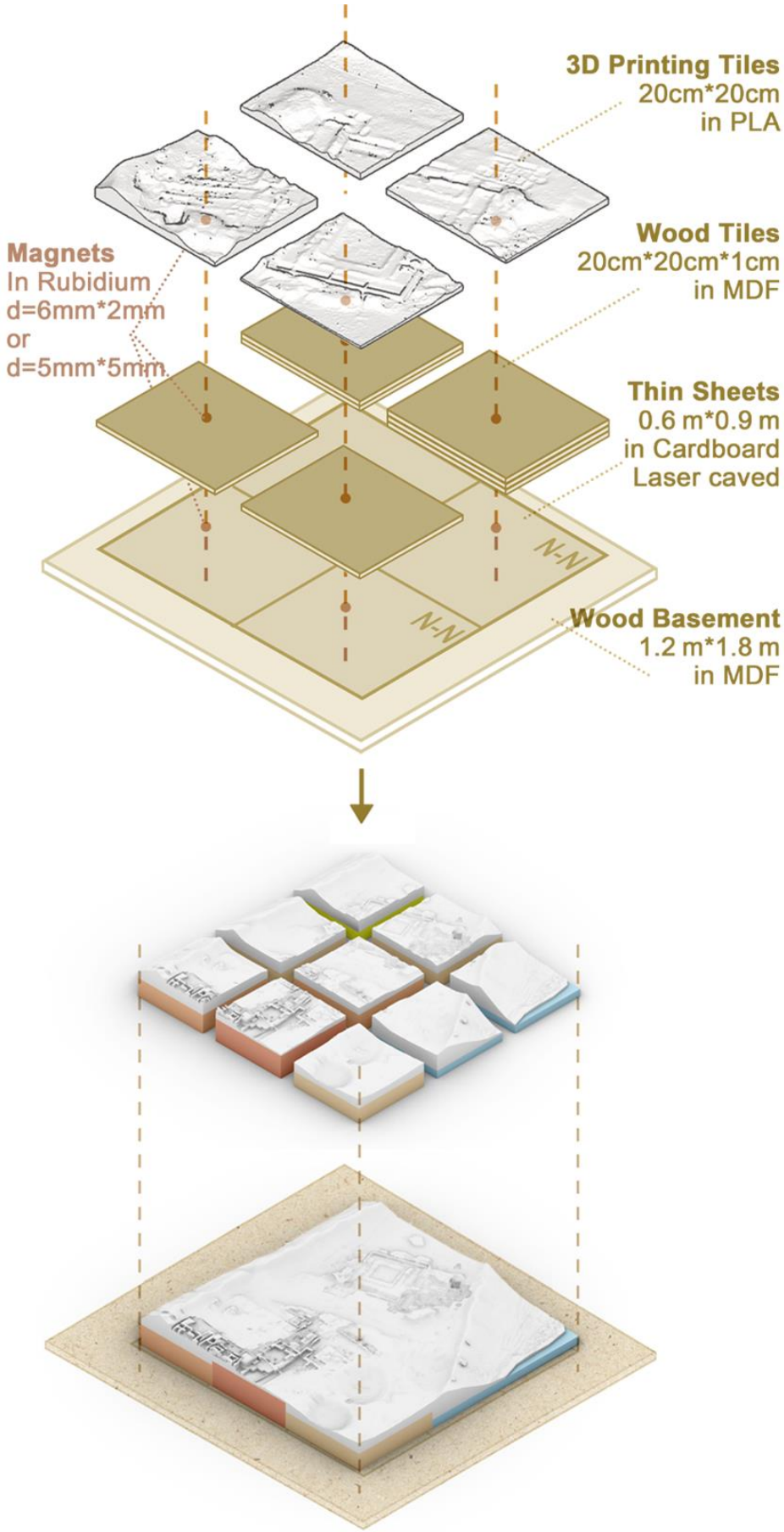

Fig. 68 Model structure arrangement

5.2.1 Model organization strategy

To ensure that the exhibition remains clearly focused, the model is designed by cutting the Old Nisa site along the outer edge of the foothills with the verification from archaeologist, in order to remove traces of the modern city and save extra work. The site is then rotated 36° counterclockwise to improve readability. After cutting and rotation, the retained area of Old Nisa measures approximately 600 meters in width and 700 meters in length. At the scale of 1:500, the resulting physical model would therefore measure roughly 1.2 m × 1.4 m.

Taking the laboratory's test printer (LOTMAXX Shark V2) as an example, its maximum build volume is only 235 mm × 235 mm × 265 mm, which is far exceeds the printing limit of the existing equipment in the lab. Obviously printing the model as a single piece is impossible, thus the model must be designed in segments.

To address this issue, the team decided to develop a control grid scheme (Fig. 69). The main idea of the approach is constructing a control mesh based on actual coordinates within the Rhino (a commercial 3D modeling software) environment. Each grid cell corresponds to a fundamental unit of 100 m by 100 m in the model space (referred to as one tile), ensuring that each module remains within the printable size limit of 20 cm by 20 cm. Each tile can be indexed using a column-row coding format (e.g. the first row in the second column is labeled as 2-1), which facilitates later assembly. Considering the text descriptions are also required in the video mapping, additional blank and flat platforms is necessary. Therefore, two additional rows of tiles are added above and below the tiles that carry the 3D printed parts. The final model size was determined to be 1.2 m by 1.8 m, divided into 54 tiles in total, among which 36 tiles are the base with the 3D printing attached and 18 tiles are blank bases (Fig. 70).

The terrain of Old Nisa shows a significant variation. GIS analysis indicates that, the highest point within the preserved area is located at the southwest corner of the city wall (371.78 m above sea level), while the lowest point is located at the northeast foot of the mountain (331.93 m above sea level), with an elevation

difference of approximately 40 m, which corresponds to a height difference of about 8 cm in the physical model. To ensure that the printed model can placed stably on the exhibition table and to reduce material consumption and printing time as much as possible, the team decided to use medium-density fibreboard (MDF) material instead of 3D printed components to replace the non-visible portions of the model. The workflow is as follows:

1) Calculating the highest point (h_{max}) and lowest point (h_{min}) of the mesh within each tile.
2) Identifying the lowest point of the entire mesh (H_{min}), and computing the difference between h_{min} and H_{min} as Δh (Table. 8).
3) Using the tile containing the lowest point (331.93 m) as a reference, the value of Δh can be observed to be in the threshold range of 0 m to 20.4 m (0 cm to 4.08 cm). Therefore, 1 cm thick MDF board is selected to replace the printing material with a contour line spacing of 5 m (1 cm in the model). Therefore, each tile will have a different number of MDF boards depending on its height, with a minimum of 2 layers and a maximum of 6 layers.
4) Based on the layer number of MDF boards, the tiles into 5 different levels, attempting to minimize printing time/material consumption and simplify the work involved in adding a base.

Table. 8 Tiles Height Calculation

Code (X-Y)	MIN (M)	MAX (M)	ΔMIN-MIN (M)	Base	Code (X-Y)	MIN (M)	MAX (M)	ΔMIN-MIN (M)	Base
1-1	320.38	325.38	/	2	4-1	320.38	325.38	/	2
1-2	335.28	342.79	3.35	2	4-2	331.95	344.30	0.02	2
1-3	340.23	342.18	8.30	3	4-3	332.63	357.56	0.70	2
1-4	340.83	349.41	8.91	3	4-4	332.78	357.06	0.85	2
1-5	343.11	354.27	11.18	4	4-5	344.20	356.26	12.28	4
1-6	343.26	355.37	11.33	4	4-6	345.79	354.17	13.86	4
1-7	344.18	356.65	12.26	4	4-7	349.96	363.43	18.03	5
1-8	325.38	330.38	/	4	4-8	341.34	363.28	9.42	4
1-9	325.38	330.38	/	4	4-9	325.38	330.38	/	4
2-1	320.38	325.38	/	2	5-1	320.38	325.38	/	2
2-2	334.73	358.69	2.80	2	5-2	320.38	325.38	/	2
2-3	340.46	358.98	8.53	3	5-3	320.38	325.38	/	2
2-4	341.30	362.64	9.37	4	5-4	332.63	357.59	0.71	2
2-5	350.51	368.83	18.59	5	5-5	338.45	363.32	6.52	3
2-6	351.37	371.12	19.44	6	5-6	337.49	363.08	5.56	3
2-7	345.58	371.78	13.65	4	5-7	339.55	363.40	7.63	3
2-8	345.02	350.90	13.09	4	5-8	341.34	363.42	9.42	4
2-9	325.38	330.38	/	4	5-9	325.38	330.38	/	4
3-1	320.38	325.38	/	2	6-1	320.38	325.38	/	2
3-2	331.93	357.93	0.00	2	6-2	320.38	325.38	/	2
3-3	344.37	355.94	12.45	4	6-3	320.38	325.38	/	2
3-4	349.61	357.30	17.69	5	6-4	320.38	325.38	/	2
3-5	352.32	364.78	20.40	6	6-5	334.84	348.77	2.92	3
3-6	351.53	365.71	19.61	6	6-6	336.52	347.63	4.60	3
3-7	348.09	369.41	16.16	5	6-7	336.53	339.55	4.61	3
3-8	342.57	350.63	10.64	4	6-8	336.99	344.22	5.06	4
3-9	325.38	330.38	/	4	6-9	325.38	330.38	/	4

*MIN of MIN value of all tiles: 331.93 M
*MIN of MAX value of all tiles: 371.78 M

Fig. 69 The model is divided into blocks based on altitude

Fig. 70 Number of layers of the wooden support base determined based on the zoning

5.2.2 Model connection strategy

In terms of the assembly design of the model, various connection node forms were tried in the early stage of the research, including sliding fits and interlocking joints (Fig. 71), with initial expectation of allowing 3D-printed components to interlock with each-other directly without adding the base. However, experiments showed that these connection methods are difficult to maintain self-stability and lead to relative sliding or loosening between the tiles, making the addition of the base necessary. Considering that the model might later be used for other inclined displays or individual module exhibitions, it was ultimately decided to adopt a magnetic connection scheme. As a connecting medium between the 3D-printed parts and the wood tiles (also between the wood tiles and the wood base), magnets allow for quick assembly and disassembly as well as stable adhesion, making the structure more flexible and maintainable.

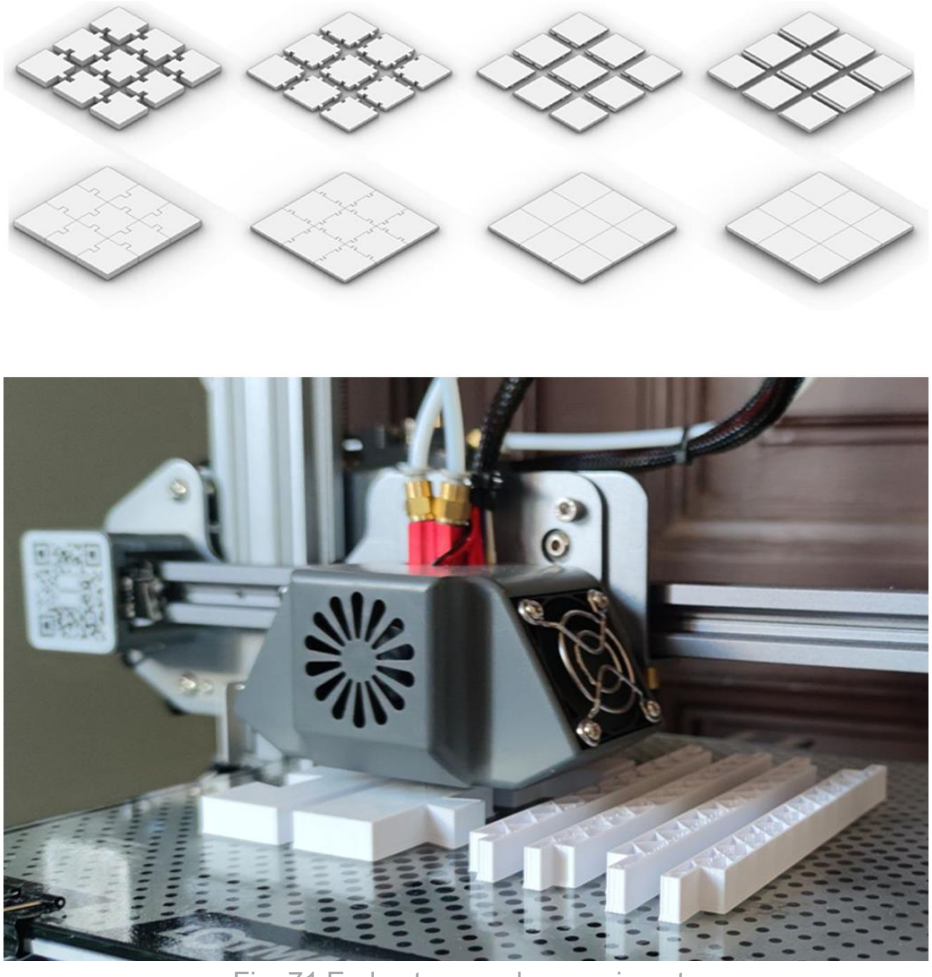

Fig. 71 Early-stage node experiments

For the magnet arrangement, a layered placement strategy was developed to balance stability and cost. Specifically, all 3D-printed modules are connected to the wood tiles with two diagonally arranged magnets to fix its orientation, while the connection between the wood tiles and the wood base depends on the number of wood tile layers in each module: for 2 layers, 2 magnets are arranged diagonally; for 3-4 layers, 3 magnets are arranged in a triangular pattern; and for 5-6 layers, 4 magnets are arranged in a square pattern (Fig. 72).

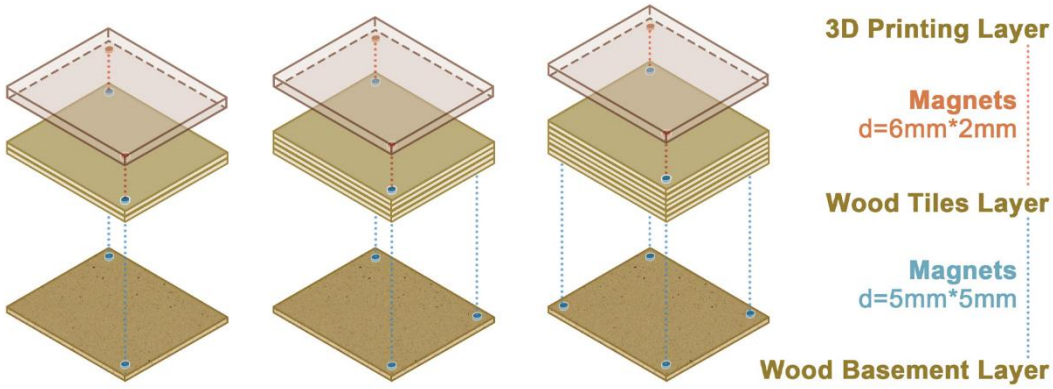

Fig. 72 Arrangement of magnets

5.3 Mesh Repair and Printing Preprocessing

Although the initial mesh exported from CloudCompare already captured the general shape, it still exhibited issues such as surface damage, non-manifold topology, and distorted details. To ensure the model's integrity and printability, further repair and preprocessing are done in commercial 3D modeling software Rhino. The cleaned and optimized mesh was then prepared for printing using slicing software.

5.3.1 Mesh processing

The work carried out in Rhino maintains the same spatial coordinate system as the real-world geographic coordinates to ensure absolute alignment and facilitate future replacement needs. The specific workflow mainly included the following steps:

1) The mesh resolution can directly affect the information density that the final 3D model can provide (in other words the model's ability to reproduce geographical features). Simplification tests showed that, a reduction to 80-90% in general does not affect the printing accuracy of the model but greatly alleviates lag during processing (Fig. 73). Therefore, the primary task has to be the simplification of mesh faces number, in order to reduce the computational load on the computer and to improve work efficiency. The specific reduction rate should be determined according to the characteristics of the target object, with areas of high-density information preserved to retain necessary detail.

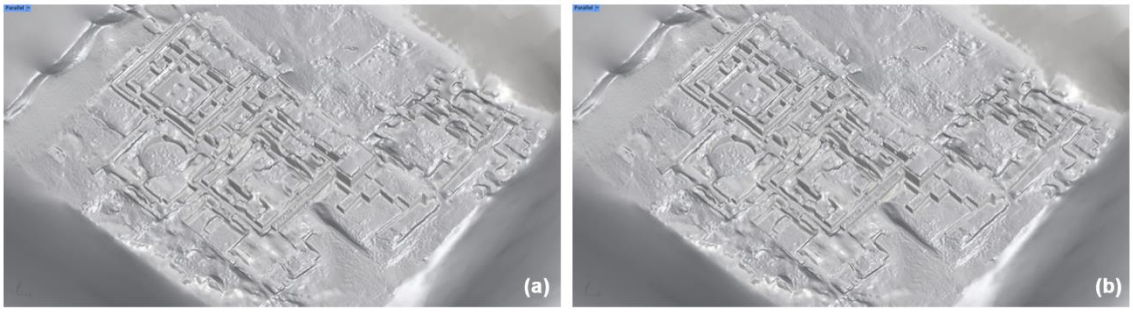

Fig. 73 Mesh face reduction, before (a) and after (b), very slight impact on precision

2) The mesh is then trimmed and cleaned restricted to the control grid, redundant edges were removed to define each tile's corresponding area, and irregularly shaped areas are cleaned subsequently. Due to the presence of a small amount of unavoidable mild point cloud noise, mesh reconstruction sometimes produce meshes that deviate from reality because of sudden vector changes, these are defined as "noise meshes" here (Fig. 74, a).

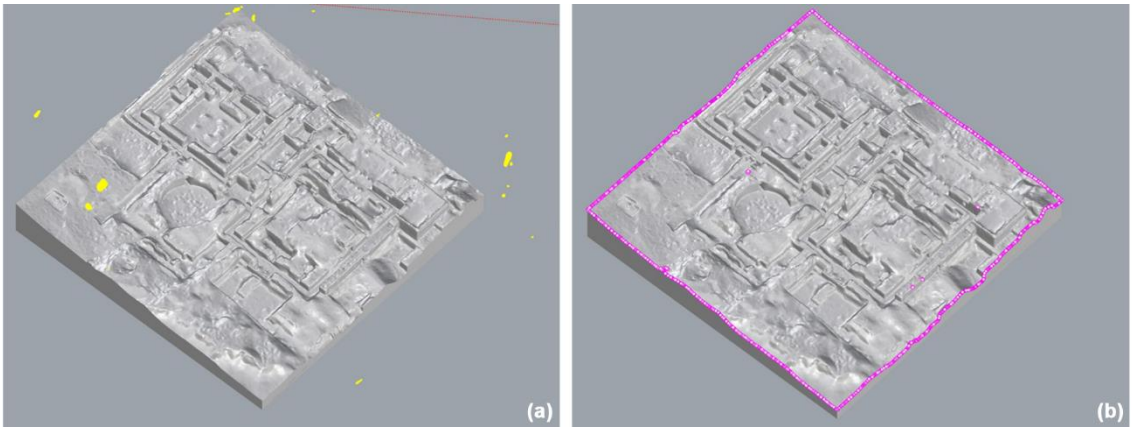

Fig. 74 (a) Filter of Noise meshes (b) check of abnormal edges

Noise meshes are divided into two categories: independent from the main mesh surface, or attached to it. In the first case, the meshes can be deleted directly. In the second case, irregular parts need to be carefully screened and deleted manually, then repaired or simplified according to photographic references and morphological logic to reflect the actual situation. To avoid noticeable edges at repair sites, sometimes the *smooth* command is needed to ensure gradual transitions between the repaired area and the original mesh. Poisson surface reconstruction may also result in small mesh gaps occasionally, but typically limited to one or a few triangles, in this case these minor losses can be directly patched using the edges of the holes. After the cleaning and repair process, an edge check should be performed to identify any open edges and ensure that each mesh has only four sides open where intended (Fig. 74, b).

3) The next step is converting the cleaned mesh into a solid with height. Based on the cleaned mesh, a height was added to transform the mesh from a surface

into a closed solid which can be recognized by 3D printer. Specifically, the minimum point on the mesh surface was determined using Rhino's built-in Grasshopper module or object information *check* tools. At least 2mm of excess thickness was added, to prevent breakage during printing. The main challenge in this step is that, the trim algorithm from the previous step may occasionally mis-identify edges. Therefore, the edge lines need to be checked to ensure that the four sides of the tile mesh lie on the same horizontal plane in the X/Y axes. Both face-trim (mesh clipped by intersecting planes) and line-trim (mesh clipped by non-intersecting but top view aligned grids) methods were tested, but their error occurrences are random.

Face-trim was preferred, because under normal conditions, trimming with four vertical planes (slightly larger than the reserved area for software recognition) and one horizontal plane, followed by joining all remaining faces, produces a closed solid directly. However, this is not guaranteed. When direct solid formation fails, line-trim is applied from a top-down view to cut the mesh, followed by verification that all points along the four edges lie on the same X/Y horizontal plane. Any deviations are corrected by unifying the X/Y coordinates; otherwise, the surface cannot be closed. Afterward, lines are inserted from the four vertices of the mesh using the calculated height, and planar surfaces are generated sequentially between the line framework and corresponding mesh edges. The final combination of these surfaces forms a closed solid.

4) Finally, each tile's base should be numbered, and all tiles are confirmed as closed solids, then the tiles were scaled down to the 1:500 scale. To prevent model loss in the slicing software due to excessively large coordinates, the tiles should be moved close to the origin point of the model space coordinate system and exported individually in STL format.

5.3.2 Printing presets

Since STL files cannot be directly recognized by the 3D printer system, they need to be imported into slicing software for preparation. Slicing software Lotmaxx 4.2 developed by the Shark V2 manufacturer was used as an example here, to adjust the printing parameters for one tile covering the northern archaeological area. The key parameters during the slicing stage are as follows:

1) Layer height is a critical factor affecting printing precision and time. Smaller layer heights provide higher surface detail, but significantly increase printing time. In this test, a normal layer height of 0.2 mm was chosen to balance terrain detail level and printing time (Fig. 75).

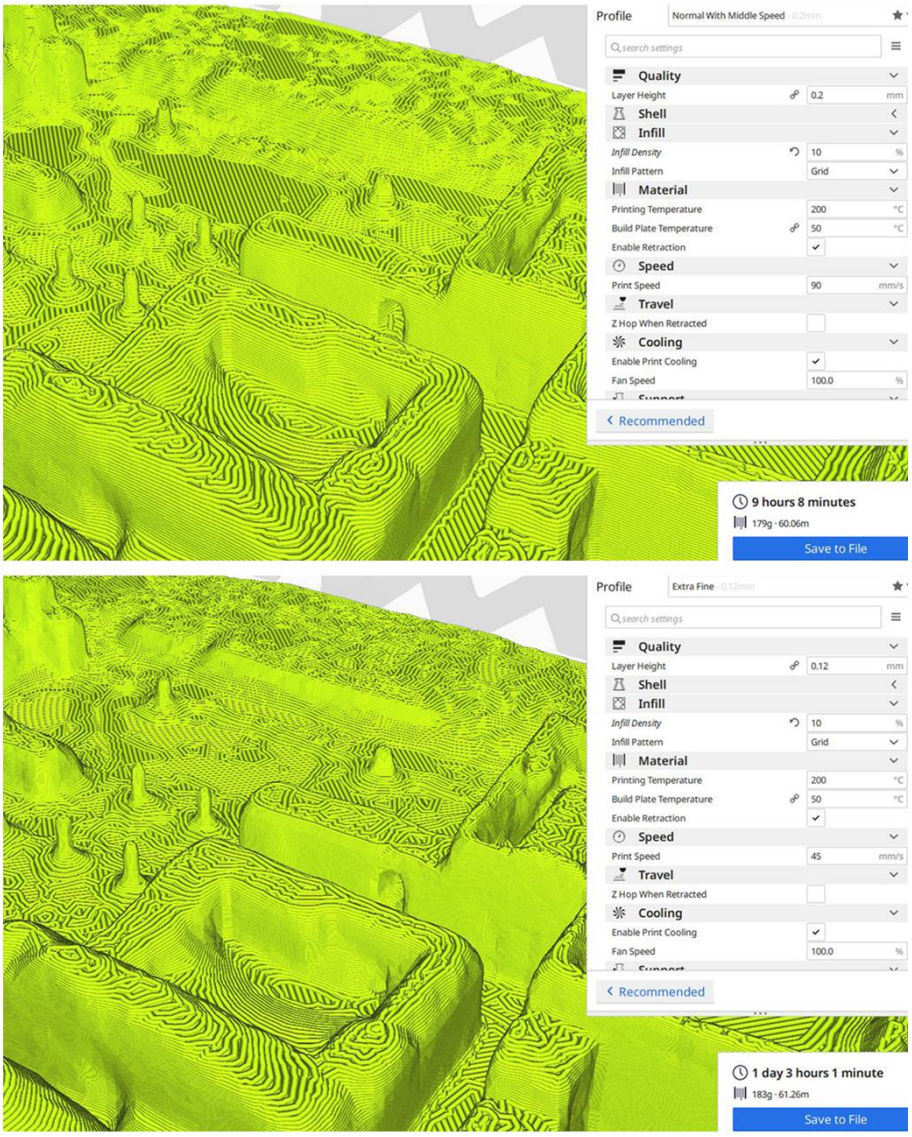

Fig. 75 Comparison of time consuming under different layer thickness: Depending on the required precision, a printing time difference of more than ten hours can be achieved.

2) Infill density of 10% was used to ensure structural strength while minimizing unnecessary material consumption and printing time. After consideration, infill with *Grid* pattern was selected (Fig. 76).

3) Nozzle and heated bed temperatures were adjusted according to the material properties. For testing material PLA, the nozzle temperature was set to 200 °C to ensure smoothly extrusion, and the heated bed was set to 50 °C to maintain stable adhesion of the print and prevent warping.

4) Although there were no overhangs on most of the model's surface, support was required for the magnet holes at the base and the relatively thin areas of the numbering. *Grid* pattern supports were selected to balance ease of removal with print quality.

5) Printing speed also directly affects model quality and detail clarity, excessive speed can cause uneven material deposition, stringing, or distortion of details. During testing, the internal infill part was mainly printed at 90 mm/s, while the exterior surfaces printing speed were settled as 60 mm/s to balance quality and time (Fig. 75).

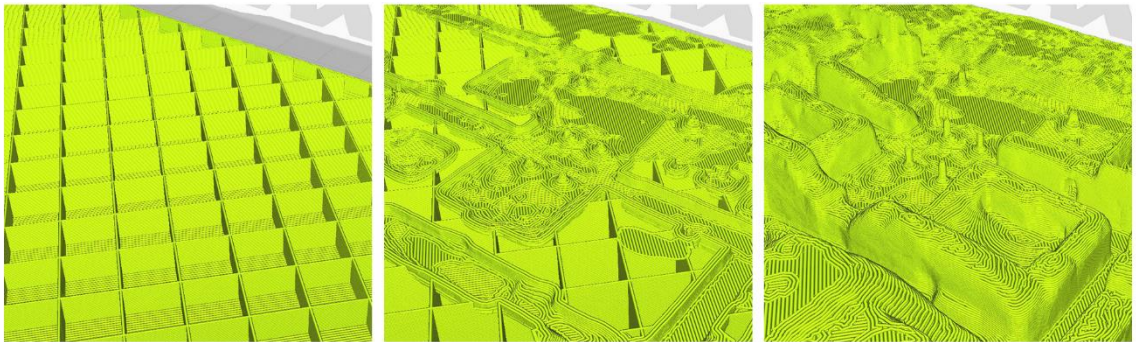

Fig. 76 Printing process preview

5.4 Printing Tests and Issue Summary

Preliminary print tests were conducted on four modules with high-density excavated buildings (tiles 2-5, 2-6, 3-5, 3-6) to verify assembly accuracy and surface quality. The results showed that the modules fit together well, terrain transitions were natural, and structural alignment was high (Fig. 77). Due to machine malfunctions at the G4CH Lab and time constraints, the printing task was reassigned to the Laboratori Modelli Reali (MODLAB) and Laboratorio Modelli Virtuali (VIRTUALAB) of Politecnico di Torino, the final printing task was completed collaboratively by both parties.

During the magnet-insertion hole test, the initially designed hole diameter allowed a tight fit. However, in actual printing, because the holes were printed inverted (the caved areas are at the bottom of the tiles) and minor differences caused by printers changing, some holes happen dimensional deviations and making it difficult to insert the magnets. To solve this problem, the hole was enlarged by manual grinding to ensure stable magnet placement. This step highlights the necessity of reserving tolerance margins during the design stage, which can significantly reduce post-print manual adjustments.

Additionally, the printed numbers were clearly visible in the initial tests, but after changing machines and increasing print speed in later stages, some numbers became fuzzy or part missing, ultimately requiring hand-written replacements. This experience indicates that fine details should be given generous dimensions to accommodate printing variability, and that a balance must be struck between precision and speed in large-scale printing.

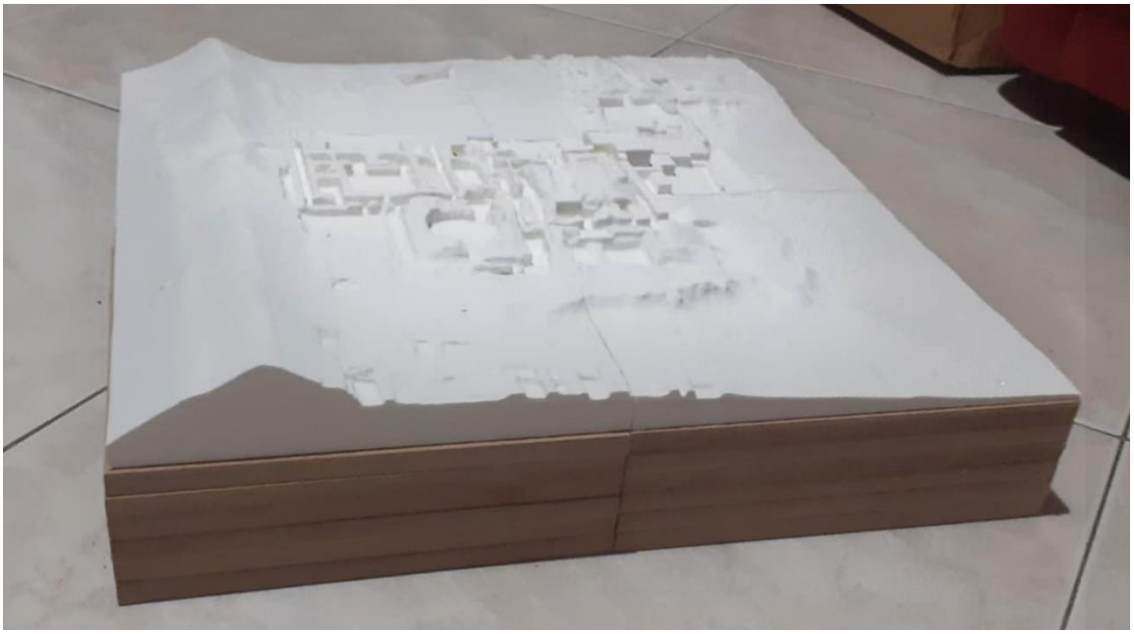

Fig. 77 Early-stage assembly of tiles 2-5, 2-6, 3-5, and 3-6

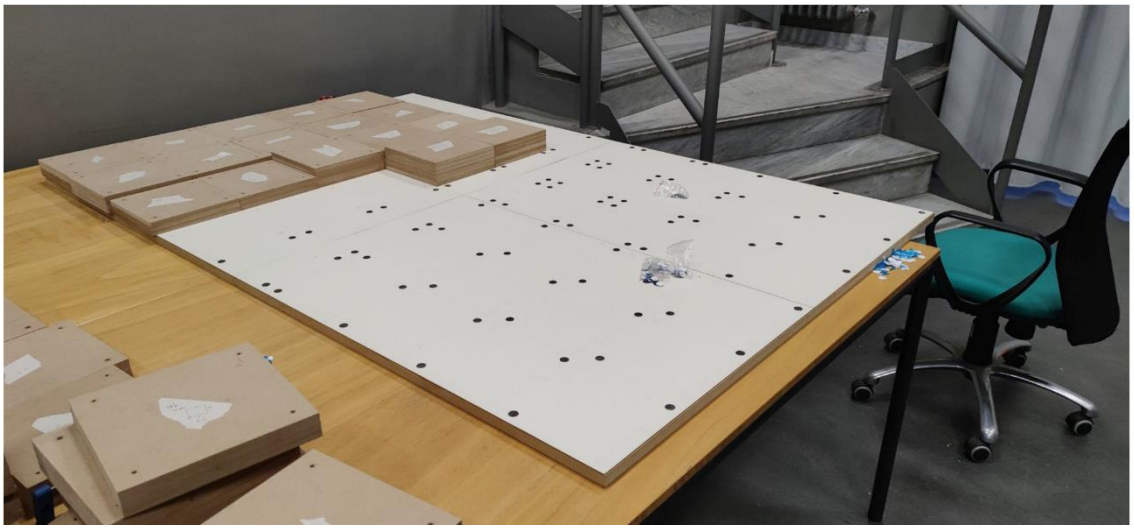

Fig. 78 Final assembly of the basement

5.5 Model Assembly and Structural Optimization

During the model assembly process, the main issues encountered were related to wood board cutting deviations and magnet alignment offsets. The preliminary wood cutting test was supported by an external service, however due to budget constraints, the woodworking tasks in the subsequent production phase were supported by MODLAB Design.

In initial tests, the cutting quality was excellent, with smooth and even edges suitable for gluing, while during large scale production, some boards failed to maintain strictly vertical cutting angles, causing slight misalignments when assembling certain modules. These deviations were enlarged across multiple tiles, and further affecting the continuity of the overall surface. To decrease the cumulative impact of such errors, the edges of the wood tiles were later re-sanded and polished to improve joint fit, which significantly enhancing the flatness of the assembled tiles.

On the other hand, offset issues during magnet attachment were caused by a combination of factors, including differences in magnet specifications and the manual positioning of the hole in the wooden tiles. Considering the structure feature of the model, the parts attached with 3D-printed components used cylindrical magnets with a diameter of 6 mm and a thickness of 2 mm, while the wood tiles used cylindrical magnets with a diameter of 5 mm and a thickness of 5 mm. The differences in dimension combined with manual positioning errors in drilling the holes on the wood, sometimes led to offsets when the magnets coupled. These misalignments were subsequently adjusted manually, ensuring the overall stability of the assembled model.

Generally, this test established a generally applicable workflow, including grid-control based segmentation, optimized printing, and assembly strategies. As a non-destructive and detachable structural solution, magnetic connections proved highly convenient for maintenance, repeated disassembly, and modular transportation. However, since the accuracy of magnetic connections highly relies

on fabrication precision, future work could explore laser cutting or computer numerical control (CNC) drilling to align positioning holes more precisely, thereby reducing errors caused by manual adjustments. Additionally, while wood provides a stable base material, it has limitations such as high weight, processing difficulty, and relatively high cost, thus future exploration may consider lighter and more easily processed alternative materials based on practical needs. Finally, the experience from this study indicates that for multi-step and multi-material model fabrication workflows, it is crucial to conduct small-scale but full-process tests early, and to predict possible unexpected situations at key stages whenever possible.

In summary, this workflow offers valuable reference for restoration of geomatics surveying results, the transformation from digital to physical models, and heritage display. The identified advantages and limitations also provide a certain insight for planning large-scale site models.

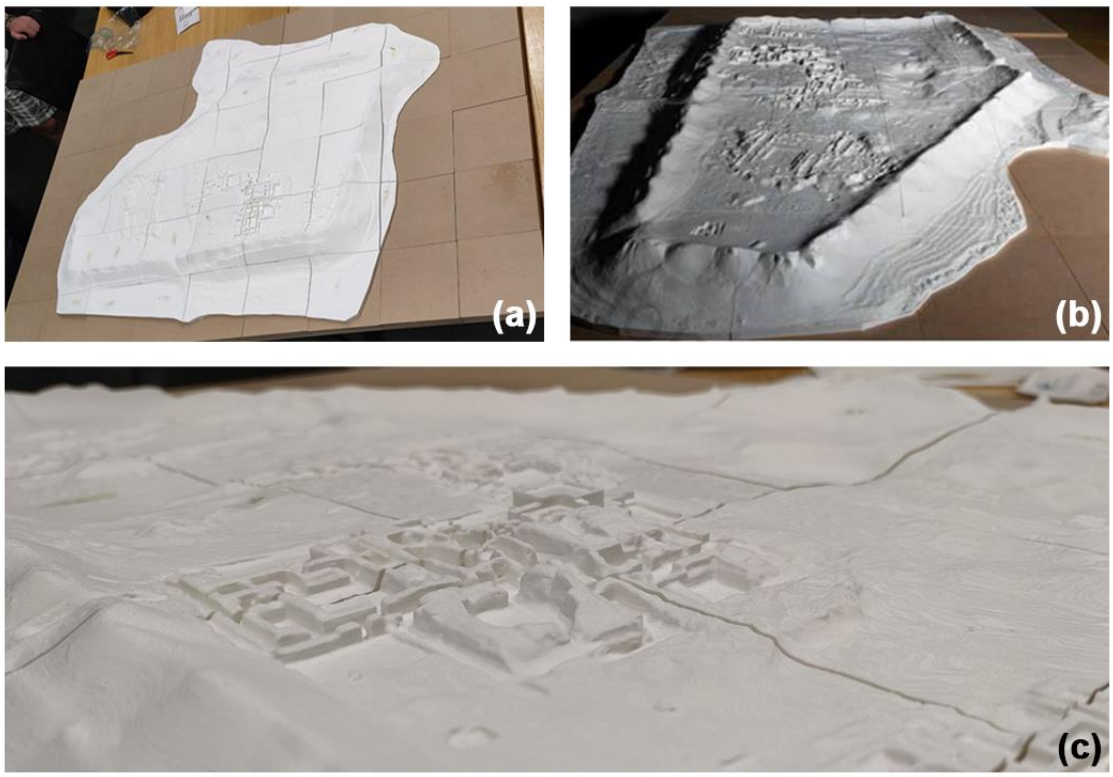

Fig. 79 Final assembled model (a),
painted model (b),
and detail of the model, central complex part as example (c)

Chapter 6: Video mapping production process

6.1 Theoretical Background and Application Directions of Video Mapping

As an important subcategory of Augmented Reality (AR), Spatially Augmented Reality (SAR) has video mapping (projection mapping) as one of its typical applications (Maniello, 2023). It is a method that uses multimedia technologies to project dynamic graphics precisely onto irregular physical surfaces, thereby producing an immersive visual experience by spatially augmented reality (Maniello, 2015).

From the technical perspective, the principle of projection mapping is to maintain the integrity of the physical structure while using a projector to project light accurately onto the surfaces of corresponding geometric forms. In this way, the visual appearance of the physical environment can be transformed without any actual physical intervention (Fig. 80). Its non-destructive and reversible features distinguished it from traditional approaches that may require the removal of physical structures (Chaiyatham, 2022).

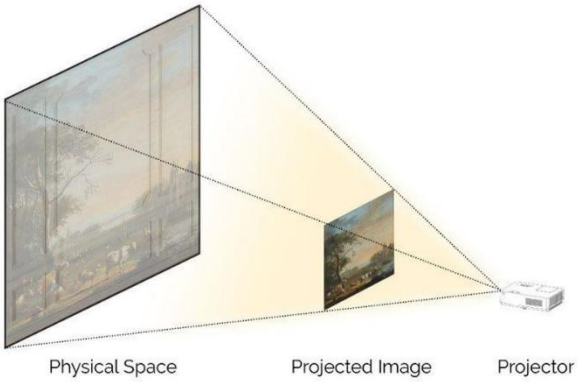

Fig. 80 Principle of projection

The technology breaks through the traditional dependence of projection on flat surfaces, enabling buildings, models, and sculptures to become the presentation media also. Compared with traditional static display methods, video mapping provides physical models with multidimensional expressiveness through the integration of light, sound, and dynamic images. It has opened up new possibilities for narrative and has been applied in a wide range of fields, including education, exhibition, art, science and so on (Pogumax, 2024). Especially in the field of cultural heritage preservation and presentation, as an intervention method,

projection mapping not only effectively protects the integrity of physical objects, but also significantly enhances the flexibility and variability of display. By updating the projected content, multiple scenes and cross thematic visual narratives can be presented without altering the original appearance of projected objects, thus greatly enriching presentation format. At the same time, it can effectively reduce operational costs and enhance visitor experience, providing a solution for heritage display that combines preservation with innovation.

In this context, this project adopts a combined approach of 3D printing and video mapping to improve the efficiency and attractiveness of site’s presentation.

6.2 Curatorial Strategy and Video Mapping Related Design

6.2.1 Basic exhibition information

The exhibition is entitled “Antiche civiltà del Turkmenistan (Ancient Civilizations of Turkmenistan)”, held in the ground floor galleries of the Palazzo dei Conservatori at the Capitoline Museums in Rome from 25/10/2025 - 12/04/2026. This exhibition is a result of a long-term collaborative projects in Turkmenistan conducted by the International Association of Mediterranean and Eastern Studies in Rome (ISMEO) and the Center for Research and Archaeological Excavations in the Middle East and Asia in Turin (CRAST), with final support from the Ministry of Culture of Turkmenistan and the University of Turin.

The exhibition covers representative artifacts from the prehistoric Margiana culture of the 3rd and 2nd millennia BC and from the ancient Parthian period. A number of valuable objects shown outside Turkmenistan for the first time are included, such as gold and semiprecious stone necklaces from Gonur, unbaked clay portrait figures of kings and warriors, and richly decorated ivory rhytons excavated from the Old Nisa, dating from the 2nd century BC to the 1st century AD (Musei Capitolini, 2025).

The exhibition is organized into two main sections. The first part introduces the culture and art of Bronze Age Margiana, while the second part focuses on another important historical phase in ancient Turkmenistan, the Parthian kingdom, and presents the archaeological discoveries from the site of Old Nisa. In addition to artifact displays, the exhibition also introduced multimedia content, including interpretive panels, video materials, and 3D reconstructions. Particularly noteworthy is the video mapping device that projects dynamic images onto a 1:500 scale model, allowing visitors to gain an immersive understanding of the current condition of the ancient site of Nisa and the scientific basis of its reconstruction. The digital and physical models, together with geographically related data were provided by the G4CH Geomatic Laboratory of Politecnico di Torino. Historical information and textual interpretation were supported by CRAST, while the

integrated projection production was completed by the MULTIMEDIALab of Politecnico di Torino. The narrative framework of the projected content was together developed by the three parties (Fig. 81).

Fig. 81 Exhibition site

6.2.2 Purpose and planning of video mapping

The video mapping installation aims to transform the complex archaeological information of the Old Nisa into a clearly structured and easily comprehensible narrative system. In this way, even visitors completely unfamiliar with knowledge of Parthian history are able to understand easily the spatial organization, historical background, and archaeological discoveries of the site. The projection is not set as a decorative layer on the model, but rather an essential interpretive medium that provides visual guidance to help viewers review the Old Nisa across the dimensions of time and space.

6.2.2.1 Content organization

To achieve this goal, the narrative framework was designed to examine the evolution of the Parthian dynasty within a broader geographical and historical context. The focus then gradually shifts toward the urban features of the Old Nisa, presenting the image of the dynasty through architecture and artifacts, and finally concludes with the current state of the site and ongoing archaeological work. The linear structure ensures that visitors not only observe isolated architectural remains, but also understand their evolution as a cultural landscape over time.

The structure of the video content aligns with the overall exhibition narrative logic. The video mapping is organized in a temporal-spatial-temporal interwoven framework, presents the story through visualization. Based on this logic, the projected content is divided into three stages, beginning with civilization level historical narration, moving to the overall layout of the site, internal architectural structures, excavated artifacts, and concluding with the modern condition of the site.

1) The first stage focuses on a macro historical perspective, including the rise of the Parthian dynasty and its interactions with civilizations of Central and Western Asia. Through maps, changes in ancient territories, and key historical events (see Chapter 2.1), this phase establishes the historical context needed to understand the foundation of Old Nisa (Fig. 82, a).

2) The second stage first concentrates on the site as a whole. High resolution rendering and slope analysis maps are used to outline the defensive system and urban pattern. The view then moves inside the site to illuminate

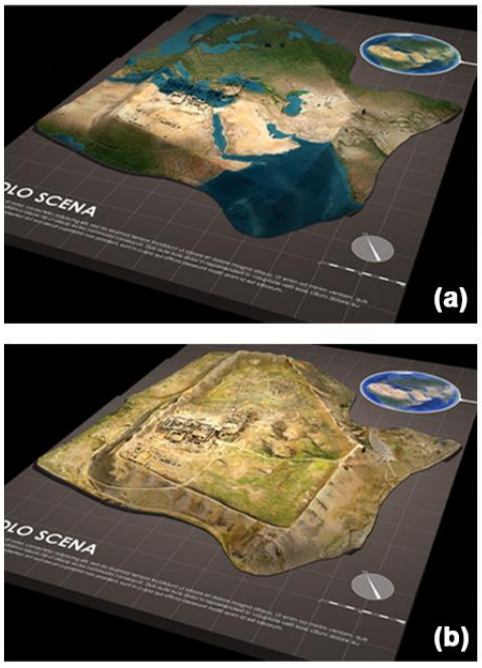

Fig. 82 (a) Global perspective phase
(b) Site focus phase

in sequence the main excavated architectural complexes, including the *Square House*, the *storage areas*, the *Central Building Complex*, and the *water basin* (see Chapter 2.2). Each area is accompanied by images and textual explanations of excavation contexts and related artifacts, linking functional elements such as storage, ritual practice, and water management. This helps visitors directly perceive the functional planning and atmosphere of the Old Nisa (Fig. 82, b, c, d).

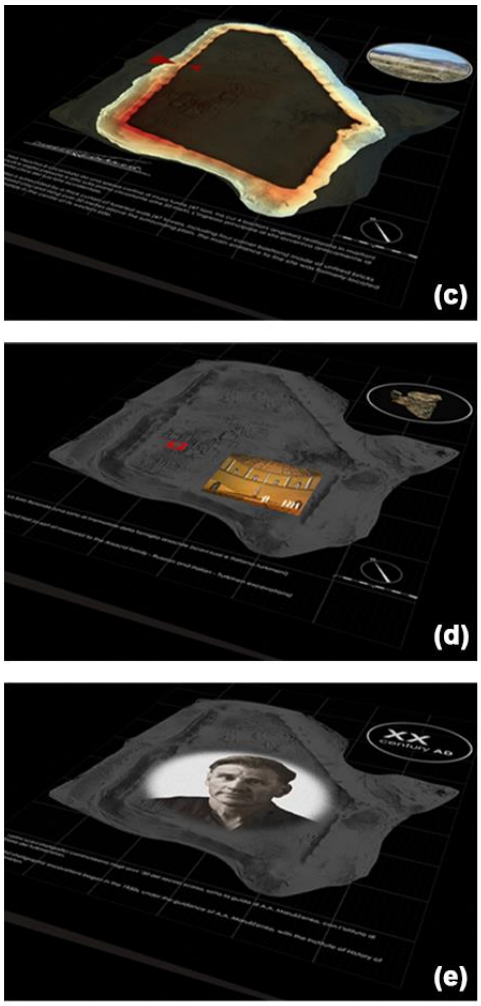

3) The third stage shifts the perspective back to the contemporary era. Through photographs and text, the show presents the continuous efforts of generations of archaeologists, conservation specialists, and surveyors. The digitization process of the site is also briefly illustrated by tracing scanning routes and observation points (Fig. 82, e).

6.2.2.2 Spatial arrangement and display logic of video mapping device

The video mapping installation is located on one side of the exhibition hall, surrounded by original artifacts from the site of Old Nisa, which creates a direct correspondence between the model and the physical objects. The lighting in the gallery is controlled, with the overall environment kept in dim. This enhances color contrast on the surface of the model, while also creating an immersive and focused viewing atmosphere. At the same time, the exhibited artifacts are illuminated independently, ensuring clear visibility without interfering with the projection.

The 3D printed model is placed horizontally on the display platform, while the projection is cast vertically from above. This allows visitors to move freely around the model along a circular route and to engage with the narrative from different viewpoints at any moment.

The model's size was chosen to fit the limitations of the curatorial space, it appropriately presents the overall layout of the site, while also effectively reproducing survey data and architectural details. This allows the projection to emphasize fine localized features, perfectly aligning with the methodology and objectives of this research (Fig. 83).

Fig. 83 Exhibition space arrangement

6.3 Production Workflow of Video Mapping

The video mapping workflow can generally be divided into three stages:

1) Projection Content Creation

Because the projection target is not a uniform surface, the projected content is designed in relation to the geometric structure of the object, in order to generate animations or images adapted to its surface characteristics. To ensure visual clarity in the final result, all source materials used during production must have a resolution corresponding to or higher than the output resolution of the projector. All images used in the project have been guaranteed with surplus quality. The point cloud derived images used to cover the entire model have a guaranteed resolution of 7108 × 10652 pixels, while the final video was exported in a vertical format at a resolution of 2160 × 3840 pixels, with an aspect ratio of 9:16.

2) Mapping Calibration

The purpose of this stage is to establish spatial correspondence between the digital imagery and the projection object (physical model of Old Nisa). The core issue in mapping calibration is addressing the structural differences between 2D media and 3D surfaces. Therefore, it is necessary to reconstruct the planar coordinates of the digital image into spatial coordinates corresponding to the projector's viewpoint through pre-simulation.

The placement of the projector plays a crucial role in the calibration process. Considering the scale and form of the Old Nisa model, the primary viewing direction was defined as a vertical top view, thus a single projector was sufficient to meet the requirements. The calibration process was performed in the 3D animation software Blender, simulating the projector's position from the top. A non-perspective orthographic camera was preset to generate the adjusted final projection video. The calibrated content was then exported directly to the projection device, thereby reducing on site adjustment time.

One issue identified during testing was that slight shadowing could occur in some densely built areas because of marginal decline at the edges of the projection beam. However, in actual situation, the projector is placed at a sufficient distance to ensure the beam was effectively perpendicular, thus guaranteeing overall projection quality (Fig. 84).

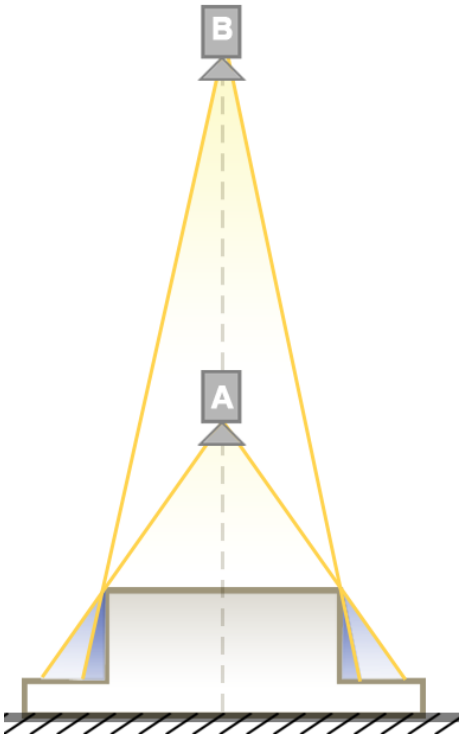

Fig. 84 Reduction of blind spots due to changes in projector position

In more complex configurations, multiple projectors could be required to form a coverage network in order to avoid occlusion and insufficient brightness. In addition to exporting pre simulated projection content, it is also possible to use live projection software such as MadMapper and HeavyM to adjust image displacement in real time through control grids.

3) Testing in the Physical Environment

The main purpose of this stage is to verify performance in real world environment. Based on the effect of the projection in the actual environment, parameters such as brightness and texture contrast are adjusted in an integrated manner to achieve the optimal final result (Fig. 85).

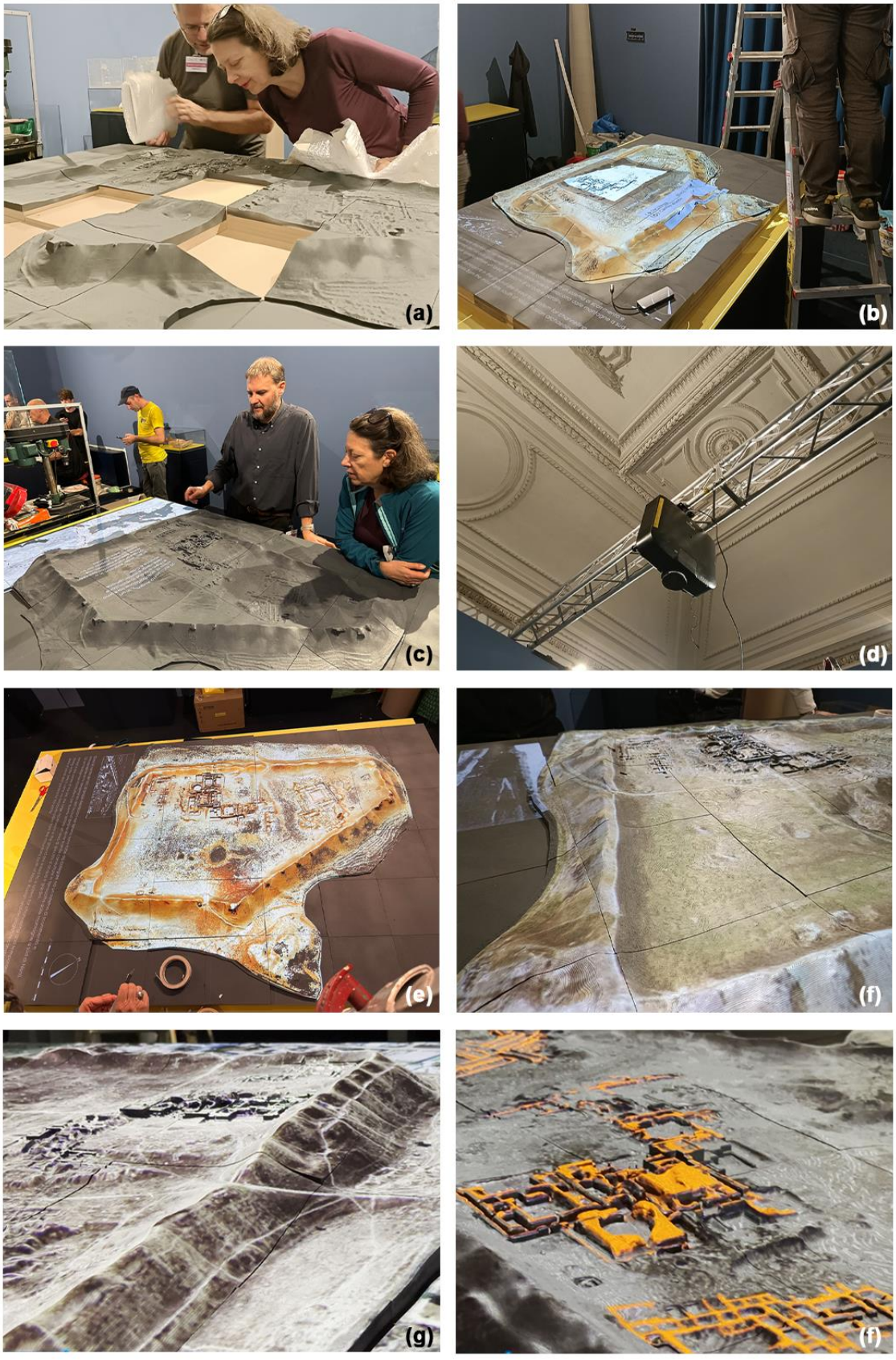

Fig. 85 On-site model assembly, projection debugging and testing

6.4 Final Projection Mapping Outcomes

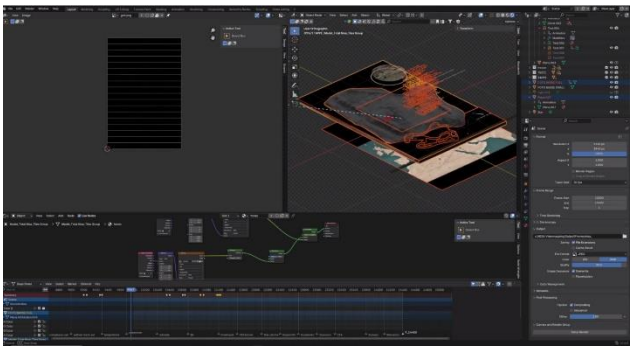

Fig. 86 Video planning in Blender

The projection was implemented with projector Epson EB PU1006. According to feedback from the production team, the main technical challenges during the process were from the diversity of intended visual effects and the tight coupling between the source materials and the production workflow. To ensure that all content could be managed uniformly within a single scene, the team chose to complete all compositing and animation work in Blender.

However, since the narrative structure required the simultaneous integration of 2D information (e.g. text, photographs, and explanatory graphics) together with 3D visualizations (e.g. solar path animations and simulated model shadows), also because these layers were linked through both timeline and spatial effects, these materials finally accumulated into complex layered compositions. This made it difficult to select, edit, or adjusting the timeline (Fig. 86).

Instead, it is possible to produce visual effects animation and projection simulation separately, and to use video editing software such as Premiere or Resolve as auxiliary tools. Nevertheless, certain processes still inevitably need to be completed within Blender. In addition, due to adjustments in the post production script, several originally planned features with higher technical complexity were replaced with simpler simulated animations based on point cloud derived images. This change did not affect the effectiveness of information delivery, and the final demonstration was still able to convey the core content clearly.

In the final on site test, slight texture seams are visible in the actual projection, however the overall result is satisfying. The projection is in high quality and blended naturally with the surface of the model (Fig. 87).

Fig. 87 Final projection effect

Conclusion

This thesis explores how the geomatic tools are involved in the digital documentation of archaeological site of Old Nisa, with the integration of terrestrial laser scanning (TLS), SLAM based mobile mapping, 3D printing method, and video mapping-based multimedia technologies. Through reviewing the technical workflow, this study demonstrated the advantages of multi-source survey data fusion, and proved its application value in the fields of heritage conservation and dissemination.

From a geomatics perspective, the combined use of TLS and SLAM LiDAR provides a reliable foundation for the digital documentation of large-scale sites in complex environments. The involvement of TLS ensures millimeter level accuracy in high detailed areas and reliability of the reference system, while SLAM compensates for data gaps in occluded zones. Through a series of denoising, calibration and registration procedures, high quality point clouds can be produced. Mesh reconstruction and tests under different levels of detail further reveal how reconstruction parameters and point cloud density influence the detail of digital model, providing a reference for future model generation at different scales. The transformation from digital to physical models shows the potential of 3D printing technology in the visualization of archaeological sites, while the difficulties encountered in actual production also indicate directions for future improvement. The introduction of video mapping ultimately transforms the physical model into a visual language. By integrating historical narratives with spatial information, it demonstrates the ability of multimedia technologies to enhance immersion and dissemination efficiency in cultural heritage presentation.

Overall, this research highlights the importance of interdisciplinary cooperation among archaeology, geomatics, 3D manufacturing and digital technologies. The workflow of archaeological survey - site digitization - derived product production implemented at heritage site the Old Nisa provides a reference for the digital documentation of heritage sites with large scale in the future. In addition, the role

of digital technologies in heritage conservation extends far beyond documentation. They are also able to support research analysis, assist conservation planning, and engage the public through different media. Although challenges remain in data integration and derivative product creation, the results of this research clearly reveal that interdisciplinary approaches can enhance the vitality of cultural heritage. Future work could focus on further exploration of point cloud optimization (e.g. using alternative tools or testing automated filtering), more efficient physical production methods, and the development of interactive projection systems in order to strengthen the links between geomatics, digital-related manufacturing, and multimedia narratives.

Reference

Bibliography and Websites

A

- Al Rashid, A., Ahmed, W., Khalid, M. Y., & Koc, M. (2021). Vat photopolymerization of polymers and polymer composites: Processes and applications. *Additive Manufacturing*, *47*, 102279.
- Anadolu Agency. (2021, August 5). Schliemann's destruction in Turkey's Troy repaired after 150 years. Daily Sabah. Retrieved from https://www.dailysabah.com/world/mid-east/us-designates-saudi-major-non-nato-ally-as-mbs-visits-washington
- Autodesk. (n.d.). *Point clouds.* Retrieved from https://www.autodesk.com/solutions/point-clouds
- Avena, M., Patrucco, G., Remondino, F., & Spanò, A. (2024). A scalable approach for automating Scan-to-BIM processes in the heritage field. *The International Archives of the Photogrammetry, Remote Sensing and Spatial Information Sciences*, *48*, 25-31.

B

- Bosse, M., & Zlot, R. (2009, May). Continuous 3D scan-matching with a spinning 2D laser. In *2009 IEEE International Conference on Robotics and Automation* (pp. 4312-4319). IEEE.
- Bosse, M., Zlot, R., & Flick, P. (2012). Zebedee: Design of a spring-mounted 3-D range sensor with application to mobile mapping. *IEEE Transactions on Robotics, 28*(5), 1104-1119.
- Britannica Editors. (2025). Parthia. Retrieved from https://www.britannica.com/place/Parthia
- Bruno, J. (2019). Old Nisa - Mithradatkert. In Re-Search. Archaeology in Central Asia and the South Caucasus, June 4-5, 2019. Staatliche Museen zu Berlin.

C

- Capra, A., Bertacchini, E., Castagnetti, C., Rivola, R., & Dubbini, M. (2015). Recent approaches in geodesy and geomatics for structures monitoring. *Rendiconti Lincei, 26*(Suppl 1), 53-61.
- Carvalho, A., & Matos, A. (2018). Museum professionals in a digital world: insights from a case study in Portugal. *Museum International*, *70*(1-2), 34-47.
- Chaiyatham, P. (2022). And There Was Light: The Use of Projection Mapping for Historic Preservation (Doctoral dissertation, Columbia University).
- CloudCompare Wiki. (2015, August 16). *Noise filter* [Web page]. Retrieved from https://www.cloudcompare.org/doc/wiki/index.php/Noise_filter

- CloudCompare Wiki. (2015, October 6). *SOR filter* [Web page]. Retrieved from https://www.cloudcompare.org/doc/wiki/index.php/SOR_filter
- CloudCompare. (n.d.). *CloudCompare user manual (Version 2.6.1)* [Software documentation]. Retrieved from https://www.cloudcompare.org/doc/qCC/CloudCompare%20v2.6.1%20-%20User%20manual.pdf

E

- Elhashash, M., Albanwan, H., & Qin, R. (2022). A review of mobile mapping systems: From sensors to applications. *Sensors, 22*(11), 4262.
- Elseberg, J., Borrmann, D., & Nüchter, A. (2013). One billion points in the cloud An octree for efficient processing of 3D laser scans. *ISPRS Journal of Photogrammetry and Remote Sensing, 76,* 76-88.

F

- FARO Technologies. (n.d.). Reference target placement for automatically registering scans in SCENE. Retrieved from https://knowledge.faro.com/Hardware/Focus/Focus/Reference_Target_Placement_for_Automatically_Registering_Scans_in_SCENE
- FARO Technologies. (n.d.). *Point clouds for beginners.* Retrieved from https://www.faro.com/en/Resource-Library/Article/Point-Clouds-for-Beginners

G

- Garagnani, S., Gaucci, A., & Gruska, B. (2016). From the archaeological record to ArchaeoBIM: the case study of the Etruscan temple of Uni in Marzabotto. *Virtual Archaeology Review*, *7*(15), 77-86.
- Garrido-Carretero, M. S., Borque-Arancón, M. J., Ruiz-Armenteros, A. M., Moreno-Guerrero, R., & Gil-Cruz, A. J. (2019). Low-cost GNSS receiver in RTK positioning under the standard ISO-17123-8: A feasible option in geomatics. *Measurement, 137,* 168-178.
- Gebre-Egziabher, D., & Gleason, S. (2009). *GNSS applications and methods.* Artech House.
- Grussenmeyer, P., Landes, T., Voegtle, T., & Ringle, K. (2008). Comparison methods of terrestrial laser scanning, photogrammetry and tacheometry data for recording of cultural heritage buildings. *International Archives of Photogrammetry, Remote Sensing and Spatial Information Sciences, 37*(B5), 213-218.

H

- Hearn, M. F. (Ed.). (1990). The architectural theory of Viollet-le-Duc: Readings and commentary. MIT Press.

- Hirt, C. (2014). Digital terrain models. In *Encyclopedia of geodesy* (pp. 1-6). Springer.
- International Council of Museums. (1931). The Athens Charter for the Restoration of Historic Monuments: Adopted at the First International Congress of Architects and Technicians of Historic Monuments, Athens 1931.
- International Council on Monuments and Sites. (1964). International charter for the conservation and restoration of monuments and sites (The Venice Charter 1964). Paris: ICOMOS. Retrieved from https://www.icomos.org/the-history-of-icomos/
- International Council on Monuments and Sites. (1990). Charter for the protection and management of the archaeological heritage (The Lausanne Charter 1990). Paris: ICOMOS. Retrieved from https://www.icomos.org/charters-and-doctrinal-texts/
- ISO & ASTM International. (2021). ISO/ASTM 52900:2021 - Additive manufacturing: General principles, fundamentals and vocabulary. Geneva, Switzerland: ISO.

J

- Jackson, M. L. (2006). The principles of preservation: The influences of Viollet, Ruskin and Morris on historic preservation. Oklahoma State University.
- Jia, X. (2025, July 3). Wengu: From the excavation of Dingling to successful World Heritage inscription, the historical appearance of the Ming Tombs is gradually restored. Beijing Daily. Retrieved from https://xinwen.bjd.com.cn/content/s6865c7a8e4b0bd64e2e06a4e.html

K

- Karsznia, K., Osada, E., & Muszyński, Z. (2023). Real-time adjustment and spatial data integration algorithms combining total station and GNSS surveys with an earth gravity model. *Applied Sciences, 13*(16), 9380.
- Katsianis, M., Tsipidis, S., Kotsakis, K., & Kousoulakou, A. (2008). A 3D digital workflow for archaeological intra-site research using GIS. *Journal of Archaeological Science*, *35*(3), 655-667.
- Kazhdan, M., Bolitho, M., & Hoppe, H. (2006, June). Poisson surface reconstruction. In *Proceedings of the Fourth Eurographics Symposium on Geometry Processing* (Vol. 7, No. 4).
- Keshavarz Rahbar, G. (2024). Urban Development and Architectural Manifestations of the Parthian Period of Iran (III BC-III AD centuries). *European Online Journal of Natural and Social Sciences*, *13*(3), pp-213.
- Kong, B. (2025). Applications of projection mapping on models: Art of space and light

(Research essay, Politecnico di Torino)

- Kristiawan, R. B., Imaduddin, F., Ariawan, D., Ubaidillah, & Arifin, Z. (2021). A review on the fused deposition modeling (FDM) 3D printing: Filament processing, materials, and printing parameters. *Open Engineering, 11*(1), 639-649.

L

- Labbé, M., & Michaud, F. (2014, September). Online global loop closure detection for large-scale multi-session graph-based SLAM. In *2014 IEEE/RSJ International Conference on Intelligent Robots and Systems* (pp. 2661-2666). IEEE.
- Langley, R. B., Teunissen, P. J., & Montenbruck, O. (2017). Introduction to GNSS. In *Springer handbook of global navigation satellite systems* (pp. 3-23). Springer International Publishing.
- Lemmens, M. (2011). Terrestrial laser scanning. In *Geo-information: Technologies, applications and the environment* (pp. 101-121). Springer Netherlands.
- Leica Geosystems. (n.d.). *Mobile mapping systems.* Retrieved from https://leica-geosystems.com/products/mobile-mapping-systems
- Lenti, R. (2025). *REPORT-Nisa SLAM point cloud denoising* [Technical report]. Geomatics Lab G4CH.
- Lippolis, C., Manassero, N., Invernizzi, A., Pappalardo, E., & Menegazzi, R. (2011). *Gli splendori di Nisa Partica - Scavi italiani in Turkmenistan*. Torino: Istituto San Giuseppe. Retrieved from https://www.collegiosangiuseppe.it/Resource/CatalogoNisaPartica.pdf
- Lippolis, C., Spanò, A., Patrucco, G., & Messina, V. (2024). Rapid digital documentation of endangered archaeological contexts: a case-study from Seleucia on the Tigris (central Iraq). *Parthica: incontri di culture nel mondo antico: 26, 2024*, 29-39.
- Lippolis, C. (2025). Nisa vecchia - Mithradatkert, il memoriale degli Arsacidi [Unpublished manuscript].
- Li, Z., Rathore, A. S., Song, C., Wei, S., Wang, Y., & Xu, W. (2018, October). PrinTracker: Fingerprinting 3D printers using commodity scanners. In *Proceedings of the 2018 ACM sigsac conference on computer and communications security* (pp. 1306-1323).

M

- Masson, M. E., & Pugačenkova, G. A. (1982). The Parthian rhytons of Nisa (Trad. di Parfjanskie ritony Nisy, 1959). Monografie di Mesopotamia I. Firenze.
- Maniello, D. (2015). Augmented reality in public spaces. Basic techniques for video mapping, 1.
- Maniello, D. (2023). Augmented Heritage. Dall'oggetto esposto all'oggetto narrato. Le Penseur.

- McClements, D. (2022, July 15). *How to compare SLA and DLP* [Article]. Xometry. Updated August 27, 2024, by M. Conniff. Retrieved from https://www.xometry.com/resources/3d-printing/sla-vs-dlp-3d-printing/
- Mill, T., Alt, A., & Liias, R. (2013). Combined 3D building surveying techniques-Terrestrial laser scanning (TLS) and total station surveying for BIM data management purposes. *Journal of Civil Engineering and Management, 19*(sup1), S23-S32.
- Mohammed, S. I. (2021, May). Important methods measurements to exam the accuracy and reliability of reflector-less total station measurements. In *Journal of Physics: Conference Series* (Vol. 1895, No. 1, p. 012007). IOP Publishing.
- Mukupa, W., Roberts, G. W., Hancock, C. M., & Al-Manasir, K. (2017). A review of the use of terrestrial laser scanning application for change detection and deformation monitoring of structures. *Survey Review, 49*(353), 99-116.
- Musei Capitolini. (2025). *Antiche civiltà del Turkmenistan*. Retrieved from https://www.museicapitolini.org/it/mostra-evento/antiche-civilt-del-turkmenistan

N

- NASA. (n.d.). *Digital elevation and terrain models (DEM)*. NASA Earthdata. Retrieved from https://www.earthdata.nasa.gov/topics/land-surface/digital-elevation-terrain-model-dem
- Nex, F., & Remondino, F. (2014). UAV for 3D mapping applications: A review. *Applied Geomatics, 6*(1), 1-15.

O

- Ogundare, J. O. (2015). Precision surveying: The principles and geomatics practice. John Wiley & Sons.

P

- Patrucco, G., Bambridge, P., Giulio Tonolo, F., Markey, J., & Spanò, A. (2023). Digital replicas of British museum artefacts. The International Archives of the Photogrammetry, Remote Sensing and Spatial Information Sciences, 48, 1173-1180.
- Patrucco, G., Setragno, F., & Spanò, A. (2025). Synthetic Training Datasets for Architectural Conservation: A Deep Learning Approach for Decay Detection. *Remote Sensing*, *17*(10), 1714.
- Pilipko, V. N. (2015). Stanovlenie i razvitie parfjanskoj kul'tury na territorii južnogo Turkmenistana. AIK.
- Pogumax. (2024). Everything about Projection Mapping (Video Mapping): How Businesses Can Increase Profits with Projection Technologies. Pogumax. Retrieved from https://pogumax.com/blog/everything-about-projection-mapping

Q

- QGIS Association. (2025). *QGIS Geographic Information System* (Version x.x) [Software]. QGIS Association. Retrieved from https://qgis.org
- Qi, H., & Moore, J. B. (2002). Direct Kalman filtering approach for GPS/INS integration. *IEEE Transactions on Aerospace and Electronic Systems, 38*(2), 687-693.
- Quan, H., Zhang, T., Xu, H., Luo, S., Nie, J., & Zhu, X. (2020). Photo-curing 3D printing technique and its challenges. *Bioactive Materials, 5*(1), 110-115.

R

- Raise3D. (2024). *3D printing applications*. Retrieved from https://www.raise3d.com/blog/3d-printing-applications/
- Rajan, K., Samykano, M., Kadirgama, K., Harun, W. S. W., & Rahman, M. M. (2022). Fused deposition modeling: Process, materials, parameters, properties, and applications. *The International Journal of Advanced Manufacturing Technology, 120*(3), 1531-1570.
- Remondino F, Stylianidis E. 3D recording, documentation and management of cultural heritage[M]. Dunbeath, UK: Whittles Publishing, 2016.
- Roussel, R., & De Luca, L. (2023). An approach to build a complete digital report of the notre dame cathedral after the fire, using the aioli platform. *The International Archives of the Photogrammetry, Remote Sensing and Spatial Information Sciences*, *48*, 1359-1365
- Rusinkiewicz, S., & Levoy, M. (2001, May). Efficient variants of the ICP algorithm. In *Proceedings of the Third International Conference on 3-D Digital Imaging and Modeling* (pp. 145-152). IEEE.
- Rusu, R. B., Blodow, N., & Beetz, M. (2009, May). Fast point feature histograms (FPFH) for 3D registration. In *2009 IEEE International Conference on Robotics and Automation* (pp. 3212-3217). IEEE.

S

- Sammartano, G., & Spanò, A. (2018). Point clouds by SLAM-based mobile mapping systems: Accuracy and geometric content validation in multisensor survey and stand-alone acquisition. *Applied Geomatics, 10*(4), 317-339.
- Santoro, V., Patrucco, G., Lingua, A., & Spanò, A. (2023). Multispectral UAV data enhancing the knowledge of landscape heritage. *The International Archives of the Photogrammetry, Remote Sensing and Spatial Information Sciences*, *48*, 1419-1426.
- Santoro, V., Wu, Z., Patrucco, G., & Spanò, A. (2024). Investigations of non-visible features in archaeological sites: testing aerial remote sensing with UAV in Pompeii. *Virtual Archaeology Review*.
- Scherer, M., & Lerma, J. L. (2009). From the conventional total station to the prospective

image assisted photogrammetric scanning total station: Comprehensive review. *Journal of Surveying Engineering, 135*(4), 173-178.

- Sharer, R. J., & Ashmore, W. (1988). *Archaeology: Discovering our past*. Mayfield Publishing Company.
- Shahrubudin, N., Lee, T. C., & Ramlan, R. J. (2019). An overview on 3D printing technology: Technological, materials, and applications. *Procedia Manufacturing, 35*, 1286-1296.
- Sheng, B., Zhao, F., Yin, X., Zhang, C., Wang, H., & Huang, P. (2018). A lightweight surface reconstruction method for online 3D scanning point cloud data oriented toward 3D printing. *Mathematical Problems in Engineering*, *2018*(1), 4673849.
- Spanò, A. (2024). *Report Nisa_dati pesi* [Unpublished report]. Geomatics Lab G4CH.
- Spanò, N., Patrucco, G., & Bonfanti, C. (2024). Integrated 3D survey activities in the Old Nisa site: Terrestrial (TLS) and mobile laser scanning integrated methods [Technical report]. Geomatics Lab G4CH & CRAST.
- Spanò, A. (2025). *Rilievo d'emergenza_spanò* [Unpublished report].
- Stanco, F., Battiato, S., & Gallo, G. (2011). *Digital imaging for cultural heritage preservation*. Boca Raton, FL, USA: CRC press.
- Staraja Nisa. Sdanie c kvadratnym zalóm. (1996). Moskva.
- Staraja Nisa. Osnovnye itogi arheologičeskogo izučenija v sovetskij period. (2001). Moskva.
- Subedi, S., Liu, S., Wang, W., Naser Shovon, S. A., Chen, X., & Ware, H. O. T. (2024). Multi-material vat photopolymerization 3D printing: A review of mechanisms and applications. *npj Advanced Manufacturing, 1*(1), 9.
- Szrek, A., Romańczukiewicz, K., Kujawa, P., & Trybała, P. (2024). Comparison of TLS and SLAM technologies for 3D reconstruction of objects with different geometries. In *IOP Conference Series: Earth and Environmental Science* (Vol. 1295, No. 1, p. 012012). IOP Publishing.

T

- The Editors of Encyclopaedia Britannica. (n.d.). Arsacid dynasty summary. In Encyclopaedia Britannica. Retrieved from https://www.britannica.com/summary/Arsacid-dynasty
- The Editors of Encyclopaedia Britannica. (n.d.). Battle of Carrhae summary. In Encyclopaedia Britannica. Retrieved from https://www.britannica.com/summary/Battle-of-Carrhae
- The Editors of Encyclopaedia Britannica. (n.d.). Ctesiphon. In Encyclopaedia Britannica. Retrieved from https://www.britannica.com/place/Ctesiphon-ancient-city-Iraq

U

- UNESCO. (1972). Convention concerning the protection of the world cultural and natural heritage. Paris: UNESCO.
- UNESCO. (2003). Convention for the safeguarding of the intangible cultural heritage. Paris: UNESCO.
- UNESCO World Heritage Centre. (2007). Parthian Fortresses of Nisa. UNESCO World Heritage List. Retrieved from https://whc.unesco.org/en/list/1242/
- UNESCO World Heritage Centre. (2007). Nomination file 1242: Parthian Fortresses of Nisa. Retrieved from https://whc.unesco.org/uploads/nominations/1242.pdf
- UNESCO. (2017). Operational guidelines for the implementation of the World Heritage Convention. Paris: UNESCO World Heritage Centre.
  Retrieved from https://whc.unesco.org/en/glossary/319

W

- Wang, F. F., & Du, J. (2021). Digital presentation and communication of cultural heritage in the post-pandemic era. *ISPRS Annals of the Photogrammetry, Remote Sensing and Spatial Information Sciences*, *8*, 187-192.
- Wang, Q., Tan, Y., & Mei, Z. (2020). Computational methods of acquisition and processing of 3D point cloud data for construction applications. *Archives of computational methods in engineering, 27*(2), 479-499.
- Wang, S. S. (2022). The Rise and Fall of the Arsacid (Parthian) Dynasty. The Commercial Press.
- Wang, X., Pan, H., Guo, K., Yang, X., & Luo, S. (2020, May). The evolution of LiDAR and its application in high precision measurement. In *IOP Conference Series: Earth and Environmental Science* (Vol. 502, No. 1, p. 012008). IOP Publishing.

Y

- Yiğit, A. Y., Hamal, S. N. G., Ulvi, A., & Yakar, M. (2024). Comparative analysis of mobile laser scanning and terrestrial laser scanning for indoor mapping. *Building Research & Information, 52*(4), 402-417.

Z

- Zhang, Q., Niu, X., & Shi, C. (2019). Assessment of the effect of GNSS sampling rate on GNSS/INS relative accuracy on different time scales for precision measurements. *Measurement, 145,* 583-593.
- Zhang, W., Qi, J., Wan, P., Wang, H., Xie, D., Wang, X., & Yan, G. (2016). An easy-to-use airborne LiDAR data filtering method based on cloth simulation. *Remote Sensing, 8*(6), 501.

- Zhao, S., Hou, M., Hu, Y., & Zhao, Q. (2018). Application of 3D model of cultural relics in virtual restoration. *The International Archives of the Photogrammetry, Remote Sensing and Spatial Information Sciences*, *42*, 2401-2405.

Appendix

Mean and Standard Deviation and Histogram Calculation

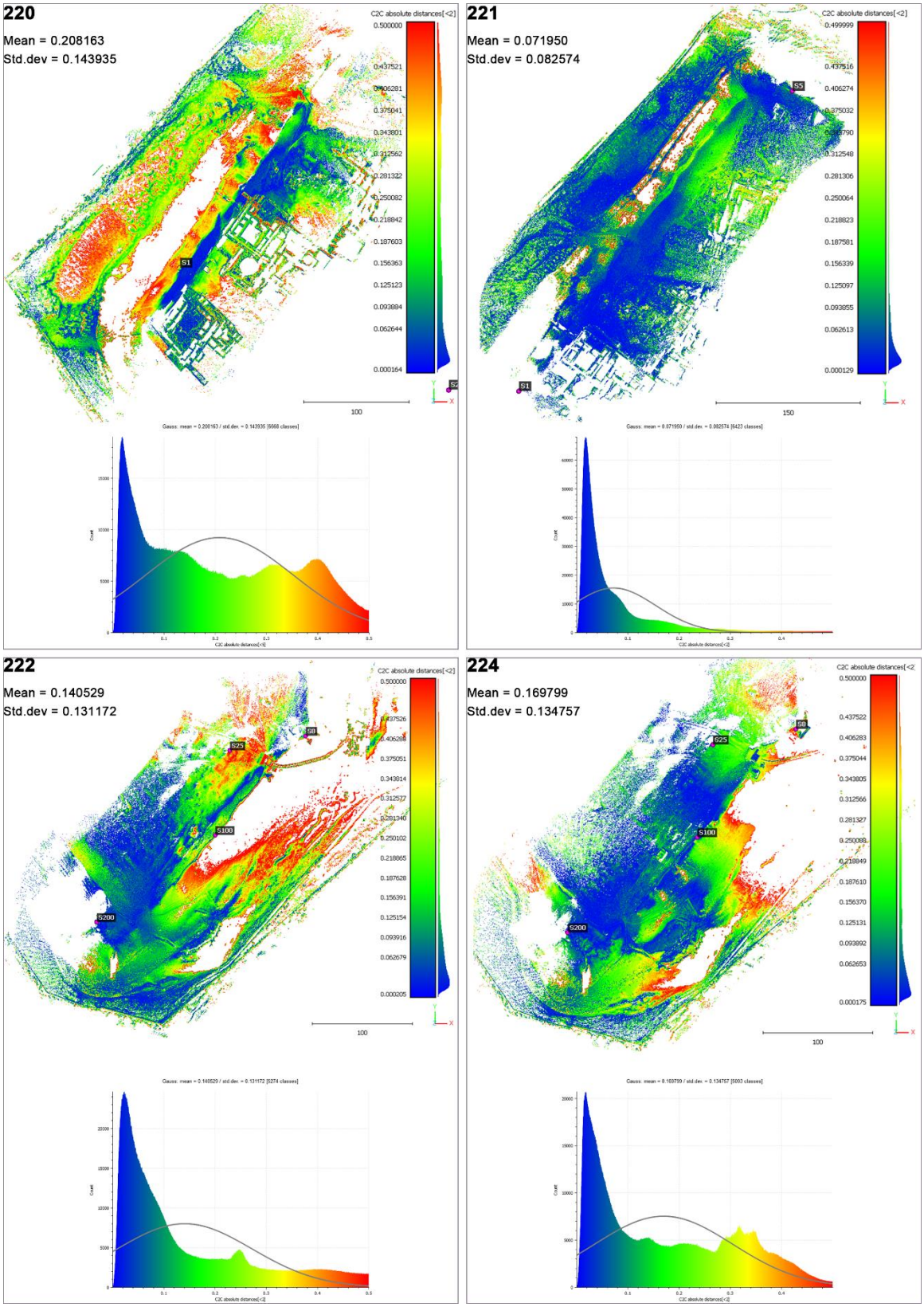

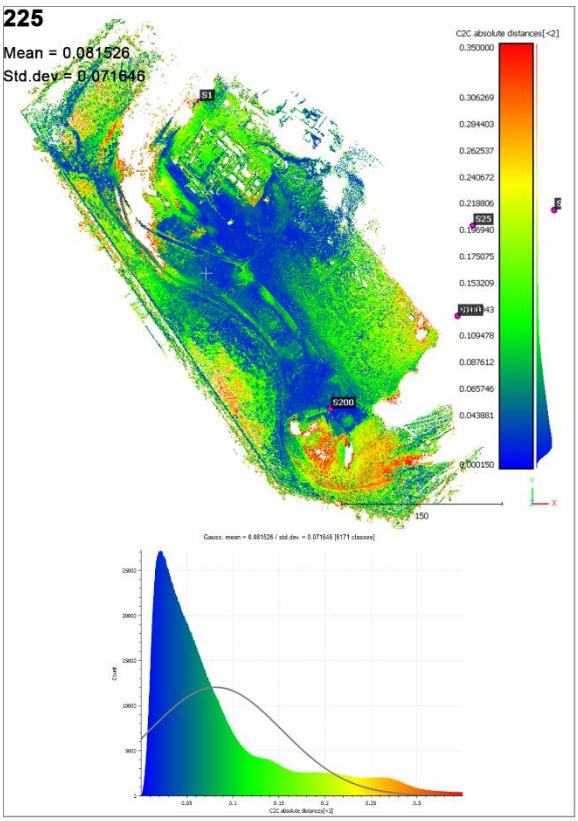
225
Mean = 0.081526
Std.dev = 0.071646
C2C absolute distances[<2]
0.350000
0.306269
0.284403
0.262537
0.240672
0.218806
0.196940
0.175075
0.153209
0.131343
0.109478
0.087612
0.065746
0.043881
0.022015
0.000150
S1
S25
S100
S200
150

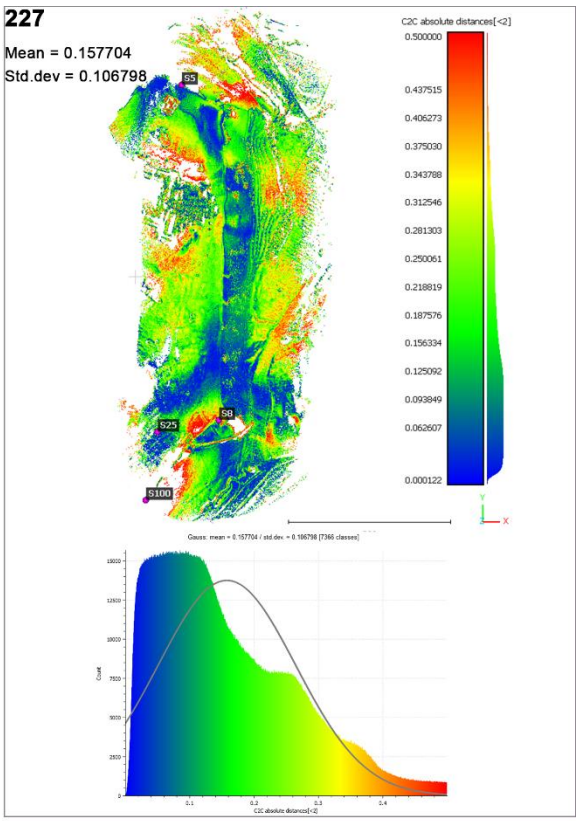
227
Mean = 0.157704
Std.dev = 0.106798
C2C absolute distances[<2]
0.500000
0.437515
0.406273
0.375030
0.343788
0.312546
0.281303
0.250061
0.218819
0.187576
0.156334
0.125092
0.093849
0.062607
0.000122
S5
S8
S25
S100

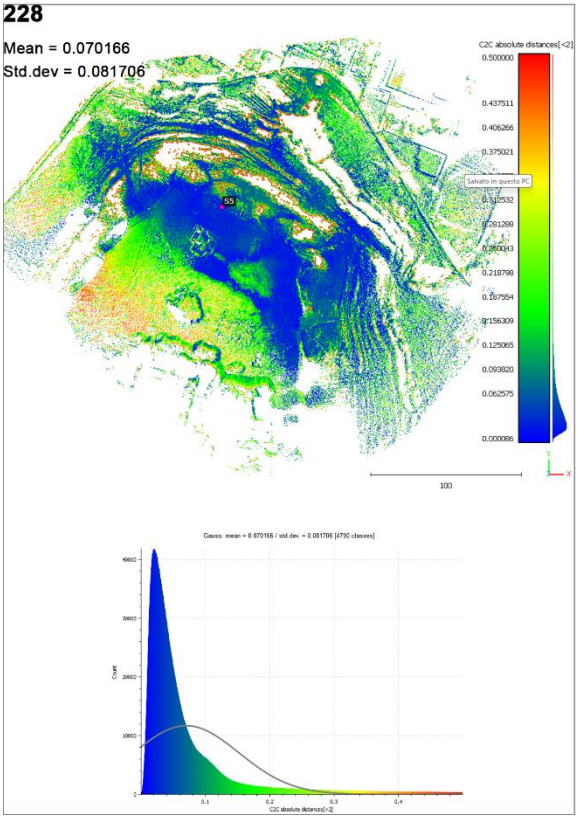
228
Mean = 0.070166
Std.dev = 0.081706
C2C absolute distances[<2]
0.500000
0.437511
0.406266
0.375021
0.343777
0.312532
0.281288
0.250043
0.218798
0.187554
0.156309
0.125065
0.093820
0.062575
0.000086
S5
100

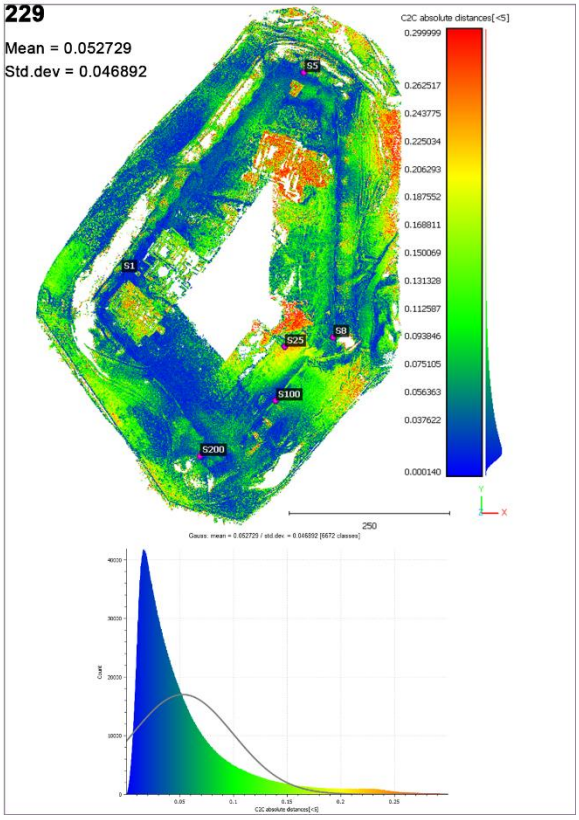
229
Mean = 0.052729
Std.dev = 0.046892
C2C absolute distances[<5]
0.299999
0.262517
0.243775
0.225034
0.206293
0.187552
0.168811
0.150069
0.131328
0.112587
0.093846
0.075105
0.056363
0.037622
0.000140
S1
S5
S8
S25
S100
S200
250

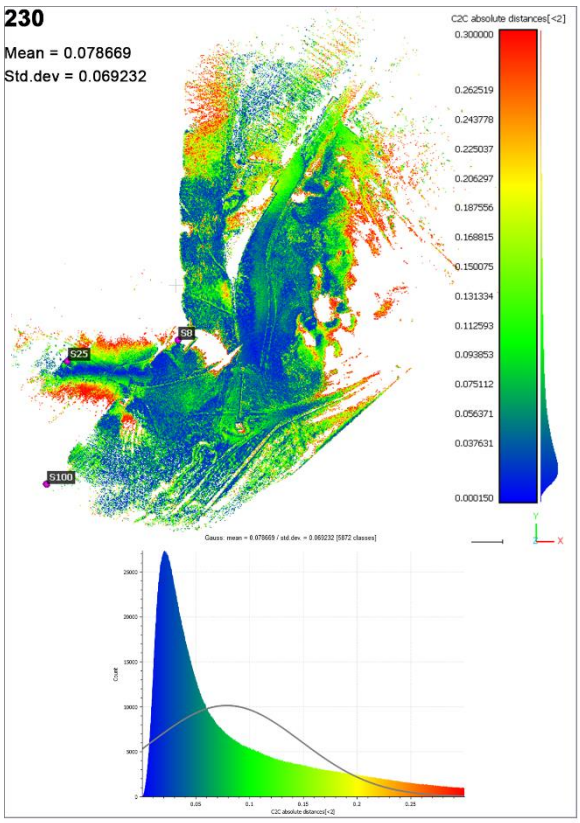
230
Mean = 0.078669
Std.dev = 0.069232
C2C absolute distances[<2]
0.300000
0.262519
0.243778
0.225037
0.206297
0.187556
0.168815
0.150075
0.131334
0.112593
0.093853
0.075112
0.056371
0.037631
0.000150
S8
S25
S100

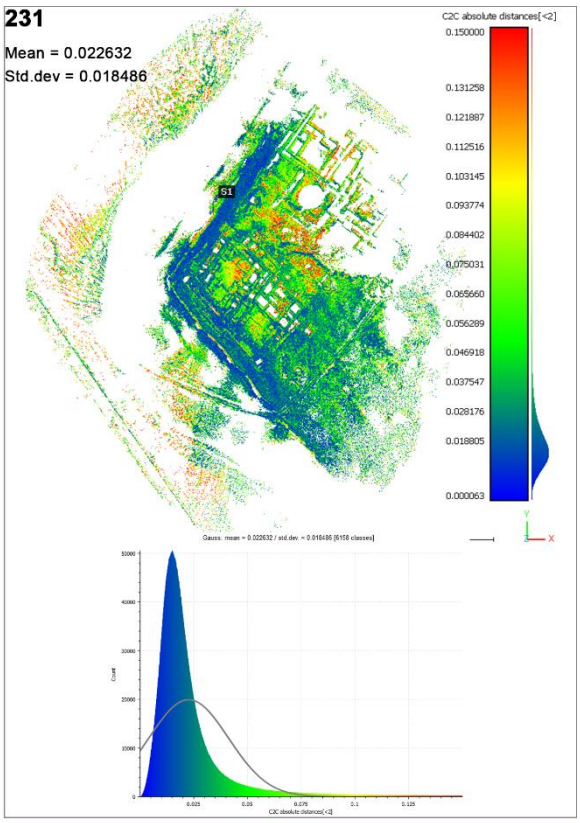
231
Mean = 0.022632
Std.dev = 0.018486
C2C absolute distances[<2]
0.150000
0.131258
0.121887
0.112516
0.103145
0.093774
0.084402
0.075031
0.065660
0.056289
0.046918
0.037547
0.028176
0.018805
0.000063
S1

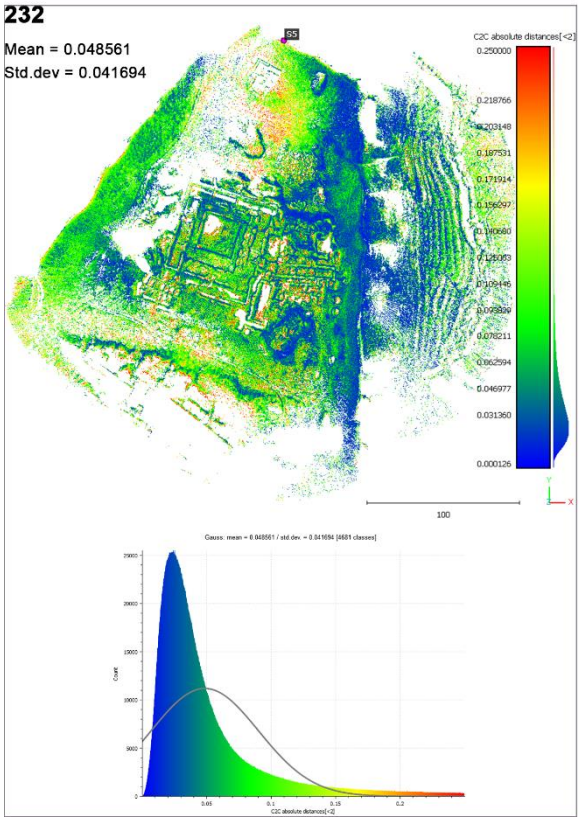
232
Mean = 0.048561
Std.dev = 0.041694
C2C absolute distances[<2]
0.250000
0.218766
0.203148
0.187531
0.171914
0.156297
0.140680
0.125063
0.109446
0.093829
0.078211
0.062594
0.046977
0.031360
0.000126
S5
100

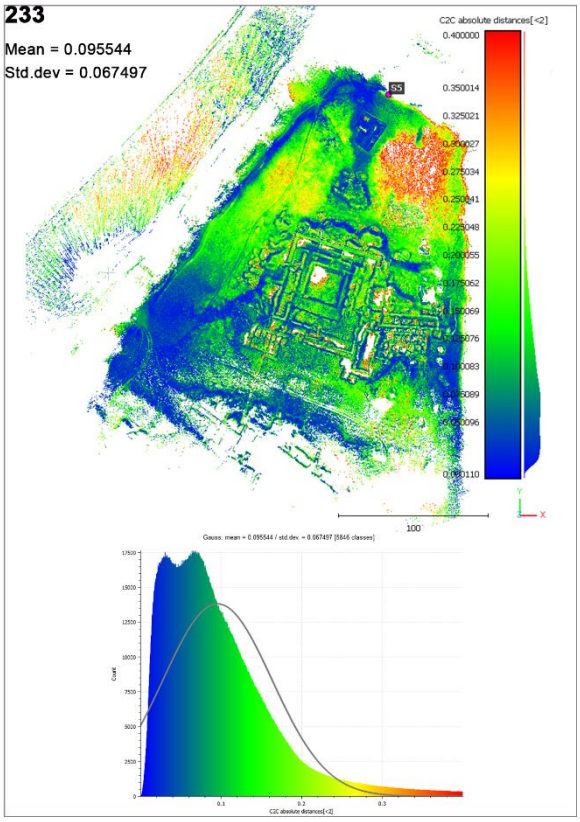
233
Mean = 0.095544
Std.dev = 0.067497
C2C absolute distances[<2]
0.400000
0.350014
0.325021
0.300027
0.275034
0.250041
0.225048
0.200055
0.175062
0.150069
0.125076
0.100083
0.075089
0.050096
0.000110
S5
100

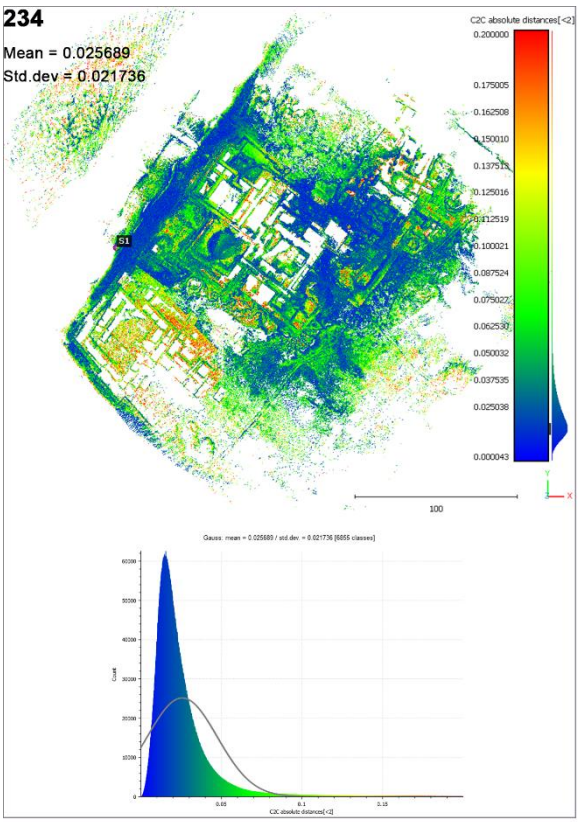
234
Mean = 0.025689
Std.dev = 0.021736
C2C absolute distances[<2]
0.200000
0.175005
0.162508
0.150010
0.137513
0.125016
0.112519
0.100021
0.087524
0.075027
0.062530
0.050032
0.037535
0.025038
0.000043
S1
100

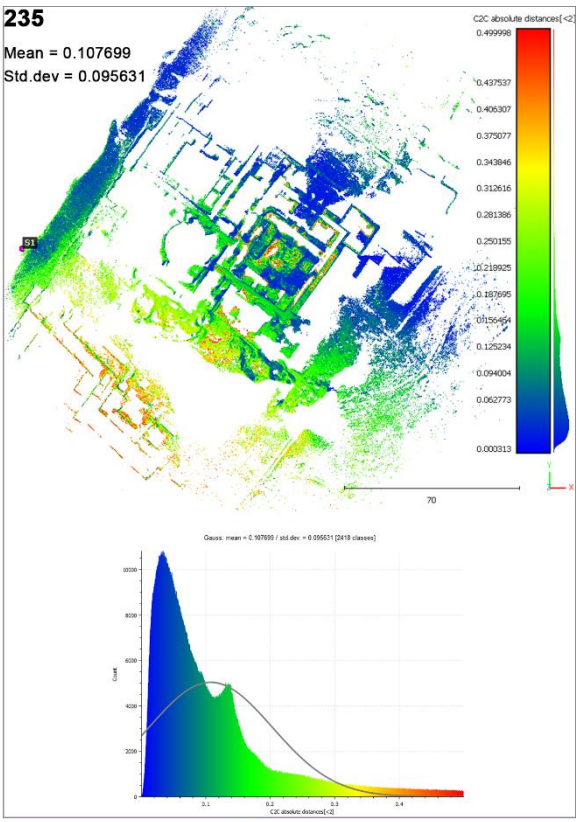
235
Mean = 0.107699
Std.dev = 0.095631
C2C absolute distances[<2]
0.499998
0.437537
0.406307
0.375077
0.343846
0.312616
0.281386
0.250155
0.218925
0.187695
0.156464
0.125234
0.094004
0.062773
0.000313
S1
70

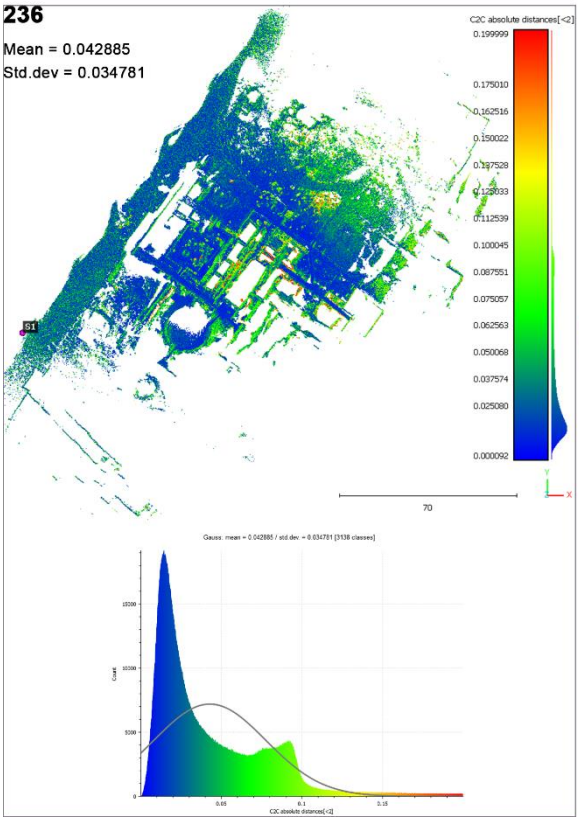
236
Mean = 0.042885
Std.dev = 0.034781
C2C absolute distances[<2]
0.199999
0.175010
0.162516
0.150022
0.137528
0.125033
0.112539
0.100045
0.087551
0.075057
0.062563
0.050068
0.037574
0.025080
0.000092
S1
70

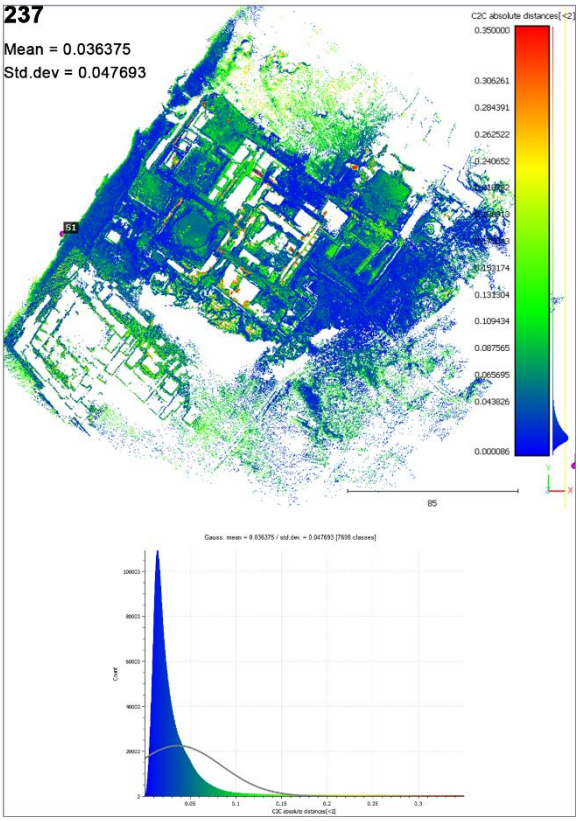
237
Mean = 0.036375
Std.dev = 0.047693
C2C absolute distances[<2]
0.350000
0.306261
0.284391
0.262522
0.240652
0.218783
0.196913
0.175043
0.153174
0.131304
0.109434
0.087565
0.065695
0.043826
0.000086
S1
85

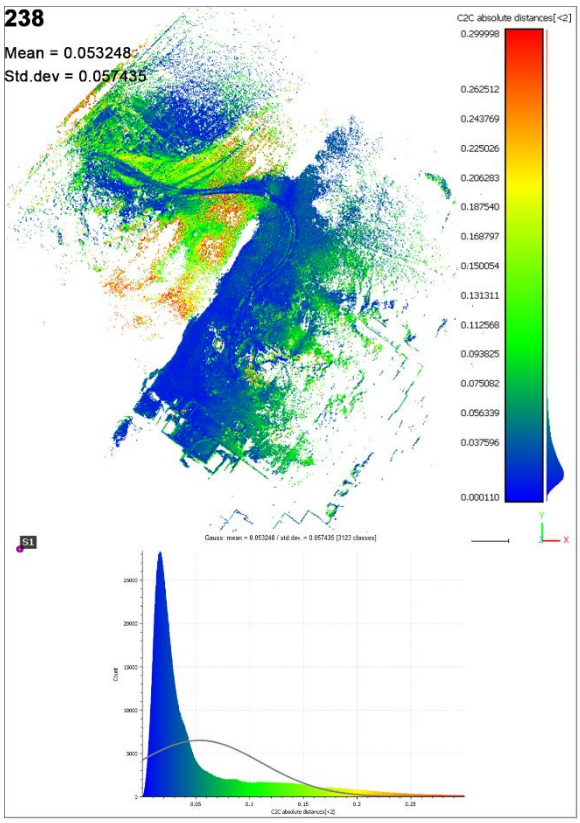
238
Mean = 0.053248
Std.dev = 0.057435
C2C absolute distances[<2]
0.299998
0.262512
0.243769
0.225026
0.206283
0.187540
0.168797
0.150054
0.131311
0.112568
0.093825
0.075082
0.056339
0.037596
0.000110
S1

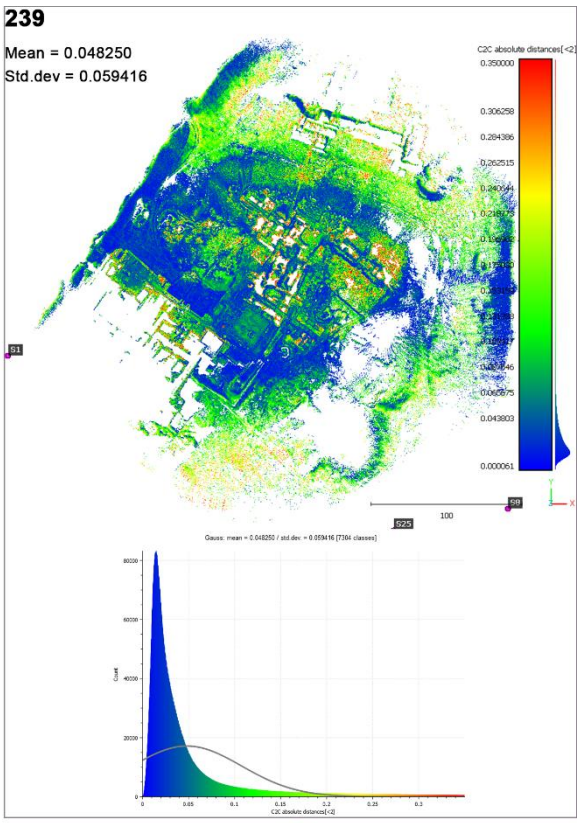
239
Mean = 0.048250
Std.dev = 0.059416
C2C absolute distances[<2]
0.350000
0.306258
0.284386
0.262515
0.240644
0.218773
0.196901
0.175030
0.153159
0.131288
0.109416
0.087545
0.065675
0.043803
0.000061
S1
S25
100

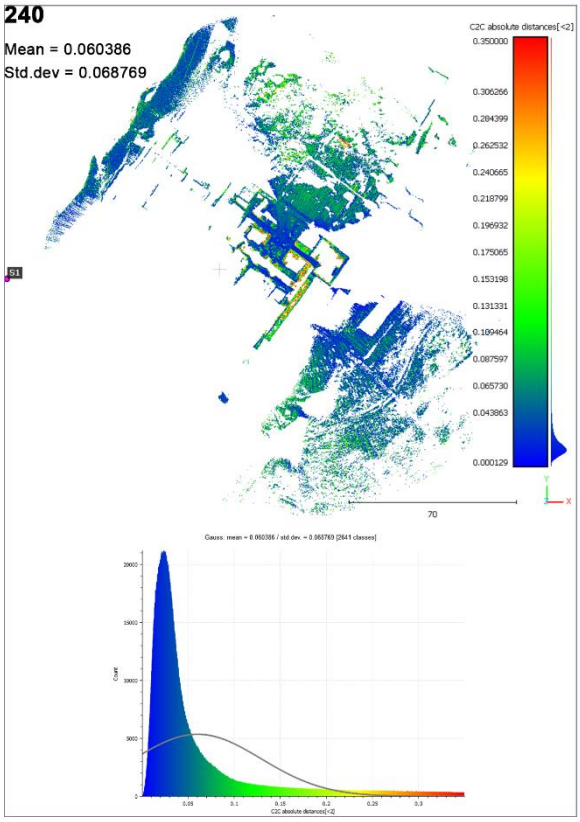
240
Mean = 0.060386
Std.dev = 0.068769
C2C absolute distances[<2]
0.350000
0.306266
0.284399
0.262532
0.240665
0.218799
0.196932
0.175065
0.153198
0.131331
0.109464
0.087597
0.065730
0.043863
0.000129
S1
70

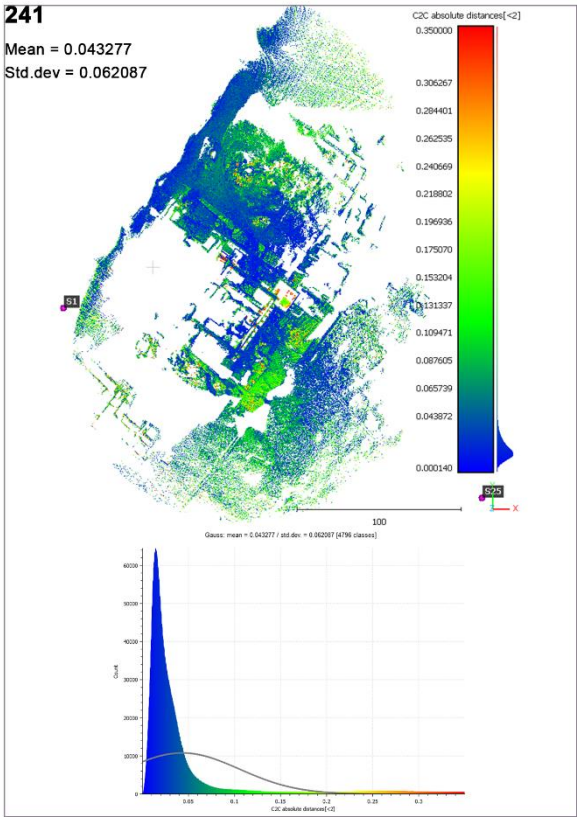
241
Mean = 0.043277
Std.dev = 0.062087
C2C absolute distances[<2]
0.350000
0.306267
0.284401
0.262535
0.240669
0.218802
0.196936
0.175070
0.153204
0.131337
0.109471
0.087605
0.065739
0.043872
0.000140
S1
S25
100